Freie Universität Berlin

A blended semi-implicit numerical model for weakly compressible atmospheric dynamics

Dissertation zur Erlangung des Grades
eines Doktors der Naturwissenschaften (Dr. rer. nat.)
am Fachbereich Mathematik und Informatik
der Freien Universität Berlin

vorgelegt von

Tommaso Benacchio

Berlin, 2014

A blended semi-implicit numerical model for weakly compressible atmospheric dynamics

Dissertation zur Erlangung des Grades
eines Doktors der Naturwissenschaften (Dr. rer. nat.)
am Fachbereich Mathematik und Informatik
der Freien Universität Berlin

vorgelegt von

Tommaso Benacchio

1. Gutachter und Betreuer:

Prof. Dr. Rupert Klein, Institut für Mathematik,
Freie Universität Berlin

2. Gutachter:

Prof. Dale Durran, Department of Atmospheric Sciences,
University of Washington

3. Gutachter:

Dr. Luca Bonaventura, MOX - Dipartimento di Matematica,
Politecnico di Milano

Datum der mündlichen Prüfung:

26. Juni 2014

Berlin, 2014

... ma qualche cosa imparo. Imparo a capir meglio la mia parte negativa, sopratutto, la mia debolezza, il mio amorproprismo, la mia ignoranza. Questo con calma, senza il gusto di cenere-in-bocca del disinganno. Bisogna viaggiare per conoscerci. Bisogna allontanarsi dallo specchio indulgente degli amici che ti amano e credono in te, — e trovarsi fra gente *ignota.*

Scipio Slataper

A Mario, Nini, Wassily e Marisa

Abstract. Physical processes in the atmosphere develop on a wide range of spatial and temporal scales. Meteorologically relevant phenomena move at speeds much lower than that of sound waves. The latter, despite their unimportance in weather and climate studies, enforce the use of very small time steps in explicit discretizations of the fully compressible equations.

Traditionally, the problem has been analytically tackled using reduced formulations – anelastic and pseudo-incompressible models on the small scales, hydrostatic models on large scales – that lack the terms that generate acoustics. Alternatively, fully compressible equations have been solved with split-explicit or semi-implicit numerical methods free of acoustic-dependent stability constraints. However, most existing approaches in this context resort to various forms of numerical filtering to achieve stability at the expense of accuracy.

The present study discusses a semi-implicit fully compressible numerical model for the simulation of low-speed flows in the atmosphere. The second-order accurate finite volume scheme extends a projection method for the pseudo-incompressible model and agrees with it by construction in the small-scale limit. Unlike most numerical approaches in meteorology, equations are solved in non-perturbational form and in terms of the thermodynamic pressure variable. Quantities are advanced in time in an explicit advection step limited by a stability threshold independent of sound speed. Compressibility is handled implicitly in a correction step that solves two elliptic problems for the pressure increments. Well-balancing techniques are used to discretize buoyancy without reference to a hydrostatically balanced background state.

Convergence properties are evaluated on the advection of a smooth vortex and compressibility effects are assessed on the case of a simple acoustic wave. Then, we test the ability of the scheme to accurately simulate gravity-driven flows with large time steps on thermal benchmarks in neutrally and stably stratified atmospheres. Obtained numerical solutions are found to be in line with published work.

Equations are then cast in a blended soundproof-compressible multimodel formulation allowing for controlled introduction of compressibility in the scheme. In a unified and uniformly accurate numerical framework, the blending feature is employed to filter acoustic perturbations in the initial stages of thermal simulations. The technique can find application in a data assimilation context, enabling on-the-fly incorporation of unbalanced data in the numerical model. The proposed extension to an implicit treatment of buoyancy envisages the use of the scheme as a flexible tool for the simulation of multiscale atmospheric flows.

Zusammenfassung. Atmosphärische Strömungen entfalten sich über ein breites Spektrum von Zeit- und Raumskalen. Prozesse von meteorologischer Bedeutung haben geringe Geschwindigkeiten im Vergleich zu Schallwellen, welche trotz ihres in Wetter- und Klimastudien unerheblichen Beitrags die Effizienz expliziter vollkompressibler Modelle auf sehr kleine Zeitschritte beschränken.

Im Allgemeinen wird das Problem durch approximierte Formulierungen wie anelastische und pseudo-inkompressible Modelle auf kleinen Skalen und hydrostatische Modelle auf großen Skalen analytisch angegangen, wobei die für die akustischen Störungen verantwortlichen Terme fehlen. Ansonsten können numerische split-explizite oder semi-implizite Verfahren auf die vollkompressiblen Gleichungen angewandt werden, um die Schallgeschwindigkeitsbedingte Stabilitätseinschränkung zu umgehen. Dennoch greifen in diesem Kontext etablierte Ansätze auf verschiedene Arten von numerischer Dämpfung zurück, welche sich zwangsläufig auf die Genauigkeit auswirken.

Diese Studie betrachtet ein semi-implizites vollkompressibles numerisches Verfahren zweiter Genauigkeitsordnung für die Simulation atmosphärischer Strömungen mit geringer Geschwindigkeit. Die Diskretisierung erweitert ein Projektionsverfahren für das pseudo-inkompressible Modell, mit dem sie im kleinskaligen Limes übereinstimmt. Im Gegensatz zu den meisten existierenden Formulierungen wird das Gleichungssystem mithilfe des thermodynamischen Drucks formuliert und wird nicht in Störungsform verfasst. Ein expliziter Schritt mit schallgeschwindigkeitsunabhängiger Stabilitätsbedingung bringt die Variablen über einen Zeitschritt voran, woraufhin zwei elliptische Probleme für die Druckinkremente in einem impliziten Schritt gelöst werden. Der Auftriebsterm wird mit well-balancing Methoden ohne Bezug auf ein hydrostatisches Profil behandelt.

Die Konvergenzeigenschaften werden an der Advektion eines glatten Wirbels geprüft und Kompressibilitätseffekte anhand einer akustischen Welle bewertet. Die Leistung des Verfahrens wird im Bereich von Simulationen schwerkraftgetriebener thermischer Luftblasen mit langen Zeitschritten in neutral- und stabilgeschichteten Atmosphären gemessen. In Bezug auf veröffentlichte Arbeiten schneiden die vorhandenen Ergebnisse vergleichsweise gut ab.

Anschließend wird das System in gemischter schalldichter/kompressibler Form dargestellt, was ein kontrolliertes Einführen von Kompressibilität ermöglicht und in einem einheitlichen und uniform genauen Rahmen für die Dämpfung akustischer Wellen beim Ansetzen der thermischen Störungen am Anfang einer Simulation gebraucht wird. Außerdem kann die Methode in Daten-Assimilierung dadurch Anwendung finden, dass unbalancierte Messdaten in das numerische Modell ohne Neustart des Codes einbezogen werden können. Die vorgeschlagene Erweiterung für die implizite Behandlung des Auftriebsterms sieht den Gebrauch des Verfahrens als anpassungsfähiges Mittel für die Simulation mehrskaliger atmosphärischer Strömungen vor.

Preface

The past three and a half years have been full of good experiences mainly because of the people who have been next to me along the way.

To Prof Rupert Klein I am deeply grateful for having proposed me to work on this topic and for the keen, ceaseless interest in my project. It has been especially through our insightful scientific discussions that I have been able to find ideas and motivation to progress during my PhD. In addition, thanks to his support, I had the opportunity of taking part in international scientific meetings that have positively shaped my research profile and network alike.

I would like to thank Dr Luca Bonaventura for having believed in my potential back in the day and for having been an invaluable source of advice ever since. Further, I want to express my gratitude to him and Prof Dale Durran for the interest in my work and for reviewing this dissertation. Among the scientists with whom I discussed about my research I would especially like to thank Prof Frank Giraldo, Dr Piotr Smolarkiewicz, and Dr Nigel Wood.

The five-weeks stay at the Isaac Newton Institute for Mathematical Sciences in Cambridge were a very productive and enriching time. Therefore I want to thank the Institute and the organizers of the "Multiscale Numerics for the Atmosphere and Ocean" Programme for their support.

In the Geophysical Fluid Dynamics group I have found a welcoming and stimulating work environment. I would especially like to thank my colleagues Linda Michalk, Ariane Papke, Dr Romain Nguyen Van Yen, Dr Nikki Vercauteren, and Dr Stefan Vater, whom I also thank for the interest in my work and for providing the data for the simple acoustic wave test.

Matthias Waidmann, Dr Stephan Gerber, and Prof Michael Oevermann have patiently answered loads of questions. For that and for providing the coding platform my project rests on, I am grateful to them.

Warren O'Neill has been a great friend and fellow traveller in our everyday work life and from him I have learnt a lot about the meaning of working together. Some of the material in this thesis is contained in the paper [16]. I thank Dr Almut Gassmann, Dr Hilary Weller, Dr Ronny Petrik, and another anonymous reviewer for the very useful feedback they have given on my work.

The Berlin Mathematical School and the Dahlem Research School have provided a great environment to pursue my postgraduate studies and I am deeply grateful for the support received.

I also want to mention here the teachers who inspired me the most during my studies, and still do: Prof Maurizio Turlon, Dr Paolo Guiotto, Prof Francesco Paccanoni, Prof Franco Cardin, Prof Francesco Fassò, Prof Sandro Salsa, and Prof Alfio Quarteroni.

And then I thank Giuliana and Leopoldo, to whom I owe all I am, and Julia, the sun of my days.

Contents

1

Introduction

This dissertation concerns the construction and validation of a conservative numerical method of second-order accuracy for the fully compressible simulation of terrestrial atmospheric flows at low Mach number, with seamless access to pseudo-incompressible dynamics. This introductory chapter aims to describe the scientific background and scope of the work as well as to make a case for pursuing the present development.

1.1 Atmospheric flows, the stiffness problem and soundproof models

The terrestrial atmosphere provides the arena for a vast range of physical processes and their interactions on a variety of spatial and temporal scales. The spatial scale extends from thousandths of millimetres for cloud processes to tens of thousands of kilometres for planetary waves, the temporal scale from microseconds to weeks [62]. Restricting to time intervals up to ten days, Numerical Weather Prediction (NWP) focuses on integrating a mathematical model of atmospheric dynamics with the assimilated observations as initial data, thereby providing a forecast for the future state of the atmosphere.

As a point of reference, the numerical model in operation at the European Centre for Medium-Range Weather Forecasts (ECMWF, [52]) currently employs a global resolution of 16 km and issues 10-day forecasts produced in one hour. The vast dimensions in play and the operational constraints have sparked a long-standing quest for efficiency in the research on atmospheric numerical models.

As far as fluid dynamics is concerned, the most comprehensive mathematical model for the simulation of atmospheric motion is given by the three-dimensional nonhydrostatic fully compressible equations under the effect of gravity. They model conservation of mass, momentum and energy and admit solutions in the form of acoustic waves, gravity waves, and inertial motions [36,50]. The latter are the chief interest of NWP in the troposphere, where reference advective velocities u are usually taken in the range of 10–30 m s^{-1}. Considering a reference value of $c \approx 330$ m s^{-1} for the speed of sound waves, one sees that $u \ll c$, so that the motions of interest in weather and climate studies are weakly compressible low Mach number flows, where the Mach number is defined as the ratio $M = u/c$. More formally, in the low Mach number regime and with $M \to 0$ the compressible equations undergo a signal speed problem as a scale separation arises between flow velocities and the speed of sound.

Explicit numerical discretizations of fully elastic models are subject to the stability condition [28]

$$\frac{(|u| + c)\Delta t}{\Delta x} \leq 1. \tag{1.1}$$

At a given spatial resolution Δx, condition (1.1) enforces the use of a time step size Δt severely constrained by the speed of acoustic waves, which thus cause numerical stiffness. However, in most meteorological situations, sound waves have small amplitudes and are rapidly balanced. For this reason, their effects are generally deemed to be of negligible physical significance in NWP and climate studies.

A first solution adopted to solve the stiffness problem has consisted in using analytical approximations to the fully compressible model that do not feature the terms responsible for acoustics. To this category belong the soundproof models traditionally employed for small-scale phenomena such as convection. The Boussinesq model [20] neglects density perturbations in the mass and momentum equation, yet retains them in the buoyancy term. Anelastic models [10, 75, 84] assume low Mach number, small density variations on a time-independent background state, and linearize the pressure gradient term in the momentum equation. Time evolution is removed from the mass continuity equation, which takes the form of a divergence constraint.

Durran's pseudo-incompressible model [34] assumes low Mach number and small pressure perturbations on a time-independent hydrostatic background state, thereby only suppressing density perturbations due to pressure variations. The pressure equation becomes a divergence constraint and a pseudo-incompressible energy is conserved that features the internal energy of the background state. Unlike other soundproof formulations, the pseudo-incompressible model does not require any a priori assumption on the size of density perturbations and features the unapproximated momentum equation.

In soundproof models, the pressure is not coupled to the density via an equation of state as in the fully compressible model. Rather, it is responsible for fulfilling the divergence constraint that replaces the continuity equation for anelastic models and the energy equation for the pseudo-incompressible model. Numerical formulations of soundproof models forgo acoustics-related limitations by construction and require at each time step the discrete solution of the elliptic problem associated with the divergence constraint. The reader is referred to [30, 36, 62] for recent reviews and further discussion.

Because of their underlying assumptions on pressure and density variations, soundproof models have traditionally been considered unapplicable to modelling at synoptic and larger scales. However, their theoretical regime of validity was recently extended [63] to realistic thermal stratifications across the troposphere for horizontal scales less than 100 km, while the use of pseudo-incompressible equations for the study of stratospheric gravity-wave breaking was justified in [1]. EULAG model users [88, 89, 97, 109, 114] have been working successfully with soundproof models to simulate baroclinic waves on synoptic scales.

At synoptic and larger scales, where motions can be described as small perturbations over a hydrostatically balanced state, hydrostatic models have generally been employed that assume a small ratio of

horizontal to vertical length scales. Vertically propagating sound waves are filtered by construction and hydrostatic balance replaces the vertical momentum equation. Hydrostatic models are still largely used in operations: the mentioned ECMWF forecasts are the results of runs in hydrostatic mode and several research codes (cfr. the ICON model [125]) are commonly tested in their hydrostatic versions before undertaking non-hydrostatic validation tests.

In view of the good performance of reduced soundproof models on small scales and hydrostatic models on large scales, efforts have focused on providing hydrostatic codes with nonhydrostatic modules [53] or anelastic models with hydrostatic extensions. For the pseudo-incompressible model, constraints on the variation of density and hydrostatic reference state have been relaxed in [35]. Anelastic and hydrostatic dynamics have been joined in [7] through the definition of a quasi-hydrostatic density and employed in cloud-scale simulations in [69].

The whole range of reduced formulations suitable for modelling at particular scales, together with geostrophic and hydrostatic balances, can be asymptotically obtained as singular limit regimes of the fully compressible system [60, 62].

1.2 Numerical strategies for compressible atmospheric flows

The other way to overcome the efficiency problem given by sound waves in the low Mach number regime is to discretize the fully elastic model with numerical methods free of acoustics-driven constraints. In fact, nonhydrostatic fully compressible approaches hold sway in atmospheric research codes and operational or semi-operational dynamical cores, as, for example, NUMA [58], DUNE [21], the models in use at NCAR [105, 132], ECMWF [52] and the UK Met Office [31, 111, 133], and others. We refer to [112] for an extensive review of numerical methods for nonhydrostatic models.

In this context, split-explicit methods [67, 102, 131] employ subcycling to integrate acoustic waves and advection with different time steps. Runge-Kutta methods are traditionally used for the integration of slow processes and forward-backward integration for the fast ones. In operations, such a strategy is employed in the WRF [104] and NICAM [99] models and in the COSMO model in use at the German weather service [8, 9]. Generalizations have aimed at improving accuracy and efficiency of both the "fast" and the "slow" integration parts [68, 129] and at avoiding the divergence damping needed to stabilise the scheme [54]. Horizontally explicit, vertically implicit discretizations are presented in [41, 119]. Yet another approach is to consider fully implicit discretizations as done in [92].

In semi-implicit (IMEX) models, firstly introduced in the nonhydrostatic equations in [116], fast modes are handled implicitly by solving three-dimensional elliptic problems at each time step, thus allowing for a treatment of slow advective modes subject to stability constraints independent of the speed of sound and gravity waves [18, 29, 37, 45, 93, 96, 115]. In order to improve efficiency in semi-implicit models, some of the mentioned studies employ semi-Lagrangian techniques that sidestep condition (1.1) altogether

by discretizing the material derivative in the momentum equation. Regarding spatial discretizations, in the recent years continuous and discontinuous Galerkin approaches have been gaining popularity that enable high-order conservative integration and appear to be well-suited for mesh refinement techniques [58, 78, 101, 118]. As noted in [112], the procedure leading to the formulation of the elliptic problem in semi-implicit approaches is akin to the path followed to obtain the pressure elliptic problems associated with the divergence constraint in anelastic and pseudo-incompressible models.

1.3 The case for a blended soundproof-compatible solver

Because of the potential efficiency gains coming along with reduced analytical formulations, the community of atmospheric modellers has tested soundproof and hydrostatic models in relation to the fully compressible model in order to ascertain the respective behaviour. In an investigation based on normal mode analyses, the authors of [32] championed the fully compressible system for general use in atmospheric modelling at all scales. This has called for models of the fully compressible dynamics in which waves at different speeds are numerically handled. In the analysis of [32], the pseudo-incompressible model emerged as the best soundproof candidate for NWP at small horizontal scales on the order of tens of kilometres. A more recent study including the mentioned unified models [7] is presented in [33].

However, computational studies with different numerical models at small [80] and large [108] scales have failed to draw clear-cut conclusions, as "the differences due to the higher-order truncation error [. . .] overwhelm the differences due to the analytic formulation of the governing equations" [110].

With increasing computing capabilities currently in the region of petaflops and the advancement brought about by massively parallel architectures, flow patterns at increasingly smaller scales are becoming accessible to direct numerical simulation [85]. Recently, the authors of [126, 127] reported significant forecast improvements with convection-permitting nonhydrostatic runs up to global resolutions of 2.5 km, foreshadowing major changes in the understanding of subgrid-scale parametrizations. Such a context makes of arguable interest the ability to operate multiple analytical formulations within a single numerical framework.

Despite their indisputable merits, there is still a need for discussion on various aspects of the modelling approaches available at the present time. First, virtually all of the existing semi-implicit or split-explicit approaches resort to some form of numerical damping for stability reasons. Examples include off-centring the discretization towards an implicit treatment in semi-implicit models and divergence damping in split-explicit models. Such choices benefit the operational schemes especially in long-time simulations but inevitably affect their overall formal accuracy. In particular, this leaves the challenge open of running stable, second-order accurate numerical discretizations free of artificial forms of damping.

Moreover, most of the mentioned formulations feature model equations written in terms of small perturbations over a hydrostatically-balanced background state. In the model currently in use at the UK Met Office, the background state used is the state of the atmosphere at the previous time step [133]. Working

with perturbations offers the arguable advantage of not having to worry about violations of hydrostatic balance at the discrete level in the implementation. The downside is that such a choice introduces a degree of arbitrariness in the implementation.

A related aspect in the framework of a model for multiple characteristic scales concerns balanced data assimilation. Computational simulations never exactly track the evolution of the considered system. Hence, data assimilation is used for exploiting observational data at regular time intervals to set up initial data for the next simulation period. Directly importing data from a local weather station to adjacent grid points disregards the aforementioned balances of the sound modes. Filtering the data with respect to sound modes while minimally distorting the dynamics remains an open problem.

Considering this background and the mentioned issues, the present study aims at answering the following research questions:

1. Is it possible to construct a semi-implicit fully compressible numerical scheme of second-order accuracy compatible with the soundproof dynamics in the relevant regimes?

2. Is the obtained scheme applicable to gravity-driven flows without reference to a prescribed background state?

3. What is the performance of the model in terms of accuracy and stability? When applied to neutrally and thermally stratified benchmarks, does it stand comparison with established approaches?

4. Can we exploit the soundproof compatibility to build a blended soundproof-compressible model operating across the range of zero to low Mach numbers via easy switching? What benefit does the obtained discretization bring in the filtering of acoustic waves in the first stages of thermal simulations?

5. Which further avenues of research does the proposed scheme open up?

To this end, a dry semi-implicit flow solver will be constructed that extends the pseudo-incompressible framework of [61] to weakly compressible dynamics. Written in non-perturbational form and in terms of density, momentum density, and a modified pressure variable, the compressible model is obtained with the simple addition of the time derivative term to the pseudo-incompressible divergence constraint.

The conservative two-time-level finite-volume method [59, 100, 122] uses a two-step solution strategy. A first explicit step considers an auxiliary hyperbolic system and yields second-order accurate scalars. The stability condition for the first step solely hinges on the advection flow speed in the regime of scales considered. The use of fluxes not compliant with the modified divergence constraint is corrected in an implicit step with the solution of a Helmholtz elliptic problem for the cell-centred pressure increments. A final Helmholtz problem for node-centred pressure increments yields stable and second-order accurate momenta, thus correcting the use of the old-time-level pressure in the momentum equation of the predictor step.

Compressibility is handled in the implicit step via the inclusion of a zero-order term in the elliptic equations that corresponds to the time derivative term in the modified pressure equation. Hence, the proposed

extension implies virtually no efficiency overhead with respect to the pseudo-incompressible version. In addition, at the end of each time step, the compressible solver features a pressure synchronization enforcing the ideal gas equation of state at the discrete level. A well-balancing framework [19] is adopted for the discretization of the buoyancy term that avoids the subtraction of a hydrostatically balanced background state.

The performance of the compressible scheme is evaluated in a number of cases. First, the scheme is validated on the advection of a smooth rotating vortex, where accuracy properties are studied and the quadratic convergence rate is verified. The case of a simple acoustic wave is then considered that highlights the compressibility features of the scheme. Next, the behaviour of the scheme is assessed in the simulation of atmospheres at rest and gravity-driven thermal bubbles in neutrally and stably-stratified atmospheres. Obtained results are stable and accurate as compared with published studies on nonhydrostatic fully compressible numerical models.

After that, by exploiting the modular character of the proposed implementation, model equations are cast in a blended compressible/pseudo-incompressible fashion that allows for a controlled handling of compressibility via easy switching. The resulting formulation is shown to be of advantage in damping acoustic imbalances generated in the initial stages of fully compressible thermal simulations. The filtering of acoustics is realized by running the model in pseudo-incompressible mode for some time steps, then gradually transitioning to fully compressible dynamics with some hybrid time steps.

The fully compressible extension developed in the present work follows the mindset of the aforementioned theoretical studies [32, 33]. The test cases considered in the present work only cover the range of small to meso-scale flows, where the fully compressible and pseudo-incompressible models yield very similar results [16]. However, the compressible module is a necessary advancement over the pseudo-incompressible model with a view to comparing the present numerical scheme with published work on numerical methods for the fully compressible equations.

In addition, because of the modular character of the compressible extension, the scheme automatically accesses the reduced dynamics in the small-scale setting. Reduced soundproof models remain at present a very active field of study [107] and have also been employed to simulate stellar dynamics [6, 22, 82, 120]. The approach taken in the present work has the advantage of keeping the valuable information from the soundproof dynamics while discretizing the fully compressible system.

The adoption of a projection-like approach for the compressible system not only comes by extension of the ideas presented in [61] and [43, 100, 122], but is also justified by the great deal of studies in the literature employing projection methods for the simulation of low-speed flows [5, 13, 14, 26, 27]. In particular, the work [3] introduced a second elliptic solver in the correction step.

Thanks to their conservation properties, finite volume methods are also well-established in atmospheric modelling in general and for the simulation of nonhydrostatic fully compressible equations in particular, see, e.g., [2, 71, 73, 83, 128]. In the present work, second-order accuracy is achieved working with nonper-

turbational quantities via linear reconstructions at the interfaces for the computation of numerical fluxes.

The scheme we present is certainly not the first attempt to all-speed modelling in computational fluid dynamics. Previous investigations in this respect are presented in [17, 24, 48, 74, 79, 81, 87]. In [42] asymptotic limits were recovered by a careful identification of advective, buoyancy, and acoustic terms in fully compressible equations. The authors of [70] took an approach similar in spirit to the one presented here, though they chiefly dealt with simulation of shocks in a different framework. In [64] a unified mathematical framework was presented for the investigation of multi-scale problems with asymptotically adaptive methods. The study also featured a compressible extension of an incompressible model via parallel solution of a convection-diffusion and a sonic system, see also the discussion in [55].

Finally, we note that a similar extension to a semi-implicit compressible model was recently presented in [109] with technical differences on the discretization. For instance, the authors of [109] worked with perturbation variables and with the Exner pressure in the momentum equation. More importantly, the option of a seamless blending of the soundproof and compressible models was not explored in [109], nor was it elsewhere in the literature, to the best of our knowledge.

The blending feature we propose is particularly attractive as a balancing tool for sound waves in a data assimilation context. By adjusting the value of the model switch from zero to unity, the technique can be employed to run a simulation in pseudo-incompressible mode for some time steps, then smoothly transitioning to fully compressible dynamics. Since in the pseudo-incompressible case pressure imbalances are absent by construction, the procedure results in fully compressible runs with nearly balanced data and an effective filtering of acoustic imbalances.

1.4 Structure of the work

Chapter 2 features an overview of the governing equations and discusses the low Mach number regime and the pseudo-incompressible model. In Chapter 3 the fully compressible numerical scheme is described and validated. Chapter 4 describes the application to gravity-driven flows. The techniques used to achieve a well-balanced treatment of the buoyancy terms are detailed and the performance of the obtained discretization tested on the simulation of rising and falling thermals in a neutrally stratified environment and inertia-gravity waves in a stably stratified channel. In Chapter 5, the blended compressible-soundproof model is introduced that uses a parameter to switch between pseudo-incompressible and compressible dynamics within the same numerical framework. In Chapter 6 we give a theoretical account of an extension of the present scheme to treat buoyancy in an implicit fashion with a view to large scale tests. Chapter 7 summarizes and discusses the results in comparison with other approaches in the field and gives an overview of future avenues of research opened up by this dissertation.

2

Weakly compressible flow in the atmosphere

In this chapter we outline the equations that govern the motions of interest in the present work. First, we state the fully compressible equations for dry air under ideal gas assumptions. Second, we nondimensionalize the equations and discuss the low Mach number regime. Third, we focus on the soundproof pseudo-incompressible system. The material in this chapter is standard, therefore we refrain from reporting the derivations in full. For more details we refer the reader to standard textbooks in atmospheric fluid mechanics, e.g. [36, 50, 130].

2.1 Fully compressible equations

The fully compressible evolution of smooth adiabatic motions in the terrestrial atmosphere is modelled, in the dry inviscid case, by the following set of equations on the spatio-temporal domain $\Omega \times [0, \mathcal{T}] \subset \mathbb{R}^3 \times \mathbb{R}$:

$$\frac{\partial \rho}{\partial t} + \nabla \cdot (\rho \boldsymbol{v}) = 0, \tag{2.1a}$$

$$\frac{\partial \rho \boldsymbol{v}}{\partial t} + \nabla \cdot (\rho \boldsymbol{v} \circ \boldsymbol{v} + p\mathsf{I}) + \mathbf{f} \times \rho \boldsymbol{v} = -\rho \nabla \Phi, \tag{2.1b}$$

$$\frac{\partial E}{\partial t} + \nabla \cdot [(E + p)\boldsymbol{v}] = 0. \tag{2.1c}$$

Here Cartesian coordinates (x, y, z) are used, with t denoting the time coordinate. Vectors are denoted in boldface. In system (2.1), $\rho \in \mathbb{R}$ is the air mass density, $\boldsymbol{v} \in \mathbb{R}^3$ is the flow velocity, $E \in \mathbb{R}$ is the total energy density, $p \in \mathbb{R}$ is the pressure, and $\Phi \in \mathbb{R}$ is the gravitational potential. Furthermore, the symbols $\cdot$, $\times$, and $\circ$ denote the scalar, vector, and tensor product, respectively. The operator $\frac{\partial}{\partial t}(\cdot)$ denotes the time derivative, $\nabla \cdot \mathbf{a} = \frac{\partial a_1}{\partial x} + \frac{\partial a_2}{\partial y} + \frac{\partial a_3}{\partial z}$ is the divergence of $\mathbf{a} = (a_1, a_2, a_3)^T$, $\nabla h = (\frac{\partial h}{\partial x}, \frac{\partial h}{\partial y}, \frac{\partial h}{\partial z})^T$ is the gradient of h. $\mathbf{f} = 2\boldsymbol{\Omega}$ is the Coriolis parameter, with $\boldsymbol{\Omega} = (\Omega_x, \Omega_y, \Omega_z)$ the Earth rotation vector. I is the identity tensor.

The system (2.1) expresses the physical principles of mass conservation in (2.1a), momentum conservation, that is, Netwon's second law of motion in (2.1b), and energy conservation in (2.1c). They were formulated

by the Swiss mathematician and physicist Leonhard Euler (1707-1783).

The thermodynamics is governed by the energy equation (2.1c) and closed by an equation of state linking ρ, p and the temperature $T \in \mathbb{R}$. We consider the equation of state for a dry, calorically perfect gas:

$$T = \frac{p}{\rho R} \tag{2.2}$$

where $R = 287 \, \mathrm{J \, Kg^{-1} \, K^{-1}}$ denotes the specific gas constant for dry air. We also have $R = c_p - c_v$, with c_p and c_v the specific heat capacities at constant pressure and volume, respectively. The ratio $\gamma = c_p/c_v$ is called the dry isentropic exponent. Unless otherwise stated, in this work the value $\gamma = 1.4$ will be considered.

For the sake of validation of the proposed numerical techniques, in this thesis the following further assumptions will be made:

1. First, we will only consider the two-dimensional case. If we define x as the zonal coordinate (positive towards the east), y the meridional coordinate (positive towards the poles), and z the height coordinate over the sea level, this assumption is equivalent to considering vertical sections of the atmosphere for fixed y. In atmospheric modelling such representations are also referred to as vertical-slice models.

2. Second, we will focus on mesoscale motions on scales up to a few hundreds of kilometres for which the Coriolis term $\mathbf{f} \times \rho \boldsymbol{v}$ can be neglected. We also remark that in (2.1) the centrifugal acceleration is already neglected, since it is negligible with respect to the acceleration of gravity for the time scale of our simulations, namely up to a few tens of minutes.

3. Third, we will make the *tangent-plane approximation*, whereby the vertical unit vector (denoted with $\boldsymbol{k}$) is constant in module and direction, the gravitational acceleration has the constant value of $g = 9.8 \, \mathrm{m \, s^{-1}}$ and the gravitational potential takes the form $\Phi(z) = gz$.

Under these assumptions, the total energy density in (2.1c) is written as the sum of its kinetic, potential and internal parts as:

$$E = E_K + E_P + E_I \tag{2.3}$$

$$= \frac{1}{2} \rho \boldsymbol{v} \cdot \boldsymbol{v} + \rho g z + \rho c_v T = \frac{1}{2} \rho \boldsymbol{v} \cdot \boldsymbol{v} + \rho g z + \frac{p}{\gamma - 1} \tag{2.4}$$

where we used the equation of state (2.2) and $c_v/R = 1/(\gamma - 1)$.

The system (2.1) is closed by initial conditions on $\Omega \times \{t = 0\}$ and boundary conditions on $\partial\Omega \times [0, \mathcal{T}]$, which will be specified in the test cases considered.

2.1.1 Potential temperature and P

Using the momentum equation (2.1b) and the mass equation (2.1a), the energy equation (2.1c) with the definition (2.3) is transformed, under assumptions of smooth flow, into the following pressure equation:

$$\frac{\partial p}{\partial t} + \boldsymbol{v} \cdot \nabla p + \gamma p \nabla \cdot \boldsymbol{v} = 0. \tag{2.5}$$

Consider now an arbitrary reference value p_{ref} for the pressure. Multiplying (2.5) by $(\gamma R \rho)^{-1} (p_{\text{ref}}/p)^{\frac{\gamma-1}{\gamma}}$ and using the continuity equation (2.1a) to eliminate the divergence we get:

$$\frac{p_{\text{ref}}^{\frac{\gamma-1}{\gamma}}}{R} \left[\frac{p^{\frac{1-\gamma}{\gamma}}}{\gamma \rho} \left(\frac{\partial}{\partial t} + \boldsymbol{v} \cdot \nabla \right) p - \frac{p^{\frac{1}{\gamma}}}{\rho^2} \left(\frac{\partial}{\partial t} + \boldsymbol{v} \cdot \nabla \right) \rho \right] = 0. \tag{2.6}$$

If we define a function

$$\Theta = \frac{p_{\text{ref}}}{\rho R} \left(\frac{p}{p_{\text{ref}}} \right)^{\frac{1}{\gamma}} \tag{2.7}$$

then expression (2.6) implies:

$$\frac{D\Theta}{Dt} = 0 \tag{2.8}$$

where $\frac{D}{Dt}(\cdot) = \frac{\partial}{\partial t}(\cdot) + \boldsymbol{v} \cdot \nabla (\cdot)$ is the material derivative, that is the time derivative measured along the fluid trajectories. The variable Θ is the *potential temperature* and it is the temperature that an air parcel initially at pressure p and density ρ attains after an adiabatic compression or expansion to the reference pressure p_{ref}. Equation (2.8) is commonly used as the energy equation in atmospheric modelling studies and expresses the fact that Θ is a conserved quantity of adiabatic motions.

The potential temperature offers insight into the stratification properties of the underlying atmosphere. A neutrally stratified atmosphere is obtained for $\partial \Theta / \partial z = 0$, a stably (resp. unstably) stratified atmosphere for $\partial \Theta / \partial z > 0$ (resp. $\partial \Theta / \partial z < 0$). For a stably stratified atmosphere, the Brunt-Väisälä, or buoyancy, frequency

$$N^2 = \frac{g}{\Theta} \frac{\partial \Theta}{\partial z} \tag{2.9}$$

is a measure of the strength of the stratification.

Using the definition of potential temperature (2.7) in the pressure equation (2.5), we see that the quantity:

$$P = \rho \Theta = \frac{p_{\text{ref}}}{R} \left(\frac{p}{p_{\text{ref}}} \right)^{\frac{1}{\gamma}} \tag{2.10}$$

satisfies the following conservation law:

$$\frac{\partial P}{\partial t} + \nabla \cdot (P\boldsymbol{v}) = 0. \tag{2.11}$$

In agreement with [61], Equation (2.11) will be used as the energy equation throughout the present work. In view of the mentioned assumptions and transformations, the system of fully compressible equations takes the following form:

$$\frac{\partial \rho}{\partial t} + \nabla \cdot (\rho \boldsymbol{v}) = 0, \tag{2.12a}$$

$$\frac{\partial \rho \boldsymbol{v}}{\partial t} + \nabla \cdot (\rho \boldsymbol{v} \circ \boldsymbol{v} + p\mathsf{I}) = -\rho g \boldsymbol{k}, \tag{2.12b}$$

$$\frac{\partial P}{\partial t} + \nabla \cdot (P \boldsymbol{v}) = 0. \tag{2.12c}$$

The system is closed by the equation of state (2.2) or, equivalently, (2.10). Equations (2.12) in two dimensions are the subject of the numerical method proposed in the present work. We remark that the system (2.12) is only valid in differential form under the assumptions of sufficient regularity, that is, at least continuity of the variables and of the first derivatives. The integral form of the conservation laws (not reported here) is valid in the presence of singularities. We refer to [39, 72] for related discussion. The motions of our concern do not involve shocks or singularities so that, assuming sufficient regularity, we can use the differential formulation and perform the mentioned operations.

System (2.12) admits solutions in the form of waves. To assess the properties of these waves, the system is linearized decomposing the variables in a basic state plus a perturbation. For an isothermal basic state, wave solutions exist whose frequency ω and horizontal wavenumber k satisfy a dispersion relation. The analysis is standard and we refer to textbooks for the derivation [36, 38]. A schematic view of the dispersion diagram is given in Figure 2.1 for the nonhydrostatic stratified case and $\omega, k > 0$. The regions where wave solutions exist are the diagonal line and the grey-shaded regions.

Dispersion curves of sound waves and gravity waves lie in the upper and lower region, respectively. The boundaries of the regions are the dispersion curves corresponding to zero vertical wavenumber. For dry air, sound waves have a lower frequency threshold of $1.11N$, while gravity waves have an upper frequency threshold of N. In the rotating frame of reference of the Earth, gravity waves have an additional lower frequency threshold at $\omega = f$. Finally, the diagonal line has slope c and represents Lamb waves, which are horizontally propagating sound waves.

2.2 Dimensionless equations and the low Mach number regime

To gain insight into the weakly compressible dynamics, we nondimensionalize the equations. For the rest of the chapter we refer to [59, 60, 100]. Let us define reference time, length, velocity, density and pressure as t_{ref}, l_{ref}, v_{ref}, ρ_{ref}, and p_{ref}, respectively. These quantities can be combined to form dimensionless numbers. An example is the Mach number:

$$M = \frac{v_{\mathrm{ref}}}{\sqrt{p_{\mathrm{ref}}/\rho_{\mathrm{ref}}}} = \frac{v_{\mathrm{ref}}}{c_{\mathrm{ref}}}, \tag{2.13}$$

which measures the importance of compressibility in the fluid. c_{ref} is the reference speed of sound. Furthermore, we denote with h_{sc} the pressure scale height, that is the height over which the pressure varies significantly with respect to its value at sea level. The Froude number is defined as
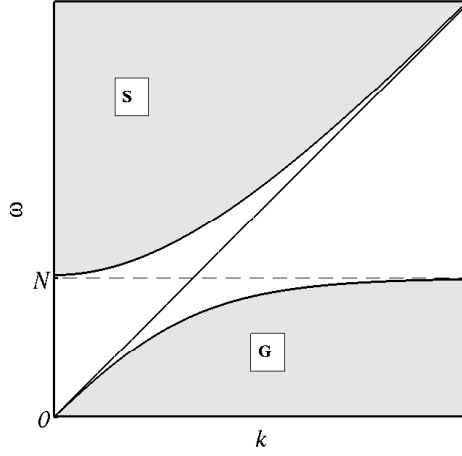
Figure 2.1: Dispersion diagram for a nonhydrostatic stratified atmosphere. The region marked with "S" contains the dispersion curves of sound waves, the region marked with "G" contains the dispersion curves of gravity waves.

$$Fr = \frac{v_{\mathrm{ref}}}{\sqrt{gh_{\mathrm{sc}}}}. \tag{2.14}$$

Using hydrostatic balance and the reference quantities, we observe that:

$$\frac{\partial p}{\partial z} = -\rho g \quad \Rightarrow \quad p_{\mathrm{ref}} \approx h_{\mathrm{sc}}\rho_{\mathrm{ref}}g. \tag{2.15}$$

If we further assume the vertical and horizontal scales of the motions to be comparable, $h_{\mathrm{sc}} = l_{\mathrm{ref}}$, we have $M = Fr$. To nondimensionalize (2.12) we write the dimensionless variables with primes, so that $t = t_{\mathrm{ref}}t'$, $x = l_{\mathrm{ref}}x'$, and so on.

Factoring out the reference values and dropping the primes, we obtain the System (2.12) in dimensionless form:

$$\frac{\partial \rho}{\partial t} + \nabla \cdot (\rho \boldsymbol{v}) = 0, \tag{2.16a}$$

$$\frac{\partial \rho \boldsymbol{v}}{\partial t} + \nabla \cdot \left(\rho \boldsymbol{v} \circ \boldsymbol{v} + \frac{1}{M^2}p\mathsf{I} \right) = -\frac{1}{M^2}\rho \boldsymbol{k}, \tag{2.16b}$$

$$\frac{\partial P}{\partial t} + \nabla \cdot (P\boldsymbol{v}) = 0. \tag{2.16c}$$

Systems (2.12) and (2.16) for $M \neq 0$ are hyperbolic. In the case of (2.16), this means that the Jacobian matrix of the flux function $\boldsymbol{f}$ for the homogeneous part:

$$\boldsymbol{f} = \begin{pmatrix} \rho \boldsymbol{v} \cdot \boldsymbol{n} \\ (\rho \boldsymbol{v} \circ \boldsymbol{v} + \frac{1}{M^2}p\mathsf{I})\boldsymbol{n} \\ P\boldsymbol{v} \cdot \boldsymbol{n} \end{pmatrix} \tag{2.17}$$

is diagonalizable and has real eigenvalues [72]. Here $\boldsymbol{n}$ is an arbitrary unit vector. The eigenvalues are:

$$\lambda_1 = \lambda_2 = \boldsymbol{v} \cdot \boldsymbol{n}, \ \lambda_{3,4} = \boldsymbol{v} \cdot \boldsymbol{n} \pm \frac{c}{M}. \tag{2.18}$$

$\lambda_{3,4}$ are the finite speeds of propagation of acoustic waves. In an acoustic wave, density and pressure rise following flow convergence via Equations (2.16a), (2.16c) and the equation of state. The resulting pressure gradient sets the fluid in motion, whereupon the cycle starts again.

As noted in the introduction, flows of interest in the atmosphere develop at a speed much lower than the speed of sound. Therefore, we now study the system (2.16) in the limit $M \to 0$. A rigorous asymptotic derivation can be found, e.g. in [77]. Here we follow [60] and expand the pressure variable in a thermodynamic and perturbational part as $p = \overline{p} + M^2 p' + o(M^2)$. The zero Mach number, variable density flow equations read, neglecting gravity for the moment:

$$\frac{\partial \rho}{\partial t} + \nabla \cdot (\rho \boldsymbol{v}) = 0, \tag{2.19a}$$

$$\frac{\partial \rho \boldsymbol{v}}{\partial t} + \nabla \cdot (\rho \boldsymbol{v} \circ \boldsymbol{v} + p' \mathsf{I}) = 0, \tag{2.19b}$$

$$\nabla \cdot \boldsymbol{v} = 0. \tag{2.19c}$$

In the limit $M \to 0$ pressure perturbations of order $O(M^2)$ affect the velocity at leading order, the pressure equation becomes the elliptic constraint (2.19c), and the speed of acoustics diverges. Mathematically, the last fact marks the transition from the hyperbolic compressible system, with finite speed of signal propagation, to the elliptic incompressible system, where adjustments are instantaneous. In the incompressible system, pressure and density are not linked by the equation of state (2.2). Instead, pressure perturbations p' are responsible for the enforcement of the divergence constraint (2.19c).

2.3 The pseudo-incompressible approximation

The pseudo-incompressible model was first proposed by Durran [34] and is obtained in the low Mach number regime, decomposing the pressure into:

$$p = \overline{p}(z) + p', \quad \text{with} \quad \frac{p'}{\overline{p}(z)} \ll 1 \ \text{and} \ \frac{\partial \overline{p}}{\partial z} = -\overline{\rho} g \tag{2.20}$$

and assuming that the density's dependence on pressure is limited to $\overline{p}$. The pseudo-incompressible equations read:

$$\frac{\partial \rho}{\partial t} + \nabla \cdot (\rho \boldsymbol{v}) = 0, \tag{2.21a}$$

$$\frac{\partial \rho \boldsymbol{v}}{\partial t} + \nabla \cdot (\rho \boldsymbol{v} \circ \boldsymbol{v} + p \mathsf{I}) = -\rho g \boldsymbol{k}, \tag{2.21b}$$

$$\nabla \cdot (\overline{P} \boldsymbol{v}) = 0 \tag{2.21c}$$

where $\overline{P} = p_{\text{ref}}/R(\overline{p}/p_{\text{ref}})^{1/\gamma}$. To express the fact that in the system (2.21) the density only depends on $\overline{p}$, a "pseudo-density" ρ^* is used instead of ρ in [34]. In our case, with an abuse of notation we keep using ρ without the asterisk to denote the "pseudo-density". For more details on the derivation of the pseudo-incompressible model see [16, 34, 61]. We remark that Durran's formulation was based on Exner pressure $\pi = (p/p_{\text{ref}})^{R/c_p}$ and potential temperature Θ. In fact, in [66] a thermodynamically consistent formulation of system (2.21) was proposed that retains the effect first-order density perturbations in the gravity term. For the purposes of comparison of our proposed fully compressible discretization, system (2.21) will be meant whenever reference is made in the present work to pseudo-incompressible runs. A thorough analysis and comparison of fully compressible results with system (2.21) and its thermodynamically consistent extension is presented in [16].

The pseudo-incompressible model converges to the zero-Mach number model (2.19) in the small-scale limit as shown in [61]. Both models (2.19) and (2.21) feature a divergence constraint with unmodified mass balance equation. In addition, the pseudo-incompressible model does not require modification of the momentum equation and conserves a pseudo-energy, defined as in (2.3) but with ρ^* instead of ρ in the mechanical energy part and the background hydrostatic pressure values in the internal energy part.

The compressible system (2.12), whose numerical solution is the subject of the present work, and the pseudo-incompressible system (2.21) only differ by the time derivative term in the energy equation. A numerical scheme extending the pseudo-incompressible framework of [61] to fully compressible dynamics is the object of the next chapter.

3

A semi-implicit, soundproof-compatible weakly compressible numerical method

In this chapter we describe the semi-implicit finite volume method employed for the discretization of the compressible equations. The scheme is an extension of the soundproof pseudo-incompressible solver presented in [61]. Unlike [61] and most approaches in the literature, the pressure gradient term in the momentum equation is written in terms of the pressure and density, instead of Exner function and potential temperature. The predictor-corrector method features a stability constraint which solely hinges on the advecting speed, thus forgoing the acoustics-induced inherent stiffness of the fully compressible model. Compressibility is implemented in the form of an added zero-order term in the elliptic correction equations and binding the energy and pressure by imposing the equation of state at the discrete level. In order to assess its stability and accuracy, the method is tested on the advection of a small-scale smooth axisymmetric vortex without gravity. Furthermore, acoustic wave simulations validate the use of the numerical strategy to simulate weakly compressible dynamics.

3.1 Numerical framework

We consider Equations (2.12) from Chapter 2 in a spatio-temporal domain $\Omega \times [0, \mathcal{T}] \in \mathbb{R}^2 \times \mathbb{R}$. The discrete solution of (2.12) is obtained through the iteration of the following steps at each time loop:

- An explicit step advects density, momentum, and P from t^n to t^{n+1}. In this step, the pressure gradient in the momentum equation is taken at the old time level and the fluxes are not consistent with the pressure equation (2.12c). Variables are already second-order-accurate after this step except for the momentum and the pressure.

- In a first implicit correction step, an elliptic Helmholtz problem is solved for cell-centred pressure increments. The solution accounts for consistency with the pressure equation and corrects the advecting and energy fluxes.

- In a second correction step, another elliptic Helmholtz problem is solved for node-centred pressure increments. The solution is used to correct the cell-centred momenta — that were only first-order-accurate after the predictor step — and yields a full second-order-accurate discretization.

The discrete model is implemented in the following spatio-temporal framework: the simulation interval $[0, \mathcal{T}]$ is divided into N subintervals, with $t^0 = 0$, $t^{n+1} = t^n + \Delta t^{n+1}$ for $n = 0, 1 \ldots, N-1$, with Δt^n denoting the time step employed at the $n+1$-th loop subject to the condition $\sum_{n=0}^{N-1} \Delta t^{n+1} = \mathcal{T}$. See below for the time step choice.

The spatial domain Ω is divided into computational cells $C_{i,j}$ (finite volumes), with $i = 1, \ldots, \mathcal{N}_x$; $j = 1, \ldots, \mathcal{N}_z$ in the Cartesian grid arrangement shown in Figure 3.1, where the interfaces are marked with I. The setting is readily extended to three dimensions. The conserved variables ρ, ρv, P are set at cell centres. Pressure is located at the grid nodes, i.e. the centres of the dual cells $\overline{C}_{i+1/2, j+1/2}$ (shaded in gray in Figure 3.1) over which the second elliptic problem is solved.
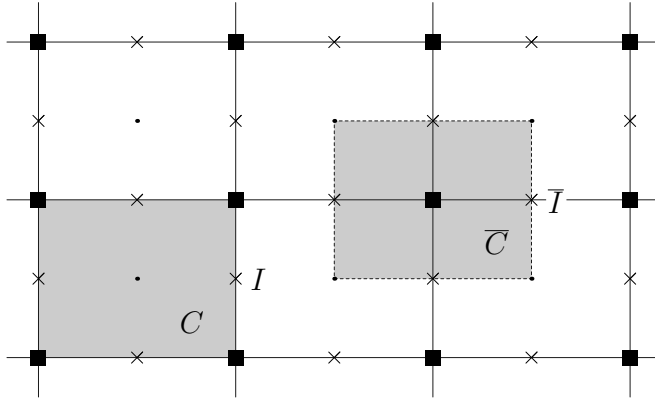

Figure 3.1: Computational grid. Solid lines define cells; dashed lines define dual cells, used for the second correction. Dots, squares and crosses denote cell centres, nodes, and interface centres, respectively.

3.1.1 Predictor

As in [61], the first explicit sub-step solves the following auxiliary hyperbolic system:

$$\frac{\partial \rho}{\partial t} + \nabla \cdot (\rho v) = 0, \tag{3.1a}$$

$$\frac{\partial \rho v}{\partial t} + \nabla \cdot (\rho v \circ v + p^n \mathsf{I}) = -\rho g \boldsymbol{k}, \tag{3.1b}$$

$$\frac{\partial P}{\partial t} + \nabla \cdot (P v) = 0. \tag{3.1c}$$

With respect to (2.12), the pressure gradient in the momentum equation (3.1b) is kept at the old-time level, thereby neglecting dynamical effects of the pressure at this stage.

Space discretization

We write equations 3.1 in the following form, which highlights the conserved variables, the flux function and the source term:

$$\boldsymbol{u}_t + \nabla \cdot [\boldsymbol{f}(\boldsymbol{u})] = \boldsymbol{s}(\boldsymbol{u}) \tag{3.2a}$$

$$\boldsymbol{u}(\boldsymbol{x}, t) := \begin{pmatrix} \rho \\ \rho\boldsymbol{v} \\ P \end{pmatrix} \qquad \boldsymbol{f}(\boldsymbol{u}) := \begin{pmatrix} \rho\boldsymbol{v} \\ \rho\boldsymbol{v} \circ \boldsymbol{v} + p^n \mathsf{I} \\ P\boldsymbol{v} \end{pmatrix} \qquad \boldsymbol{s}(\boldsymbol{u}) := \begin{pmatrix} 0 \\ -\rho g\boldsymbol{k} \\ 0 \end{pmatrix}. \tag{3.2b}$$

Numerical integration of the system (3.2a) is carried out with a finite volume method, see [72] for an introduction.

Discrete variables are defined as approximations of cell averages set at the centres of the cells $C_{i,j}$. In vector form:

$$\boldsymbol{U}_C^n = \begin{pmatrix} \rho_C \\ (\rho\boldsymbol{v})_C \\ P_C \end{pmatrix} \approx \frac{1}{|C|} \int_C \boldsymbol{u}(\boldsymbol{x}, t^n) \, d\boldsymbol{x}. \tag{3.3}$$

Above, the indices i, j were dropped for simplicity, $|C|$ denotes the cell volume and variables have been considered at the time level t^n. We then define numerical fluxes and discrete source terms that approximate the spatial and temporal integral of the functions $\boldsymbol{f}(\boldsymbol{u})$ and $\boldsymbol{s}(\boldsymbol{u})$ on the cell interfaces and volumes, respectively:

$$\boldsymbol{F}_I^{n+\frac{1}{2}}(\boldsymbol{u}) \approx \frac{1}{\Delta t |I|} \int_{t^n}^{t^{n+1}} \oint_I \boldsymbol{f}(\boldsymbol{u}) \cdot \boldsymbol{n} \, d\ell \, dt \qquad \boldsymbol{S}_C^{n+\frac{1}{2}}(\boldsymbol{u}) \approx \frac{1}{\Delta t} \int_{t^n}^{t^{n+1}} \int_C \boldsymbol{s}(\boldsymbol{u}) \, d\boldsymbol{x} \, dt \tag{3.4}$$

where I denotes a cell interface and $|I|$ its measure. Different options are available for the computation of numerical fluxes. We use an upwind method with piecewise linear reconstruction at the interfaces for second-order accuracy [72]. In particular, as in [61] but with technical differences on the upwinding, numerical fluxes are computed with reference to the flux of the energy variable $P = \rho\Theta$. To illustrate, we consider the fluxes in the horizontal direction.

1. Interface velocity is determined by averaging the neighbouring cell values:

$$u = \frac{1}{2}(u_L + u_R) \tag{3.5}$$

where u_L and u_R are linearly reconstructed to obtain a second-order accurate discretization. At the interface $(x_{i+1/2}, y_j)$, the reconstructed values read:

$$u_L = u_i + \frac{1}{2}\psi(u_i - u_{i-1}, u_{i+1} - u_i) \tag{3.6a}$$

$$u_R = u_{i+1} - \frac{1}{2}\psi(u_{i+1} - u_i, u_{i+2} - u_{i+1}) \tag{3.6b}$$

where ψ is a slope function. In particular, we have:

$$\psi(a, b) = \frac{a+b}{2} \tag{3.7}$$

for centred slopes, whereas

$$\psi(a,b) = \begin{cases} \dfrac{2ab}{a+b}\chi(\min(a/b, b/a)) & (\mathrm{sgn}(ab) > 0) \\ 0 & \text{otherwise} \end{cases} \qquad \chi(r) = 1 + r(1-r)(1-r^2) \qquad (3.8)$$

for van Leer-like limited slopes (see [61]). The results presented in this work have all been obtained without using limiters.

2. The obtained velocities are used to compute the upwind fluxes for the P variable as:

$$F(P) = F^+(P) + F^-(P) \tag{3.9}$$

where:

$$F^+(P) = P_L \max(\boldsymbol{u}, 0), \qquad F^-(P) = P_R \min(\boldsymbol{u}, 0) \tag{3.10}$$

and P_L and P_R denote linearly reconstructed energy values at the interface obtained with the formulas (3.6).

3. Fluxes for the remaining advected quantities $\phi \in \{\Theta^{-1}, \boldsymbol{v}\Theta^{-1}\}$ are referred to the carrier flux $P\boldsymbol{v}$ and derived using (3.9) to get:

$$F(\phi) = F^+(P)\phi_L + F^-(P)\phi_R \tag{3.11}$$

where the subscripts denote reconstructed values.

4. For the momentum equation, i.e. $\phi = \boldsymbol{v}/\Theta$ in (3.11), the pressure contribution is obtained by interpolating the adjacent nodal values to the cell interface centres. In the no-gravity case the interpolation amounts to a simple average, while in a stratified setting a modification will be required, which is described below, see Section 4.4.2. Similarly, the gravity source term in (3.2b) will be handled within the well balanced framework analyzed in Chapter 4.

Time discretization

As for the time discretization, different two-time-level explicit schemes are available and have been implemented. The common idea is that discrete variables at the new time level are obtained subtracting the net outflow fluxes at the interface from the old-time-level ones and adding the contributions from the source terms. With the definitions of (3.3) and (3.4), we obtain:

$$\boldsymbol{U}_C^{n+1,*} = \boldsymbol{U}_C^n - \frac{\Delta t}{|C|} \sum_{I \in \partial C} \boldsymbol{F}_I^{n+\frac{1}{2},*}(\boldsymbol{U}) + \frac{\Delta t}{|C|} \boldsymbol{S}_C^{n+\frac{1}{2},*}(\boldsymbol{U}), \tag{3.12}$$

where the sum runs over the interfaces I that make up the boundary ∂C of cell C. Furthermore, we have denoted with a superscripted asterisk quantities computed in the predictor step.

Runge-Kutta time integration

Let us define:

$$L(\boldsymbol{U}) = -\frac{1}{|C|} \sum_{I \in \partial C} \boldsymbol{F}_I^{n+\frac{1}{2}}(\boldsymbol{U}) + \frac{\Delta t}{|C|} \boldsymbol{S}_C^{n+\frac{1}{2},*}(\boldsymbol{U}). \tag{3.13}$$

For simplicity, in all our tests we employed a two-stage second-order strong stability preserving Runge-Kutta method [46], which reads:

$$\boldsymbol{U}_C^{(1)} = \boldsymbol{U}_C^n + \Delta t L(\boldsymbol{U}_C^n) \tag{3.14a}$$

$$\boldsymbol{U}_C^{n+1,*} = \frac{1}{2}\boldsymbol{U}_C^n + \frac{1}{2}\boldsymbol{U}_C^{(1)} + \frac{1}{2}\Delta t L\left(\boldsymbol{U}_C^{(1)}\right). \tag{3.14b}$$

This corresponds to the classical Heun's method (see [36]), which amounts to computing the new time-level variables using an average of the initial and first-stage slopes. Above, $\boldsymbol{U}_C^{(1)}$ denotes the first-stage solution. Therefore, the discrete version of the auxiliary system solved in the predictor step reads:

$$\rho_C^{n+1,*} = \rho_C^n - \Delta t \left(\widetilde{\nabla} \cdot \left(P\boldsymbol{v}\,\Theta^{-1}\right)\right)_C^{n+\frac{1}{2},*}, \tag{3.15a}$$

$$(\rho\boldsymbol{v})_C^{n+1,*} = (\rho\boldsymbol{v})_C^n - \Delta t \left(\widetilde{\nabla} \cdot \left(P\boldsymbol{v} \circ \boldsymbol{v}\Theta^{-1} + p^n\mathsf{I}\right)\right)_C^{n+\frac{1}{2},*} - \Delta t\, g\boldsymbol{k}\, (\rho)_C^{n+\frac{1}{2},*}, \tag{3.15b}$$

$$P_C^{n+1,*} = P_C^n - \Delta t \left(\widetilde{\nabla} \cdot (P\boldsymbol{v})\right)_C^{n+\frac{1}{2},*}. \tag{3.15c}$$

Above, the $n+1/2, *$ superscript denotes time averaging in agreement with the chosen time integrator. Once again, we stressed the use of the old-time-level pressure value in the momentum equation. Furthermore, the following symbolic notation was used to denote the balance of a numerical flux $\boldsymbol{f}$ across cell boundaries ∂C,

$$\widetilde{\nabla} \cdot \boldsymbol{f}_C = \frac{1}{|C|} \sum_{I \in \partial C} \boldsymbol{f}_I \cdot \boldsymbol{n} = \frac{1}{|C|} \oint_{\partial C} \boldsymbol{f} \cdot \boldsymbol{n}\, d\ell + O(\Delta x^2). \tag{3.16}$$

The validation tests in this chapter will be carried out with the homogeneous scheme. We refer to Section 4.3 below for details on the discretization of the gravity source term in the predictor. We finally remark that further experiments have been tried with the Strang splitting strategy used in [61]. Results in that direction are still object of research and are not further discussed in the present work.

Time step choice

The time discretization used in (3.15) is explicit. As such, the employed time step Δt must be chosen in abidance by the so-called CFL stability condition [28]. As we neglect the effect of dynamic pressure — and thus, explicit compressibility — in the momentum equation, the condition reads for one dimensional flow:

$$\frac{\|u\|_\infty \Delta t}{\Delta x} \leq 1 \tag{3.17}$$

where Δx is the grid size and $\|u\|_\infty$ the maximum of the advecting flow velocity. A choice of the pair $(\Delta x, \Delta t)$ corresponds to a numerical speed $u_{\text{num}} = \Delta x / \Delta t$. Condition (3.17) states that, for an explicit scheme to be stable, only those pairs $(\Delta x, \Delta t)$ are admissible that correspond to a u_{num} greater or equal to the advecting velocity u of the flow under consideration. The ratio $\text{CFL} = u/u_{\text{num}}$ is called the Courant number and condition (3.17) states that explicit schemes are stable for $\text{CFL} \leq 1$ (see [90] for a thorough explanation).

The extension of condition (3.17) to vectorial velocities in a multidimensional setting reads, for an upwind method [72]:

$$\frac{\|\boldsymbol{v}\|_1 \Delta t}{\Delta x} \leq 1 \tag{3.18}$$

where $\|\cdot\|_1$ is the discrete L^1 norm (see below, Section 3.2) and $\boldsymbol{v}$ the vector of the maximum velocity values in the coordinate directions.

Our scheme features an adaptive choice of the time step. In particular, we dynamically compute the time step size at each time loop according to:

$$\Delta t = \min\left(\Delta t_{\text{I}}, \Delta t_{\text{A}}, \Delta t_{\text{B}}\right) \tag{3.19}$$

where Δt_{I} is an externally imposed value of the time step. Δt_{A} is the advective time step:

$$\Delta t_{\text{A}} = \frac{\text{CFL}\,\Delta x}{\max_\Omega\left(\|\boldsymbol{v}\|_2\right)}, \tag{3.20}$$

where $\text{CFL} \leq 1$ and $\|\cdot\|_2$ is the discrete L^2 norm. Δt_{B} is a buoyancy-dependent time step which will be discussed below, see Section 4.3. Dynamically adaptive time stepping is standard in computational fluid dynamics and its implementation is straightforward [72].

At the end of the predictor step:

- the scalar variables ρ, Θ and P are second-order-accurate (see [61]);
- the advecting fluxes $(P\boldsymbol{v})^{n+1/2}$ do not provide a stable update for P, i.e., they are not compliant with the energy equation (2.12c) in the fully compressible model. This corresponds to the violation of the divergence constraint (2.21c) in the pseudo-incompressible context;
- the use of the old-time level pressure prevents the scheme from being fully second-order accurate.

3.1.2 Corrector

In the second, implicit part of our scheme, we build two Helmholtz elliptic problems for the pressure increments. The solution of the first elliptic problem corrects the advecting fluxes, which were computed neglecting a semi-implicit discretization of the energy equation at the half time level. The solution of the second elliptic problem, located at the grid nodes, corrects the use of the old time-level pressure in the predictor and adjusts the momenta to second-order-accurate values. In both problems, the difference with

the Poisson equation obtained in the incompressible formulation [61, 100, 122] lies in an additional zero-order term which accounts for the energy time derivative in Equation (2.12c). The added term is obtained using a discrete version of the equation of state (2.10) that links P with p and builds compressibility into the scheme, i.e., the dynamical effect of pressure upon density.

First step

The first correction step corresponds to the MAC-projection in projection methods for incompressible flows [12, 49]. Consider the energy equation at the half time level:

$$\left[\frac{\partial P}{\partial t} + \nabla \cdot (P\boldsymbol{v})\right]^{n+\frac{1}{2}} = 0. \tag{3.21}$$

Since the predictor has second-order temporal accuracy, the advecting fluxes $(P\boldsymbol{v})^{n+\frac{1}{2},*}$ provide a first-order accurate update at the half time level. This is sufficient to maintain second-order accurate advection. However, for stability reasons it is necessary to add the effect of the new-time-level pressure gradient into the advecting flux. Consider the momentum equation (2.12b). Multiplying it by Θ we obtain:

$$(P\boldsymbol{v})_t + \nabla \cdot (P\boldsymbol{v} \circ \boldsymbol{v}) + \Theta\nabla p + Pg\boldsymbol{k} = \rho\boldsymbol{v}\left(\Theta_t + \boldsymbol{v} \cdot \nabla\Theta\right) = 0 \tag{3.22}$$

where we used mass (2.12a) and energy (2.12c) conservation equations to cancel the second expression. Integrating then (3.22) in time over a half time step we find:

$$(P\boldsymbol{v})^{n+\frac{1}{2}} = (P\boldsymbol{v})^n - \frac{\Delta t}{2}\left[\nabla \cdot (P\boldsymbol{v} \circ \boldsymbol{v})\right]^{n+\frac{1}{4}} - \frac{\Delta t}{2}(Pg\boldsymbol{k})^{n+1/4} - \frac{\Delta t}{2}(\Theta\nabla p)^{n+\frac{1}{4}} \tag{3.23a}$$

$$= (P\boldsymbol{v})^n - \frac{\Delta t}{2}\left[\nabla \cdot (P\boldsymbol{v} \circ \boldsymbol{v})\right]^{n+\frac{1}{4}} - \frac{\Delta t}{2}(Pg\boldsymbol{k})^{n+1/4} - \frac{\Delta t}{2}\Theta^{n+\frac{1}{4}}\nabla\left[\frac{1}{2}\left(p^n + p^{n+\frac{1}{2}}\right)\right] \tag{3.23b}$$

$$= (P\boldsymbol{v})^n - \frac{\Delta t}{2}\left[\nabla \cdot (P\boldsymbol{v} \circ \boldsymbol{v})\right]^{n+\frac{1}{4}} - \frac{\Delta t}{2}(Pg\boldsymbol{k})^{n+1/4} - \frac{\Delta t}{2}\Theta^{n+\frac{1}{4}}\nabla\left\{\frac{1}{2}\left[2p^n + (p^{n+\frac{1}{2}} - p^n)\right]\right\} \tag{3.23c}$$

$$= (P\boldsymbol{v})^n - \frac{\Delta t}{2}\left[\nabla \cdot (P\boldsymbol{v} \circ \boldsymbol{v})\right]^{n+\frac{1}{4}} - \frac{\Delta t}{2}(Pg\boldsymbol{k})^{n+1/4} - \frac{\Delta t}{2}\Theta^{n+\frac{1}{4}}\left[\nabla p^n + \frac{1}{4}\nabla\left(p^{n+1} - p^n\right)\right] \tag{3.23d}$$

$$= (P\boldsymbol{v})^{n+\frac{1}{2},*} - \frac{\Delta t}{2}\Theta^{n+\frac{1}{2},*}\nabla\frac{\delta p}{4}. \tag{3.23e}$$

In the derivation above, we used the following relations

$$p^{n+\frac{1}{2}} - p^n = \frac{1}{2}\left(p^{n+1} - p^n\right) + O\left((\Delta t)^2\right), \quad \Theta^{n+\frac{1}{2},*} = \Theta^{n+\frac{1}{4}} + O\left((\Delta t)^2\right) \tag{3.24}$$

for $\Delta t \to 0$ and we defined as $\delta p = p^{n+1} - p^n$ the unknown cell-centred pressure increment. The asterisk denotes predicted values. Next, consider the energy equation (3.21). We observe that:

$$\left(\frac{\partial P}{\partial t}\right)^{n+\frac{1}{2}} = \left(\frac{\partial P}{\partial p}\frac{\partial p}{\partial t}\right)^{n+\frac{1}{2}} = \left(\frac{\partial P}{\partial p}\right)^{n+\frac{1}{2},*}\frac{\delta p}{\Delta t} + O\left((\Delta t)^2\right) \tag{3.25}$$

where we used $P^{n+\frac{1}{2}} = P^{n+\frac{1}{2},*} + O\left((\Delta t)^2\right)$ for $\Delta t \to 0$. To compute the derivative of the energy with respect to pressure, we use the equation of state in the form (2.10). Inserting then (3.23e) and (3.25) into (3.21) we obtain the discrete elliptic problem:

$$\frac{1}{R\gamma\Delta t}\left(\frac{P^{n+\frac{1}{2},*}R}{p_{\text{ref}}}\right)_C^{1-\gamma}\delta p + \widetilde{\nabla}\cdot[(P\boldsymbol{v})^{n+\frac{1}{2},*}]_C - \widetilde{\nabla}\cdot\left[\frac{\Delta t}{2}\Theta^{n+\frac{1}{2},*}\nabla\frac{\delta p}{4}\right]_C = 0 \tag{3.26}$$

that is:

$$-\frac{1}{R\gamma\Delta t}\left(\frac{P^{n+\frac{1}{2},*}R}{p_{\text{ref}}}\right)_C^{1-\gamma}\delta p + \underbrace{\widetilde{\nabla}\cdot\left[\frac{\Delta t}{8}\Theta^{n+\frac{1}{2},*}\nabla\delta p\right]_C}_{\dfrac{P_C^{n+1} - P_C^{n+1,*}}{\Delta t}} = \underbrace{\widetilde{\nabla}\cdot[(P\boldsymbol{v})^{n+\frac{1}{2}\cdot*}]_C}_{-\dfrac{P_C^{n+1,*} - P_C^n}{\Delta t}}\cdot \tag{3.27}$$

Expression (3.27) is a Helmholtz problem. Implicit compressibility is included in the zero-order term — the first on the left hand side. The term is not present in the pseudo-incompressible formulation (2.21), for which the energy equation (2.21c) is a divergence constraint that gives rise to a Poisson problem.

Note that in the expression (3.23e), since

$$(\nabla\delta p)^{n+\frac{1}{2},*} = (\nabla\delta p)^{n+\xi,*} + O\left((\Delta t)^2\right) \tag{3.28}$$

for $\xi \in [0,1]$ and $\Delta t \to 0$, any $\xi \in [0,1]$ would maintain the desired accuracy. The choice $\xi = 1/4$ corresponds to a midpoint, symplectic discretization. However, in a context of small-scale acoustics superposed on a larger-scale flow, the choice $\xi = 1/4$ prevents the solution from adjusting to the expected advective behaviour, a feature we noticed while benchmarking the code on the smooth vortex, see Section 3.2.2 below. To sidestep the issue and in view of (3.28), similarly to [121] we choose $\xi = 1$ and use, instead of (3.23e), the following expression:

$$(P\boldsymbol{v})^{n+\frac{1}{2}} = (P\boldsymbol{v})^{n+\frac{1}{2},*} - \frac{\Delta t}{2}\Theta^{n+\frac{1}{2},*}\nabla\delta p. \tag{3.29}$$

Thus, we obtain the modified Helmholtz problem:

$$-\left(\frac{\mathcal{C}_H^{n+\frac{1}{2},*}}{\Delta t}\delta p\right)_C + \widetilde{\nabla}\cdot\left[\frac{\Delta t}{2}\Theta^{n+\frac{1}{2},*}\nabla\delta p\right]_C = \widetilde{\nabla}\cdot[(P\boldsymbol{v})^{n+\frac{1}{2},*}]_C \tag{3.30}$$

where we defined:

$$\mathcal{C}_H^{n+\frac{1}{2},*} = \left(\frac{\partial P}{\partial p}\right)^{n+\frac{1}{2},*} = \frac{1}{R\gamma}\left(\frac{P^{n+\frac{1}{2},*}R}{p_{\text{ref}}}\right)^{1-\gamma}. \tag{3.31}$$

In (3.27) we highlighted that the second-order differential operator accounts for the energy correction with respect to the value $P_C^{n+1,*}$ computed by the predictor, while the right hand side represents the energy increment itself, i.e., the negative of the last term in the predictor energy equation (3.15c). The sum of these

two terms in the form of the new zero-order term explains how the Helmholtz problem accounts for stable time increments of P in the compressible framework. The effect is not present in the pseudo-incompressible model where $P = \overline{P}(z)$ and the solution of the Poisson equation projects away any pressure imbalance to yield $P^{n+1} \equiv \overline{P}$ at the discrete level up to the tolerance of the elliptic solver.

The elliptic problem (3.30) is solved on the cells C with a standard flux-based approach using the divergence theorem to write the discrete second-order operator as sum of the integrals of divergence argument across the cell interfaces. Piecewise constant data are assumed on the interfaces $I \in \partial C$ of the primary cells and the discrete divergence is computed via integration on ∂C. We refer the reader to [61] for details. A five-point stencil is used in the first projection.

With the solution of (3.30) at hand, the corrections to the advecting fluxes as of equation (3.23e) are built as:

$$\delta P \boldsymbol{v} \cdot \boldsymbol{n} = -\frac{\Delta t}{2} \Theta \nabla \delta p \cdot \boldsymbol{n} \tag{3.32}$$

and the predicted values are corrected by:

$$\rho_C^{n+1} = \rho_C^{n+1,*} - \Delta t \widetilde{\nabla} \cdot \left(\delta P \boldsymbol{v} \Theta^{-1} \right)_C \tag{3.33a}$$

$$(\rho \boldsymbol{v})_C^{n+1,**} = (\rho \boldsymbol{v})_C^{n+1,*} - \Delta t \widetilde{\nabla} \cdot \left(\delta P \boldsymbol{v} \circ \boldsymbol{v} \Theta^{-1} \right)_C \tag{3.33b}$$

$$P_C^{n+1} = P_C^{n+1,*} - \Delta t \widetilde{\nabla} \cdot \left(\delta P \boldsymbol{v} \right)_C. \tag{3.33c}$$

Here, the advected variables Θ^{-1} and $\boldsymbol{v}\Theta^{-1}$ are evaluated at $n + 1/2, *$. Further, the new momentum variable collects a second asterisk to indicate a preliminary value that needs to be updated after the second correction step. By contrast, the value of ρ and P will remain unmodified from this point on.

After stabilizing the advecting fluxes with an implicit cell-centred pressure increment, we are ready to tackle the issue of the old-time-level pressure in the momentum equation.

Second step

The use of the old-time-level pressure in the momentum equation (3.1b) makes the predictor only first-order-accurate with respect to momentum. In a second correction step, the momentum flux and the pressure are corrected to achieve stable, second-order-accurate values.

A first, straightforward route is to interpolate the solution δp of the first correction equation (3.30) from the cell centres to the interfaces. The values are then used to correct the momentum computed in (3.33b) via the following expression:

$$(\rho \boldsymbol{v})_C^{n+1} = (\rho \boldsymbol{v})_C^{n+1,**} - \frac{\Delta t}{2} \widetilde{\nabla} \cdot (\delta p \mathsf{I})_C. \tag{3.34}$$

This strategy, however, generates an unstable update. Therefore, for stability reasons we solve a second elliptic problem for a node-centred pressure variable (see also [3, 100, 122] for similar procedures).

We proceed as in the previous section and integrate the momentum equation, this time over the entire time interval $\left[t^n,\, t^{n+1}\right]$. After multiplication by Θ^{n+1} and taking into account that the scalars ρ, P, Θ have already attained their final values after the first correction, we have:

$$(P\boldsymbol{v})^{n+1} = (P\boldsymbol{v})^n - \Delta t \nabla \cdot (P\boldsymbol{v} \circ \boldsymbol{v})^{n+\frac{1}{2}} - \Delta t \, (Pg\boldsymbol{k})^{n+\frac{1}{2}} - \Delta t \Theta^{n+1} \left(\nabla p\right)^{n+\frac{1}{2}} \tag{3.35a}$$

$$= (P\boldsymbol{v})^n - \Delta t \nabla \cdot (P\boldsymbol{v} \circ \boldsymbol{v})^{n+\frac{1}{2}} - \Delta t \, (Pg\boldsymbol{k})^{n+\frac{1}{2}} - \Delta t \Theta^{n+1} \nabla \left[\frac{1}{2}(p^n + p^{n+1})\right] \tag{3.35b}$$

$$= (P\boldsymbol{v})^n - \Delta t \nabla \cdot (P\boldsymbol{v} \circ \boldsymbol{v})^{n+\frac{1}{2}} - \Delta t \, (Pg\boldsymbol{k})^{n+\frac{1}{2}} - \Delta t \Theta^{n+1} \nabla \left[\frac{1}{2}\left(2p^n + (p^{n+1} - p^n)\right)\right] \tag{3.35c}$$

$$= (P\boldsymbol{v})^{n+1,**} - \frac{\Delta t}{2}\Theta^{n+1}\nabla \delta p_\nu. \tag{3.35d}$$

In (3.35d), the two asterisks in the superscript indicate values after the first correction step. As in the first step, we replace (3.35d) in:

$$\left(\frac{\partial P}{\partial t}\right)^{n+\frac{1}{2}} + \nabla \cdot \left[\theta \, (P\boldsymbol{v})^{n+1} + (1-\theta)\,(P\boldsymbol{v})^n\right] = 0, \tag{3.36}$$

where $\theta \in [1/2, 1]$ is an off-centring parameter. In particular, a second-order-accurate trapezoidal discretization is obtained for $\theta = 1/2$, whereas for $1/2 < \theta \leq 1$ the discretization is first-order accurate. Unless otherwise stated, we will use $\theta = 1/2$ throughout. The result is the Helmholtz problem:

$$\left(-\frac{\mathcal{C}_H^{n+1}}{\Delta t}\delta p_\nu\right)_{\overline{C}} + \widetilde{\nabla} \cdot \left(\theta \frac{\Delta t}{2}\Theta^{n+1}\nabla \delta p_\nu\right)_{\overline{C}} = \widetilde{\nabla} \cdot \left[\theta(P\boldsymbol{v})^{n+1,**} + (1-\theta)(P\boldsymbol{v})^n\right]_{\overline{C}} \tag{3.37}$$

where $\mathcal{C}_H^{n+1}$ is defined as in (3.31) using the corrected value of P and we marked with δp_ν the unknown nodal pressure increment. As in the first correction step, the zero-order term on the left hand side of (3.37) accounts for compressibility, while the old/new-time-level weighting in the square bracket on the right hand side ensures consistency with a second-order-accurate discretization for $\theta = 1/2$.

The second Helmholtz problem is solved by integration over the dual cells — whose centres are the grid nodes, see Figure 3.1. A nine-point stencil is used for the discretization of the Laplacian in (3.37). The nodal values of the pressure increments define continuous piecewise bilinear pressure distributions on the primary control volumes. We integrate their gradients analytically over the boundaries $\overline{I} \in \partial\overline{C}$ of the dual cells that are centred on the grid nodes. The solution δp_ν is accordingly defined in the centres of the dual cells $\overline{C}$. We refer to [61, 122] for details.

The solution δp_ν is transferred to the centres of the cell faces via simple averaging of the two adjacent nodal values. The obtained values at the cell interfaces are then used to update the momentum to its final, second-order-accurate value via formula (3.34). The time loop is completed by the computation of the final velocity via $\boldsymbol{v}^{n+1} = (\rho\boldsymbol{v})_C^{n+1}/\rho_C^{n+1}$ and the pressure update detailed below.

We remark that the scheme constructed above conserves total mass, horizontal momentum and the total mass-weighted potential temperature P. Other variables such as total energy are not conserved by design. A related analysis is presented for the rising bubble case in Section 4.5.2. We refer to [41, 117] for related discussion.

Pressure update

A first option for the pressure update is to take the solution δp_ν to the problem (3.37) and add it to the old-time-level nodal value:

$$p^{n+1} = p^n + \delta p_\nu. \tag{3.38}$$

This is the strategy employed in the pseudo-incompressible context. However, in the compressible case this way of updating the pressure brings about instabilities in the benchmark vortex runs, see below Section 3.2.2. To solve the problem we introduce a binding option, whereby an auxiliary cell-centred pressure value p_C is computed from the final value P_C of the energy variable using the inverse of the equation of state (2.10) in discrete form:

$$p_C^{n+1} = \left(\frac{P^{n+1}}{\rho_{\text{ref}} T_{\text{ref}}} \right)^\gamma p_{\text{ref}}. \tag{3.39}$$

The obtained value is then interpolated to the nodes and yields the new value of the nodal pressure p^{n+1}.

BDF2 discretization

Similarly to what is done in [121] in a shallow water setting, we implement a multistep option for the second correction step. For the ordinary differential equation:

$$\frac{du}{dt} = L(u) \tag{3.40}$$

where L is a differential operator, the backward difference discretization of order 2 (BDF2) reads as follows [36]:

$$\frac{\frac{3}{2} u^{n+1} - 2u^n + \frac{1}{2} u^{n-1}}{\Delta t} = L(u^{n+1}). \tag{3.41}$$

The BDF2 method yields second-order accurate approximations and is widely employed in meteorological applications [36]. In [123], dispersion studies are presented on the linear acoustic equations that highlight the different numerical damping and phase speed associated with the BDF2 method in comparison with the trapezoidal method.

The momentum equation reads, neglecting the gravity term to illustrate:

$$(\rho \boldsymbol{v})^{n+1} = \frac{4}{3} (\rho \boldsymbol{v})^n - \frac{1}{3} (\rho \boldsymbol{v})^{n-1} - \frac{2}{3} \Delta t \nabla \cdot (\rho \boldsymbol{v} \circ \boldsymbol{v})^{n+1} - \frac{2}{3} \Delta t \nabla p^{n+1}. \tag{3.42}$$

Using then flux extrapolation:

$$(\rho \boldsymbol{v} \circ \boldsymbol{v})^{n+1} = (\rho \boldsymbol{v} \circ \boldsymbol{v})^{n+\frac{1}{2}} + \frac{1}{2} \left((\rho \boldsymbol{v} \circ \boldsymbol{v})^{n+\frac{1}{2}} - (\rho \boldsymbol{v} \circ \boldsymbol{v})^{n-\frac{1}{2}} \right) \tag{3.43}$$

and $p^{n+1} = p^n + \delta p_\nu$, where $\delta p_\nu = p^{n+1} - p^n$ as above, and defining the intermediate momentum update as:

$$(\rho\boldsymbol{v})^{n+1,**} = \frac{4}{3}(\rho\boldsymbol{v})^n - \frac{1}{3}(\rho\boldsymbol{v})^{n-1} - \frac{2}{3}\Delta t\left[\nabla\cdot(\rho\boldsymbol{v}\circ\boldsymbol{v})^{n+1} + \nabla p^n\right], \tag{3.44}$$

we write the momentum update at the new time level:

$$(\rho\boldsymbol{v})^{n+1} = (\rho\boldsymbol{v})^{n+1,**} - \frac{2}{3}\Delta t\nabla\delta p_\nu \tag{3.45}$$

whereupon

$$(P\boldsymbol{v})^{n+1} = (P\boldsymbol{v})^{n+1,**} - \frac{2}{3}\Delta t\Theta^{n+1,**}\nabla\delta p_\nu. \tag{3.46}$$

At time $n+1$, the energy equation reads:

$$\left(\frac{\partial P}{\partial t}\right)^{n+1} + \nabla\cdot(P\boldsymbol{v})^{n+1} = 0 \tag{3.47}$$

from which

$$\frac{\mathcal{C}_H^{n+1}}{\Delta t}\left(\frac{3}{2}\delta p_\nu - \frac{1}{2}\delta p_\nu^{old}\right) = -\nabla\cdot\left[(P\boldsymbol{v})^{n+1,**} - \frac{2}{3}\Delta t\Theta^{n+1}\nabla\delta p_\nu\right] \tag{3.48}$$

and $\delta p_\nu^{old} = p^n - p^{n-1}$. Finally, the Helmholtz equation for the pressure increment reads:

$$\left(-\frac{3\mathcal{C}_H^{n+1}}{2\Delta t}\delta p_\nu\right)_{\overline{C}} + \frac{2}{3}\Delta t\widetilde{\nabla}\cdot\left(\Theta^{n+1}\nabla\delta p_\nu\right)_{\overline{C}} = \widetilde{\nabla}\cdot(P\boldsymbol{v})_{\overline{C}}^{n+1,**} - \left(\frac{\mathcal{C}_H^{n+1}}{2\Delta t}\delta p_\nu^{old}\right)_{\overline{C}}. \tag{3.49}$$

The value of $(P\boldsymbol{v})^{n+1,**}$ on the right hand side is computed expanding (3.44) using (3.43) as follows:

$$(\rho\boldsymbol{v})^{n+1,**} = \underline{(\rho\boldsymbol{v})^n} + \frac{1}{3}(\rho\boldsymbol{v})^n - \frac{1}{3}(\rho\boldsymbol{v})^{n-1} \underline{-\Delta t\nabla\cdot(\rho\boldsymbol{v}\circ\boldsymbol{v})^{n+\frac{1}{2}}} + \frac{1}{3}\Delta t\nabla\cdot(\rho\boldsymbol{v}\circ\boldsymbol{v})^{n-\frac{1}{2}}$$
$$\underline{-\Delta t\nabla p^n} + \frac{1}{3}\Delta t\nabla p^n. \tag{3.50}$$

The underlined terms represent the momentum after the first projection in the current time step, which we call $(\rho\boldsymbol{v})_1^{n+1,**}$, so that the above expression becomes:

$$(\rho\boldsymbol{v})^{n+1,**} = (\rho\boldsymbol{v})_1^{n+1,**} + \frac{1}{3}(\rho\boldsymbol{v})^n \underline{-\frac{1}{3}(\rho\boldsymbol{v})^{n-1} + \frac{1}{3}\Delta t\nabla\cdot(\rho\boldsymbol{v}\circ\boldsymbol{v})^{n-\frac{1}{2}}}$$
$$+ \frac{1}{3}\Delta t\nabla\left(p^n - p^{n-1}\right) \underline{+\frac{1}{3}\Delta t\nabla p^{n-1}} \tag{3.51}$$

where now the underlined terms denote $-1/3$ times the momentum after the first projection in the previous time step $(\rho\boldsymbol{v})_1^{n,**}$. Finally, after multiplication by Θ_1^{n+1} we obtain:

$$(P\boldsymbol{v})^{n+1,**} = (P\boldsymbol{v})_1^{n+1,**} - \frac{1}{3}(P\boldsymbol{v})_1^{n,**} + \frac{1}{3}(P\boldsymbol{v})^n + \frac{1}{3}\Theta_1^{n+1,**}\Delta t\nabla\delta p_{old}^n. \tag{3.52}$$

Summary of the numerical scheme

For the reader's convenience, we summarize the operations performed by the numerical scheme in the following:

Algorithm 1 (Compressible scheme)**.**

Starting from compliant initial and boundary conditions:

<u>Initialization</u>

    Grid setting and input preprocessing. Then, for each time loop, **do**:

<u>Predictor</u>

   (i) Compute linearly reconstructed P and $\boldsymbol{v}$ values at the interfaces via (3.6) and compute advecting upwind fluxes of P via (3.9);

  (ii) Linearly reconstruct $1/\Theta$ and $\boldsymbol{v}/\Theta$ at the cell interfaces and compute the remaining advecting fluxes via (3.11). For the momentum, interpolate the nodal pressure values to the cell interface centres for the flux computation;

 (iii) Compute new-time-level predicted quantities using (3.15)

<u>First Correction</u>

   (i) Solve the Helmholtz equation (3.30) for cell-centred pressure increments;

  (ii) Use the solution to correct advecting fluxes via (3.33);

<u>Second Correction</u>

   (i) Solve the Helmholtz equation (3.37) for node-centred pressure increments;

  (ii) Interpolate the solution on cell interface centres and correct momentum flux via (3.34).

<u>Pressure update</u>

    Synchronise the energy and pressure via the equation of state using the binding formula (3.39);

<u>Conclusion</u>

    Post-processing and output management.

3.2 Numerical results

This section contains the validation of the semi-implicit fully compressible method. After an outline of the coding framework that we used to implement the scheme, we move on to describe the test case of the smooth vortex upon which we validated the method's properties. Comparisons between compressible and pseudo-incompressible runs are presented and convergence tests are discussed for the proposed fully compressible version. Finally, the compressible features of the scheme are tested on a simple acoustic wave.

Remark on norms

We give some definitions that will be used throughout the work. Given a function u defined on a domain $\Omega \in \mathbb{R}^m$, $m = 2$, 3 we define its L^k norm as:

$$\|u\|_k := \left(\int_\Omega |u|^k \, dx\right)^{1/k} \qquad \forall \, 1 \le k < \infty \tag{3.53a}$$

$$\|u\|_\infty := \sup_{x \in \Omega} |u(x)| \,. \tag{3.53b}$$

For discrete functions, expressions (3.53) translate into the definition of k-norm for a vector $\boldsymbol{u} = \{u_i\}_{i=1}^n$:

$$\|\boldsymbol{u}\|_k := \left(\sum_i |u_i|^k\right)^{1/k} \qquad \forall \, 1 \le k < \infty \tag{3.54a}$$

$$\|\boldsymbol{u}\|_\infty := \max_i \left(|u_i|\right) \tag{3.54b}$$

and the induced definition of matrix k-norm for a matrix $A = \{a_{ij}\}_{i=1,\ldots,l; \, j=1\ldots n}$:

$$\|A\|_k = \sup_{\mathbb{R}^n \ni \boldsymbol{x} \ne 0} \frac{\|A\boldsymbol{x}\|_k}{\|\boldsymbol{x}\|_k}. \tag{3.55}$$

3.2.1 Coding framework

The numerical model is implemented in an object-oriented C++ environment based on the SAMRAI framework [51] for mesh refinement. The compressible extension is built over an in-house flow solver originally designed for the simulation of multiphase flows developed at the Geophysical Fluid Dynamics working group in the Institute of Mathematics at Freie Universität Berlin. The solver is based on the pseudo-incompressible numerical framework presented in [61].

Since the code is fully parallelized and has built-in grid adaptivity features, its use appears to be advantageous in a number of envisaged atmospheric applications, see e.g. [11, 78]. Although for the purposes of the present study we focused our attention to two dimensional serial runs, the code is 3d-ready.

In the implementation of the scheme we made extensive use of preprocessor instructions (see e.g. [134] for details), which facilitated switching between different configurations, e.g. compressible/pseudo-incompressible, trapezoidal/bdf2 etc.

The linear systems in the correction step are solved with the Krylov-type BiCGStab method [124] with algebraic multi-grid preconditioners as included in the Hypre library [40]. The code has an option for solving with GMRES [98] but BiCGStab has been observed to give better results and therefore was used throughout. The solver tolerance was set at 10^{-12} for all of the test cases. We remark that the coding framework we use is not fully optimized. For some tests the total wallclock time is reported for reference.

As for visualization, we employed the open-source VisIt package [25]. The data were then exported into MATLAB®[1] for the production of plots. The simulations were performed on a personal computer Intel® Core™ i7-2640M CPU @2.80GHz×4, 7.7 GB RAM in double machine precision. An execution of the standard MATLAB command `eps` on this system yields the value `eps = 2.22e-16`. Source files and data are available upon request at benacchio@math.fu-berlin.de.

---

[1] Version 7.14.0.739 (2012a)

3.2.2 Smooth vortex

The first benchmark [56] consists of a travelling, axisymmetric, anticlockwise rotating vortex in the doubly periodic, unit-square-shaped domain $[0,\ 1]^2$ m^2. The initial data for density and velocity are as follows:

$$\rho(x,y,t) = \begin{cases} \rho_c + \dfrac{1}{2}(1-r^2)^6 & \text{if} \quad r < 1, \\ \rho_c & \text{otherwise} \end{cases} \tag{3.56}$$

$$u(x,y,t) = \begin{cases} -1024 \sin(\vartheta)(1-r)^6 r^6 + u_c & \text{if} \quad r < 1, \\ u_c & \text{otherwise} \end{cases} \tag{3.57}$$

$$v(x,y,t) = \begin{cases} 1024 \cos(\vartheta)(1-r)^6 r^6 + v_c & \text{if} \quad r < 1, \\ v_c & \text{otherwise.} \end{cases} \tag{3.58}$$

$$\tag{3.59}$$

where

$$\vartheta = \arctan \frac{y - y_c(t)}{x - x_c(t)}, \quad r = \frac{\sqrt{(x - x_c(t))^2 + (y - y_c(t))^2}}{R} \tag{3.60}$$

are the angular and radial coordinate for the vortex, the latter rescaled by the value of its radius held fixed at $R = 0.4$ m. The vortex is initially placed at the centre of the domain, the coordinates of the centre being $(x_c(0), y_c(0)) = (0.5, 0.5)$. The initial pressure field is computed by means of the centripetal force formula:

$$p = p_{\text{coeff}} \rho_c \left(u_c^2 + v_c^2\right). \tag{3.61}$$

In the general case of $\rho_c \neq 1/2$, the expression of the pressure coefficient in the travelling vortex as in [56] has to be modified as follows:

$$\begin{aligned} p_{\text{coeff}}(r) = 1024^2 r^{12} \Bigg[&\frac{1}{72} r^{24} - \frac{6}{35} r^{23} + \frac{15}{17} r^{22} - \frac{74}{33} r^{21} + \frac{57}{32} r^{20} + \frac{174}{31} r^{19} \\ &- \frac{269}{15} r^{18} + \frac{450}{29} r^{17} + \frac{153}{8} r^{16} - \frac{1564}{27} r^{15} + \frac{510}{13} r^{14} + \frac{204}{5} r^{13} \\ &- \frac{1}{24}(2210 - \rho_{dl}) r^{12} + \frac{12}{23}(85 - \rho_{dl}) r^{11} + \left(\frac{510}{11} + 3\rho_{dl}\right) r^{10} \\ &- \frac{4}{21}(391 + 55\rho_{dl}) r^9 + \frac{9}{40}(119 + 110\rho_{dl}) r^8 + \frac{18}{19}(25 - 44\rho_{dl}) r^7 \\ &- \frac{1}{9}(269 - 462\rho_{dl}) r^6 + \frac{6}{17}(29 - 132\rho_{dl}) r^5 + \frac{3}{16}(19 + 165\rho_{dl}) r^4 \\ &- \frac{2}{15}(37 + 110\rho_{dl}) r^3 + \frac{3}{7}(5 + 11\rho_{dl}) r^2 - \frac{6}{13}(1 + 2\rho_{dl}) r + \frac{1}{24}(1 + 2\rho_{dl}) \Bigg] \end{aligned} \tag{3.62}$$

where $\rho_{dl} = \left[1 + \frac{1}{2}(1 - r^2)^6\right] / \rho_c$. The initial data are depicted in Figure 3.2.

The density has a bulge in the centre, the velocity has a maximum absolute value of $1 + \sqrt{2}$ in the lower right part of the vortex, while pressure perturbation displays a corresponding negative bulge. Since the vortex is
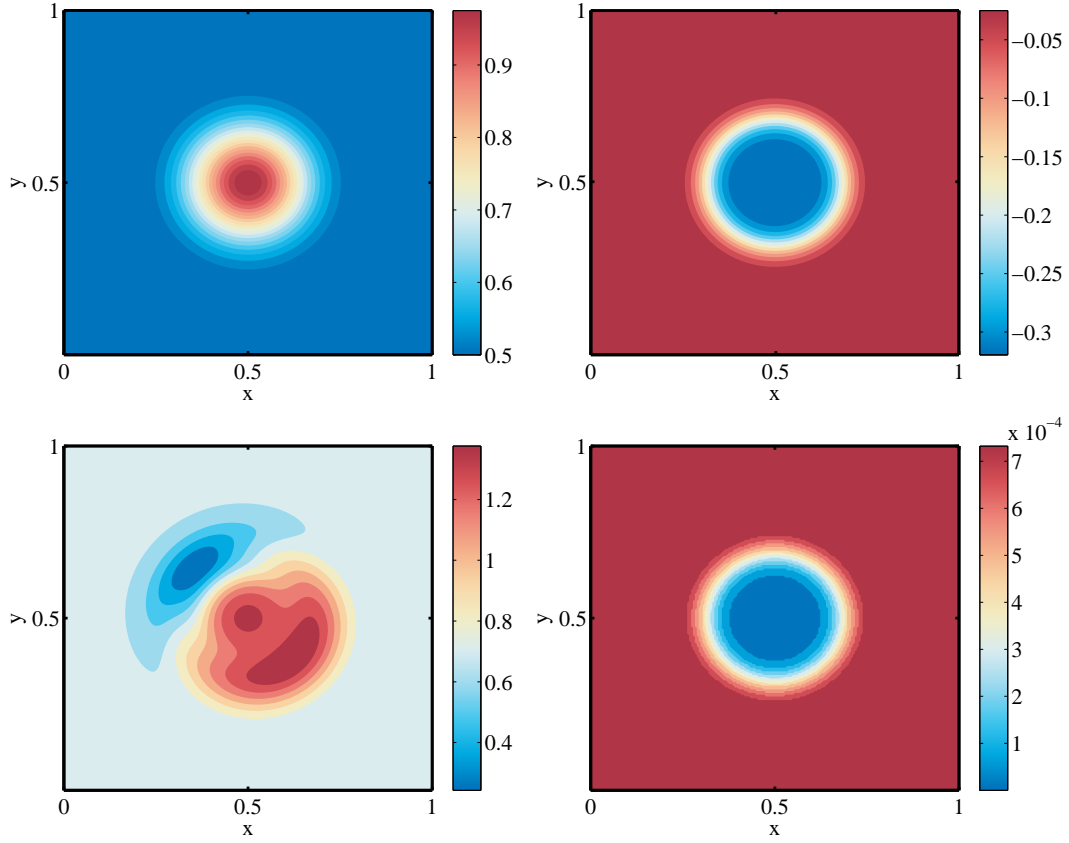
Figure 3.2: Initial data for the smooth vortex. Density (upper left), pressure perturbation (upper right), momentum magnitude (2-norm, lower left), P (lower right). Colour shading every $0.025 \, \mathrm{kg \, m^{-3}}$ in the interval $[0.525, 0.975] \, \mathrm{kg \, m^{-3}}$ for the density, every 0.025 Pa in $[-0.3, 0.025]$ Pa for the pressure. For the momentum norm, 10 shades of colour are shown in the interval $[0.2427, 1.489] \, \mathrm{kg \, m^{-2} \, s^{-2}}$. For P, the minimum value of $353.04797 \, \mathrm{kg \, K \, m^{-3}}$ was subtracted for plotting and 12 shades of colour are shown in the interval $[0, 7.93\mathrm{e}\text{-}04] \, \mathrm{kg \, K \, m^{-3}}$.

advected at constant speed (u_c, v_c), the formulas:

$$x_c(t) = 0.5 + u_c t, \quad y_c(t) = 0.5 + v_c t \tag{3.63}$$

yield the position of the centre of the vortex at all times t. In agreement with [56] we consider unitary velocity $(u_c, v_c) = (1, \, 1) \, \mathrm{m \, s^{-1}}$.

This test case case is an exact solution for both the zero Mach number incompressible equations, to which Durran's pseudo-incompressible model reduces in the absence of gravity (see [61]), and for the compressible equations initialized with consistent pressure data. Moreover, in the compressible case we derive the initial distribution for the energy P via the equation of state in (2.10).

Reference physical quantities are set as follows:

$$\rho_{\mathrm{ref}} = 0.5 \, \mathrm{kg \, m^{-3}}, \ p_{\mathrm{ref}} = 101625 \, \mathrm{Pa}, \ T_{\mathrm{ref}} = 706.098 \, \mathrm{K}, \ \gamma = 1.4, \tag{3.64}$$

corresponding to a maximum Mach number of $M_{\mathrm{max}} = \max \left(\|\boldsymbol{v}\|_2 / \sqrt{\gamma p / \rho} \right) \approx 4.52\mathrm{e}\text{-}03$. Thus in this

case the flow is very weakly compressible. The high value of T_{ref} is computed from p_{ref} and ρ_{ref} considered in [56] and enables an easier comparison with their results.

Because of the doubly periodic boundary conditions and of the unitary velocity, at $t = 1$ s and $t = 2$ s the initial configuration is to be reproduced unchanged up to second-order errors. To verify that, we consider a discrete setting with 192 grid cells in both directions, corresponding to $\Delta x = 5.21e\text{-}03$ m. The time step is determined by formula (3.20). For the sake of validation and along the lines of published literature [14], we take a safety value of CFL $= 0.45$ in (3.20). The corresponding constant time step is $\Delta t = \Delta t_A = 9.7e\text{-}04$ s. We remark that these data correspond to a sound-speed-based Courant number $\text{CFL}_S = \text{CFL}/M_{max} \approx 90.72$.

The vortex is transported by the background unitary velocity. Compressible results at $t = 1$ s and $t = 2$ s reproduce the initial configuration. Figure 3.3 displays results with the trapezoidal method in the second projection, Figure 3.4 refers to results obtained with the BDF2 option in the second projection. Left panels display results at $t = 1$ s, right panels results at $t = 2$ s. The simulation with trapezoidal method until the time $t = 2$ s (2056 time steps) had a total wallclock time of 2382.57 s. 39% of the total wallclock time was used by the predictor step and 56% by the corrector step. The simulation with BDF2 had a total wallclock time of 2369.24 s, 38% of which for the predictor step and 57% for the corrector step.

The numerical scheme is shown to advect the vortex at the correct speed. Results obtained with the pseudo-incompressible scheme (displayed for $t = 1$ s in Figure 3.5) show no noticeable difference with the compressible ones, as intended in the low Mach number regime considered. In Figure 3.5, the energy plot is not displayed since $P \equiv \overline{P}(z)$ for the pseudo-incompressible model. Note that the tripole-like shapes in the external contours at $t = 2$ s also arise in the pseudo-incompressible runs at that time (not shown) and are due to the onset of a physical instability which develops after the second round. For the sake of validation of the compressible scheme in the framework of the convergence studies detailed below, we will use the results at time $t = 1$ s.

As for the comparison of compressible and pseudo-incompressible results, a notable difference lies in the transport of P in the compressible model. As noted, the pseudo-incompressible, Poisson-equation-based correction step brings the energy distribution back to the imposed $P = \overline{P}(z)$ at each time loop by construction. By contrast, the compressible scheme simulates the full dynamics of P as an advected and conserved quantity, modelling its time derivative as in expressions (3.21) and (3.36). As shown in the graphs, in the compressible scheme the energy is transported with its shape unchanged after one and two rounds. Another related difference between the compressible and pseudo-incompressible configuration lies in the pressure adjustments at the outset of the simulation. Since the compressible scheme models the full dynamics through a midpoint, P-preserving discretization, in the first stages of runs with the compressible scheme we observed considerable adjustments to a balanced pressure distribution. This is to be expected as the fully compressible system admits acoustic solutions which our fully compressible numerical scheme simulates, albeit implicitly.
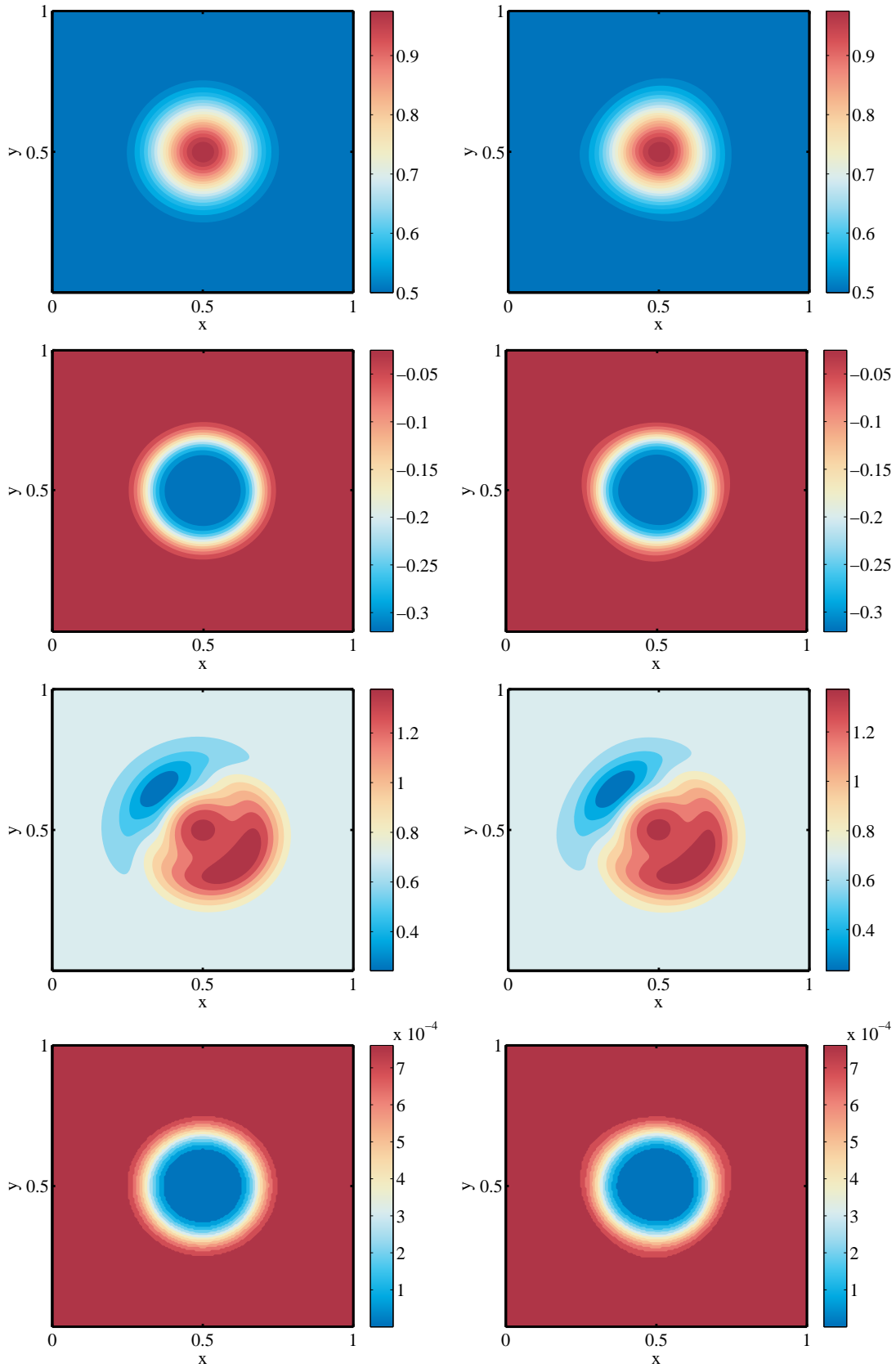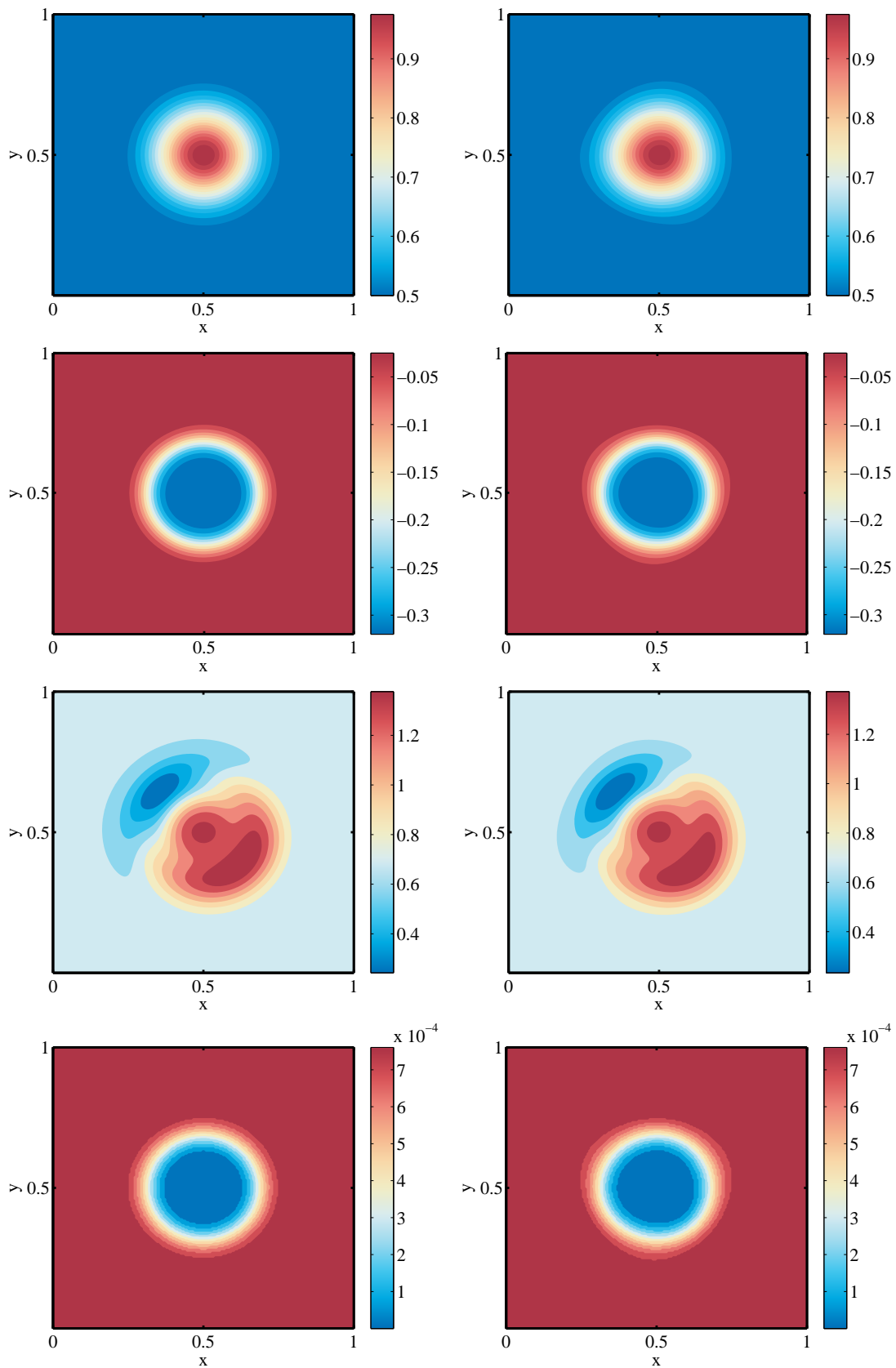
Figure 3.3: Computed results for the smooth vortex at $t = 1$ s (left panels) and $t = 2$ s (right panels), fully compressible model. Density (top row), pressure perturbation (second row), momentum magnitude (2-norm, third row), P (bottom row). Shades of colour as in Figure 3.2. Values of momentum norm are in the range $[0.2426, 1.489]$ kg m^{-2} s^{-2} at $t = 1$ s, in the range $[0.233, 1.487]$ kg m^{-2} s^{-2} at $t = 2$ s. Values of the P in the same range as Figure 3.2.

Figure 3.4: Computed results for the smooth vortex at $t = 1$ s (left panels) and $t = 2$ s (right panels), fully compressible model with BDF2 discretization in the second projection. Density (top row), pressure perturbation (second row), momentum magnitude (2-norm, third row), P (bottom row). Shades of colour as in Figure 3.2. Ranges of momentum 2-norm and P as in Figure 3.3.
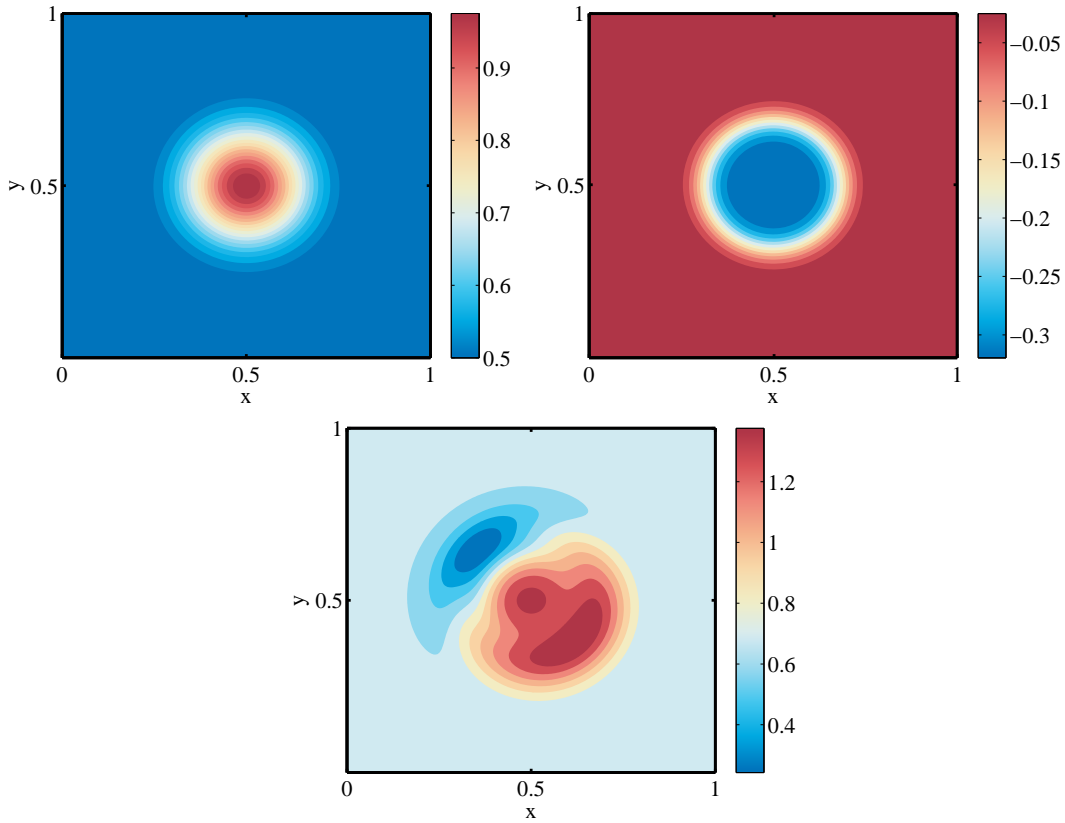
Figure 3.5: Computed results for the smooth vortex at $t = 1$ s, pseudo-incompressible model. Density (upper left), pressure perturbation (upper right), momentum magnitude (2-norm, bottom). Shades of colour as in Figure 3.2. Values of the momentum norm are in the range $[0.2428, 1.489]$ kg m^{-2} s^{-2}.

Even though these imbalances are of small amplitude, their effect can be observed in the graphs of the nodal pressure increment, solution of the second elliptic problem. In the compressible case (Figure 3.6, left panel) a sizeable asymmetry is present with respect to the pseudo-incompressible run (Figure 3.6 right panel). The difference between the two graphs mirrors the mathematical character of the compressible Helmholtz problem on the one hand and the pseudo-incompressible Poisson problem on the other. In the former, implicit compressibility is modelled by the zero order term that the latter lacks.

Indeed, at a later stage, after the acoustic waves are rebalanced, the plots of the compressible and pseudo-incompressible models look the same (not shown). We will delve into the adjustment problem in Chapter 5 while presenting blended compressible/pseudo-incompressible simulations.

Since the two elliptic Helmholtz problems (3.30) and (3.37) share the same derivation through the P equation (3.21), we expect their solutions to match. This is confirmed by the graph in Figure 3.7 which reports the nodal and cell-centred increments at $t = 0.25$ s in the compressible case. The maximum computed error in the L^∞ norm between the nodal and cell-centred pressure increment as of Figure 3.7 is less than 0.5 per cent.

While implementing the compressible scheme, the correct advection of P was a measure of key importance
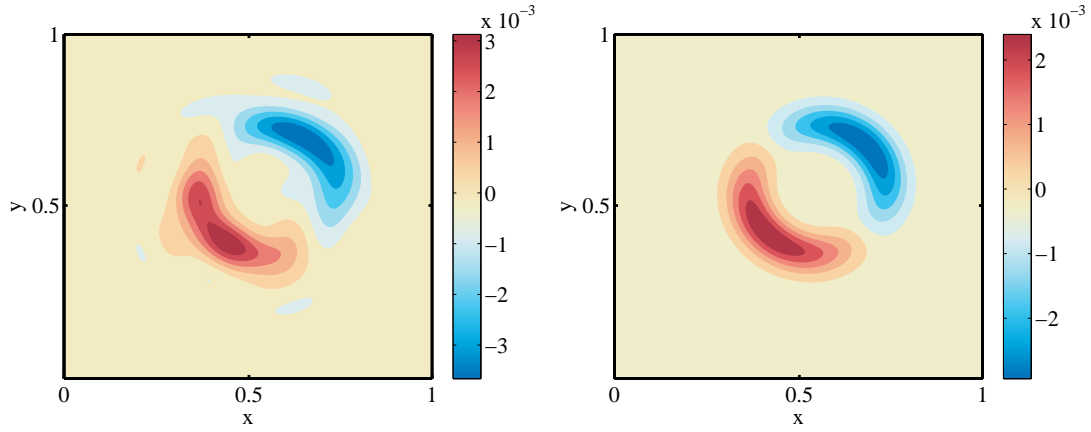
Figure 3.6: Computed nodal pressure increment for the smooth vortex at $t = 0.05$ s by the fully compressible (left) and pseudo-incompressible (right) models. 12 shades of colour are plotted in the interval $[-3.66\text{e-}03, 3.81\text{e-}03]$ Pa in the left panel and $[-2.94\text{e-}03, 2.93\text{e-}03]$ Pa in the right panel.
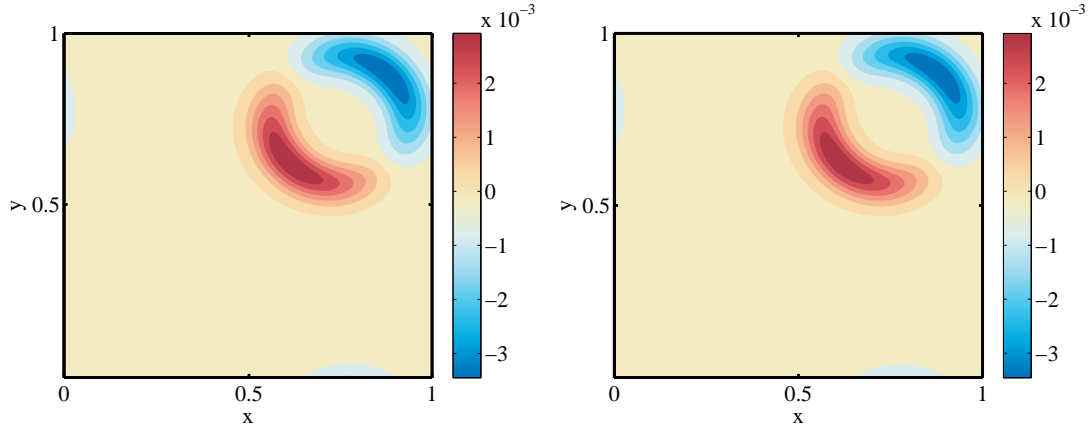

Figure 3.7: Computed nodal (left) and cell-centred (right) pressure increment for the smooth vortex at $t = 0.25$ s, fully compressible model. 12 shades of colour are plotted in the interval $[-3.45\text{e-}03, 3.45\text{e-}03]$ Pa for the nodal pressure and $[-3.45\text{e-}03, 3.46\text{e-}03]$ Pa for the cell-centred pressure increments

to assess the validity of the approach. In fact, simple pressure update via adding the solution of the second correction equation triggered a slight asymmetry in the P distribution. This made us devise the energy-pressure binding (3.39) which eventually enabled us to produce the results in Figure 3.3 discussed above.

Convergence tests

In this section, we present the results of convergence studies we performed to evaluate the accuracy properties of our numerical scheme. The soundproof model described in [61] is second-order-accurate. In order to check that our compressible extension maintains the quadratic rate of error decay with grid refinement, we will consider the vortex case. Notwithstanding the smoothness of the initial data, it is important to verify the theoretical accuracy in this idealized situation, before we can proceed with the analysis of buoyancy-driven flows in Chapter 4. First, we define the error measures we will be employing. Given the discrete value ϕ_N

and a reference value ϕ with $\phi = \rho$, $\rho\|\boldsymbol{v}\|_2$, p, the relative error $\mathcal{E}_\phi$ of ϕ_N with respect to ϕ in the k-norm is defined as:

$$\mathcal{E}_\phi(\phi_N) := \frac{\|\phi_N - \phi\|_k}{\|\phi_N\|_k} \qquad \forall\, 1 \le k \le \infty \tag{3.65}$$

see above for the definition of norms, expressions (3.53) and their calculation in a discrete setting, expressions (3.54) and (3.55). In practice, the values on a discrete two-dimensional grid will be encoded in matrices and the standard Matlab® function `norm` will be used to compute the errors listed below. Moreover, we define as rate of convergence $\sigma_\phi(\phi_N)$ of the discrete solution corresponding to the grid refinement from a $N/2 \times N/2$ grid to a $N \times N$ grid the following quantity:

$$\sigma_\phi(\phi_N) := \log_2 \frac{\mathcal{E}_\phi(\phi_{N/2})}{\mathcal{E}_\phi(\phi_N)} \tag{3.66}$$

where the errors on the numerator and denominator are computed in the same norm. Therefore, checking the second-order accuracy of our method, we aim at σ_ϕ values of 2.

Convergence test with initial data as exact solution

As in [56], we develop our convergence analysis from the computed data at time $t = 1$ s, displayed above in Figure 3.3 for the compressible model. The convergence tests refer to the version with trapezoidal integration in the second projection. In [56], the errors are computed taking the initial data as exact solution. We could have also used the computed data after a few time steps and then shift them to compare them with the initial data. However, in this way we would not have been able to assess, for instance, the correctness of the implementation of the periodic boundary conditions.

An investigation of the results using the grid sizes as of [56] reveals super-optimal rates for the pressure p and sub-optimal rates for density ρ and momentum magnitude $\rho\|\boldsymbol{v}\|_2$ (Table 3.1 and Figure 3.8). Hereafter, for simplicity $\mathcal{E}_\phi$ and σ_ϕ defined in (3.65) and (3.66) will not feature the argument ϕ_N in the tables and figures. Moreover, the value of the rate σ_ϕ is to be understood as the one computed between the $(N \times N)$-sized grid and the $(N/2 \times N/2)$-sized grids.

Table 3.1: Variation of relative L^2 and L^∞ errors and convergence rates for the smooth vortex case as of Fig. 3.8, fully compressible runs. Errors computed as numerical solution at $t = 1$ s on grids with N^2 cells with respect to initial data.

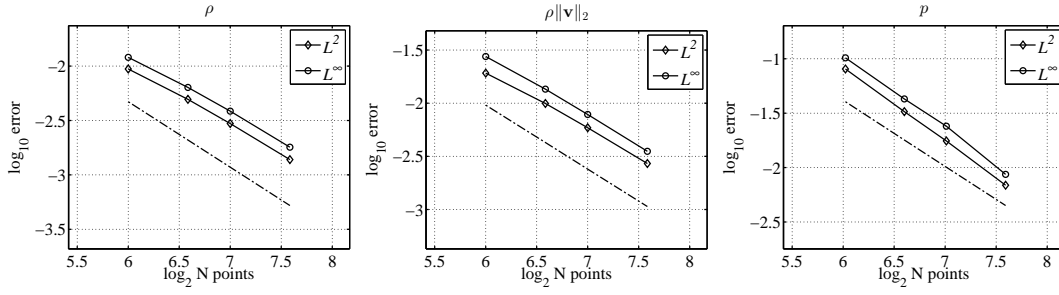|	N	$\mathcal{E}_\rho$	σ_ρ	$\mathcal{E}_{\rho\|\boldsymbol{v}\|_2}$	$\sigma_{\rho\|\boldsymbol{v}\|_2}$	$\mathcal{E}_p$	σ_p
	64	1.20e-02		2.75e-02		1.02e-01	
	96	6.36e-03		1.36e-02		4.28e-02	
L^∞	128	3.85e-03	1.64	7.84e-03	1.81	2.40e-02	2.11
	192	1.80e-03	1.83	3.53e-03	1.94	8.66e-03	2.32
	N	$\mathcal{E}_\rho$	σ_ρ	$\mathcal{E}_{\rho\|\boldsymbol{v}\|_2}$	$\sigma_{\rho\|\boldsymbol{v}\|_2}$	$\mathcal{E}_p$	σ_p
	64	9.41e-03		1.92e-02		8.06e-02	
	96	4.95e-03		9.94e-03		3.26e-02	
L^2	128	2.97e-03	1.67	5.88e-03	1.71	1.76e-02	2.22
	192	1.38e-03	1.84	2.71e-03	1.88	6.88e-03	2.26

Figure 3.8: Density (left), momentum magnitude (middle) and pressure (right) convergence story for the smooth vortex case, fully compressible runs. Errors of computed solutions at $t = 1$ s on grids with N^2 cells with respect to initial data. The dashed-dotted line represents quadratic slope.

In order to check whether the sub-optimal rates are a product of our compressible extension, we ran the tests on a pseudo-incompressible version of the code (Table (3.2) and Figure (3.9)). The results mirror the previous ones, ruling out a difference due to the simulation of compressibility.

Table 3.2: Variation of relative L^2 and L^∞ errors and convergence rates for the smooth vortex case as of Fig. 3.9, pseudo-incompressible runs. Errors computed as numerical solution at $t = 1$ s on grids with N^2 cells with respect to initial data.

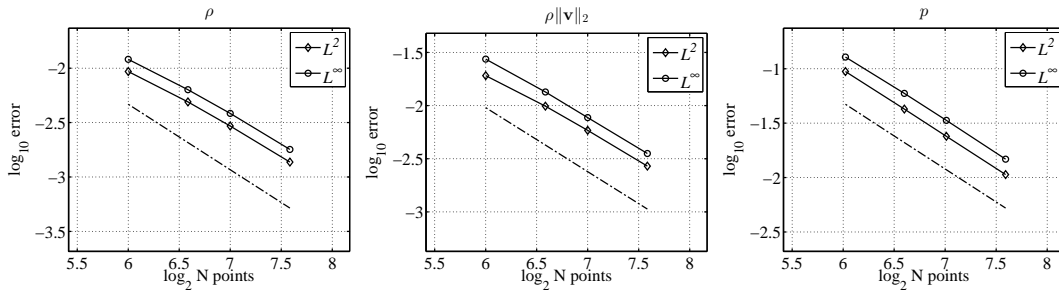|	N	$\mathcal{E}_\rho$	σ_ρ	$\mathcal{E}_{\rho\|v\|_2}$	$\sigma_{\rho\|v\|_2}$	$\mathcal{E}_p$	σ_p
	64	1.21e-02		2.74e-02		1.28e-01	
	96	6.34e-03		1.34e-02		5.94e-02	
L^∞	128	3.84e-03	1.65	7.72e-03	1.83	3.35e-02	1.96
	192	1.79e-03	1.82	3.54e-03	1.92	1.47e-02	2.02
	N	$\mathcal{E}_\rho$	σ_ρ	$\mathcal{E}_{\rho\|v\|_2}$	$\sigma_{\rho\|v\|_2}$	$\mathcal{E}_p$	σ_p
	64	9.32e-03		1.91e-02		9.43e-02	
	96	4.90e-03		9.89e-03		4.26e-02	
L^2	128	2.94e-03	1.67	5.85e-03	1.71	2.39e-02	2.00
	192	1.37e-03	1.84	2.70e-03	1.88	1.07e-02	2.01

Figure 3.9: Density (left), momentum magnitude (middle) and pressure (right) convergence story for the smooth vortex case, pseudo-incompressible runs. Errors of computed solutions at $t = 1$ s on grids with N^2 cells with respect to initial data. The dashed-dotted line represents quadratic slope.

Then, we consider again the compressible model and repeat the analysis for finer grids (Table 3.3 and Figure

3.10). Convergence rates for density and momentum magnitude are seen to approach the desired value. This is to be expected as the pressure adjustments in the initial stages of the simulations as seen in Figure 3.6 have smaller effects on the computed solution at final time on finer grids. In particular, this was observed in the decaying amplitude of generated pressure waves in the compressible case at the outset for finer grids (not shown). However small though this amplitude, it appears to contribute to worsening the rate of convergence of the pressure error, notably in the 384-to-768 segment, where it nearly approaches a linear rate.

Table 3.3: Variation of relative L^2 and L^∞ errors and convergence rates for the smooth vortex case as of Fig. 3.10, fully compressible runs. Errors computed as numerical solution at $t = 1$ s on grids with N^2 cells with respect to initial data.

|	N	$\mathcal{E}_\rho$	σ_ρ	$\mathcal{E}_{\rho\|\boldsymbol{v}\|_2}$	$\sigma_{\rho\|\boldsymbol{v}\|_2}$	$\mathcal{E}_p$	σ_p
	64	1.20e-02		2.75e-02		1.02e-01	
	96	6.36e-03		1.36e-02		4.28e-02	
	128	3.85e-03	1.64	7.84e-03	1.81	2.40e-02	2.11
	192	1.80e-03	1.83	3.53e-03	1.94	8.66e-03	2.32
L^∞	256	1.02e-03	1.91	2.02e-03	1.96	5.50e-03	2.14
	384	4.60e-04	1.97	9.12e-04	1.95	2.44e-03	1.84
	512	2.59e-04	1.98	5.16e-04	1.97	1.51e-03	1.87
	768	1.16e-04	1.99	2.31e-04	1.98	1.13e-03	1.11
	1024	6.50e-05	2.00	1.30e-04	1.99	4.55e-04	1.74
	N	$\mathcal{E}_\rho$	σ_ρ	$\mathcal{E}_{\rho\|\boldsymbol{v}\|_2}$	$\sigma_{\rho\|\boldsymbol{v}\|_2}$	$\mathcal{E}_p$	σ_p
	64	9.41e-03		1.92e-02		8.06e-02	
	96	4.95e-03		9.94e-03		3.26e-02	
	128	2.97e-03	1.67	5.88e-03	1.71	1.76e-02	2.22
	192	1.38e-03	1.84	2.71e-03	1.88	6.88e-03	2.26
L^2	256	7.91e-04	1.91	1.54e-03	1.88	3.87e-03	2.20
	384	3.57e-04	1.95	6.94e-04	1.93	1.82e-03	1.92
	512	2.02e-04	1.97	3.92e-04	1.93	1.21e-03	1.69
	768	9.05e-05	1.98	1.75e-04	1.96	8.52e-04	1.10
	1024	5.11e-05	1.99	9.87e-05	1.96	3.62e-04	1.74
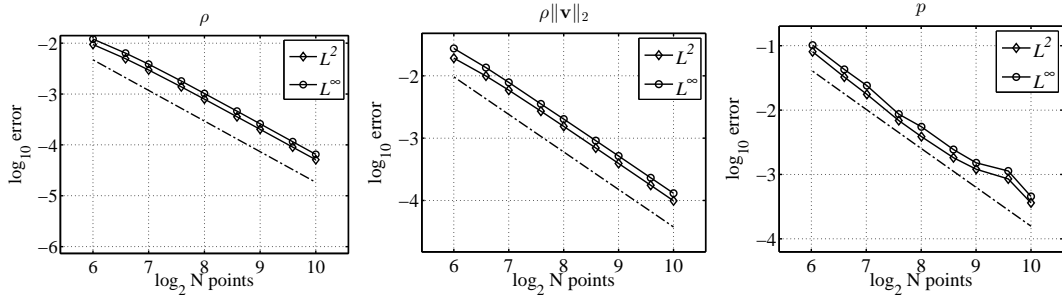
Figure 3.10: Density (left), momentum magnitude (middle) and pressure (right) convergence story for the smooth vortex case, fully compressible runs. Errors of computed solutions at $t = 1$ s on grids with N^2 cells with respect to initial data. The dashed-dotted line represents quadratic slope.

Convergence test with respect to a fine-grid solution

In order to investigate further the convergence in the vortex case, we perform yet another convergence study. Here the reference solution is taken to be the one at final time $t = 1$ s as computed on a fine grid (768×768 or 1024×1024 points). The fine-grid values are then restricted to coarser grids via standard interpolation to make them comparable with the results obtained with the coarser-grid simulations and to compute the corresponding errors. With this procedure, we are implicitly relying on the assumption that our scheme provides a physically meaningful solution. Therefore, as reference solution for this test we are not using the solution at a different time level, thereby avoiding comparison between data before and after the compressible adjustment occurring in the first stages of the simulation.

Considering Tables 3.4 and 3.5 and Figures 3.11 and 3.12, some coarse-grid effects as the one noticed in the previous convergence study (see above, Table 3.1) are still present, notably in the 64-to-128 rate values in Table 3.5. On the whole, however, the errors on the finer grids in this test appear to confirm the theoretical analysis and the validity of the strategy adopted in devising the compressible extension, with a preservation the second-order accuracy of the scheme.

Table 3.4: Variation of relative L^2 and L^∞ errors and convergence rates for the smooth vortex case as of Fig. 3.11. Errors computed as numerical solution at $t = 1$ s on grids with N^2 cells with respect to a fine-grid solution computed on 768^2 cells.

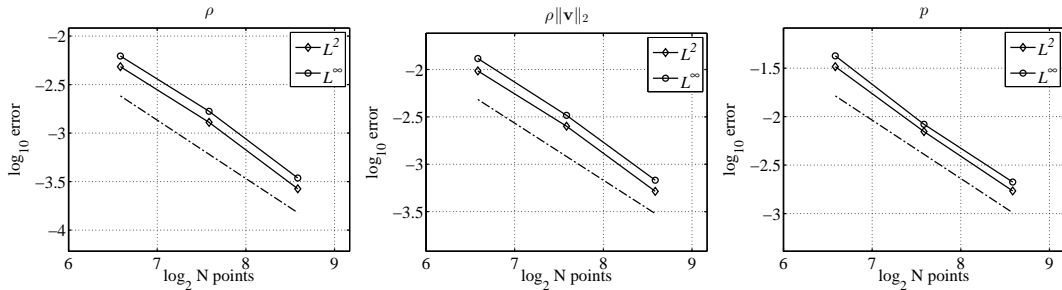|	N	$\mathcal{E}_\rho$	σ_ρ	$\mathcal{E}_{\rho\|v\|_2}$	$\sigma_{\rho\|v\|_2}$	$\mathcal{E}_p$	σ_p
	96	6.24e-03		1.31e-02		4.23e-02	
L^∞	192	1.68e-03	1.89	3.28e-03	1.99	8.33e-03	2.34
	384	3.44e-04	2.29	6.79e-04	2.27	2.12e-03	1.98
	N	$\mathcal{E}_\rho$	σ_ρ	$\mathcal{E}_{\rho\|v\|_2}$	$\sigma_{\rho\|v\|_2}$	$\mathcal{E}_p$	σ_p
	96	4.84e-03		9.66e-03		3.27e-02	
L^2	192	1.29e-03	1.91	2.52e-03	1.94	7.00e-03	2.22
	384	2.67e-04	2.27	5.18e-04	2.28	1.71e-03	2.03

Figure 3.11: Density (left), momentum magnitude (middle) and pressure (right) convergence story for the smooth vortex case. Errors of computed solutions at $t = 1$ s on grids with N^2 cells with respect to a fine-grid solution computed on 768^2 cells. The dashed-dotted line represents quadratic slope.

Table 3.5: Variation of relative L^2 and L^∞ errors and convergence rates for the smooth vortex case as of Fig. 3.12. Errors computed as numerical solution at $t = 1$ s on grids with N^2 cells with respect to a fine-grid solution computed on 1024^2 cells.

	N	$\mathcal{E}_\rho$	σ_ρ	$\mathcal{E}_{\rho\|v\|_2}$	$\sigma_{\rho\|v\|_2}$	$\mathcal{E}_p$	σ_p
	64	1.19e-02		2.64e-02		1.03e-01	
L^∞	128	3.78e-03	1.65	7.61e-03	1.79	2.38e-02	2.11
	256	9.59e-04	1.98	1.88e-03	2.02	5.11e-03	2.22
	512	1.94e-04	2.30	3.85e-04	2.29	1.13e-03	2.18
	N	$\mathcal{E}_\rho$	σ_ρ	$\mathcal{E}_{\rho\|v\|_2}$	$\sigma_{\rho\|v\|_2}$	$\mathcal{E}_p$	σ_p
	64	9.26e-03		1.87e-02		8.22e-02	
L^2	128	2.91e-03	1.67	5.73e-03	1.71	1.76e-02	2.23
	256	7.40e-04	1.97	1.44e-03	1.99	3.57e-03	2.30
	512	1.51e-04	2.29	2.93e-04	2.30	8.50e-04	2.07
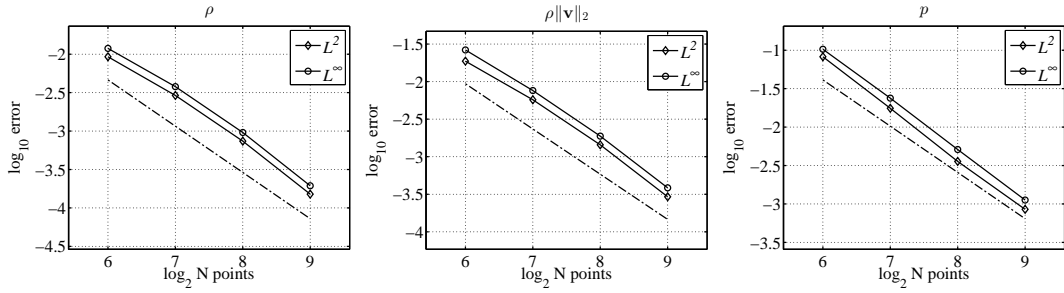
Figure 3.12: Density (left), momentum magnitude (middle) and pressure (right) convergence story for the smooth vortex case. Errors of computed solutions at $t = 1$ s on grids with N^2 cells with respect to a fine-grid solution computed on 1024^2 cells. The dashed-dotted line represents quadratic slope.

3.2.3 Weakly nonlinear acoustic wave

In this section, we present the results obtained in the simulation of a simple acoustic wave with the fully compressible scheme. The aim of this test is to show that our semi-implicit method is able to handle acoustic perturbations, which characterize the fully compressible system. In an acoustic wave, the restoring mechanism is given by pressure adjustments following compressive or expansive density perturbations. As noted, anelastic and pseudo–incompressible models suppress acoustic waves by explicitly neglecting this mechanism and eliminating the pressure dependence on density to different extents, as discussed in sections 1.1 and 2.3 above.

Following [95] and [121], we derive the initial data for a simple one-dimensional acoustic wave via characteristic theory. The eigenvalues of the Jacobian of the flux function relative to system (2.12a)-(2.12c) in homogeneous form and one space dimension correspond to the speeds, i.e. slopes, of three families of characteristics [39]. One finds the eigenvalues, for a flow velocity u:

$$\lambda_{1,3} = u \mp c, \ \lambda_2 = u. \tag{3.67}$$

The family of characteristics corresponding to λ_1 (respectively λ_3) represents leftward (resp. rightward)

travelling acoustic waves with speed c relative to the flow. We focus on the rightward-travelling wave. The function (Riemann invariant)

$$R^- = u - \frac{2c}{\gamma - 1} = K \in \mathbb{R} \tag{3.68}$$

is constant along the 3-characteristics (corresponding to $\lambda_3 = u + c$). In the one-dimensional domain $[0, L]$, we impose the following L-periodic horizontal perturbation of the speed of sound:

$$c = c_{\text{ref}} + \tilde{c} \sin \frac{2\pi x}{L} \tag{3.69}$$

where, for isentropic flows, $c_{\text{ref}} = \sqrt{\gamma p_{\text{ref}} / \rho_{\text{ref}}}$. The sound speed and the other derived quantities are taken constant in the vertical and the flow is one-dimensional.

The constant K in (3.68) is chosen in order to have zero background velocity:

$$0 = K + \frac{2c_{\text{ref}}}{\gamma - 1} \quad \implies \quad K = -\frac{2c_{\text{ref}}}{\gamma - 1}. \tag{3.70}$$

Using this expression and (3.68), we derive the initial velocity distribution:

$$u = \frac{2}{\gamma - 1} \tilde{c} \sin \frac{2\pi x}{L}. \tag{3.71}$$

We also assume a smooth-flow regime, so that the entropy and the potential temperature Θ may be taken as constant. Using the definition of potential temperature and the ideal gas equation of state we have:

$$p = \rho R T = \rho R \Theta \left(\frac{p}{p_{\text{ref}}} \right)^{\frac{\gamma - 1}{\gamma}} \tag{3.72}$$

where p_{ref} is a reference value for the pressure. Therefore we have, nondimensionalizing:

$$\rho_{\text{ref}} R \Theta_{\text{ref}} \rho' \Theta' = p_{\text{ref}} \left(\frac{p}{p_{\text{ref}}} \right)^{\frac{1}{\gamma}} \quad \implies \quad \frac{P}{P_{\text{ref}}} = P' = \rho' \Theta' \tag{3.73}$$

where the primes denote nondimensional quantities, and P has the definition (2.10). Note that in the last expression we recover the nondimensional definition of the energy variable $P = \rho \Theta$. As for the pressure and density, we derive their values from the speed of sound distribution as follows:

$$c = \sqrt{\frac{\gamma p}{\rho}} \quad \implies \quad c' c_{\text{ref}} = \sqrt{\frac{\gamma p_{\text{ref}}}{\rho_{\text{ref}}}} \sqrt{\frac{p'}{\rho'}} = (\rho')^{\frac{\gamma - 1}{2}} \tag{3.74}$$

where c' is the nondimensional speed of sound computed with (3.69), that is:

$$c' = 1 + \frac{\tilde{c}}{c_{\text{ref}}} \sin \frac{2\pi x}{L}. \tag{3.75}$$

With c' at hand, ρ' and p' can be computed via:

$$\rho' = (c')^{\frac{2}{\gamma-1}}, \tag{3.76}$$

$$p' = (c')^{\frac{2\gamma}{\gamma-1}}. \tag{3.77}$$

The last two relations, multiplied with the reference quantities ρ_{ref} and p_{ref}, yield an expression of all the quantities needed to initialize the rightward-travelling acoustic wave:

$$u = \frac{2}{\gamma-1}\tilde{c}\sin\left(\frac{2\pi}{L}x\right) \tag{3.78}$$

$$\rho = \rho_{\text{ref}}\left[1 + \frac{\tilde{c}}{c_{\text{ref}}}\sin\left(\frac{2\pi}{L}x\right)\right]^{\frac{2}{\gamma-1}} \tag{3.79}$$

$$p = p_{\text{ref}}\left[1 + \frac{\tilde{c}}{c_{\text{ref}}}\sin\left(\frac{2\pi}{L}x\right)\right]^{\frac{2\gamma}{\gamma-1}} \tag{3.80}$$

$$P = \rho_{\text{ref}}T_{\text{ref}}\left(\frac{p}{p_{\text{ref}}}\right)^{1/\gamma}. \tag{3.81}$$

We consider the reference values:

$$\rho_{\text{ref}} = 1\,\text{kg}\,\text{dm}^{-3},\ p_{\text{ref}} = 101325\,\text{Pa},\ T_{\text{ref}} = 353.048780488\,\text{K}. \tag{3.82}$$

As for $\tilde{c}$, setting for instance $\tilde{c} = 0.01 c_{\text{ref}}$ corresponds to having initially Ma ≈ 0.1. To facilitate the assessment of our scheme's performance, we will compare our results with the results obtained on the case of a weakly nonlinear gravity wave with the low-Froude numerical scheme for the shallow water equations described in [121]. In their dimensionless formulation, $c = \sqrt{h}/Fr$ denotes the gravity wave speed, where h denotes the fluid depth and Fr the Froude number. As a consequence and following [121] we have:

$$h = c^2 Fr^2 = \left(\frac{1}{Fr} + c_{\text{pert}}\right)^2 Fr^2 = (1 + Fr c_{\text{pert}})^2. \tag{3.83}$$

Introducing then the perturbation as of (3.75) we have:

$$\frac{Fr}{2}\sin\frac{2\pi}{L}x \overset{!}{=} \frac{\tilde{c}}{c_{\text{ref}}}\sin\frac{2\pi}{L}x. \tag{3.84}$$

Therefore, choosing:

$$\tilde{c} = c_{\text{ref}}\frac{Fr}{2} \tag{3.85}$$

and $\gamma = 2$ in the fully compressible system we obtain initial conditions equivalent to the weakly nonlinear gravity wave test in [121], see also [76].

As in [121], we will consider two perturbations:

$$\tilde{c} = \begin{cases} 0.05\,c_{\text{ref}} & Fr = 0.1 \\ 0.01\,c_{\text{ref}} & Fr = 0.02 \end{cases}. \tag{3.86}$$

For the density, this corresponds to a perturbation amplitude of $0.1\,\mathrm{kg\,dm^{-3}}$ in the first case (Figure 3.13 left), $0.02\,\mathrm{kg\,dm^{-3}}$ in the second case (Figure 3.14 left). Right panels in Figures 3.13 and 3.14 show initial horizontal momentum. Moreover, boundary conditions are periodic in both cases.
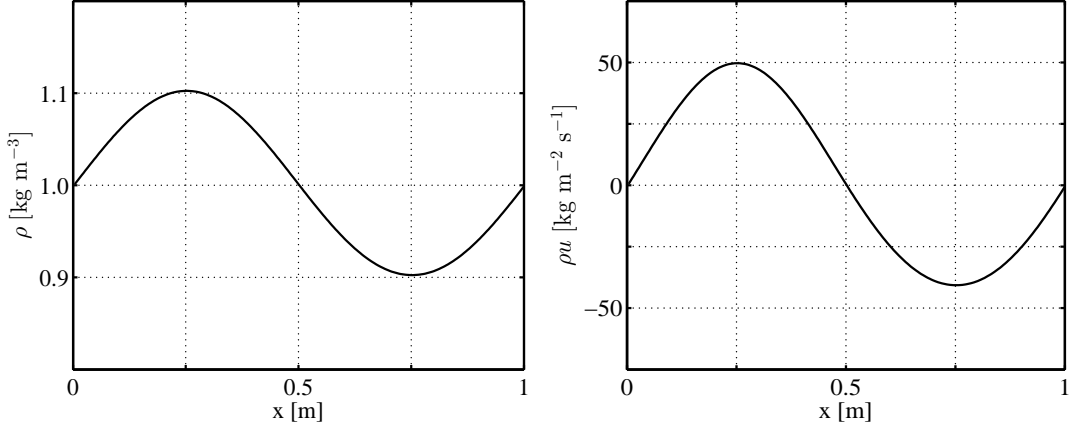

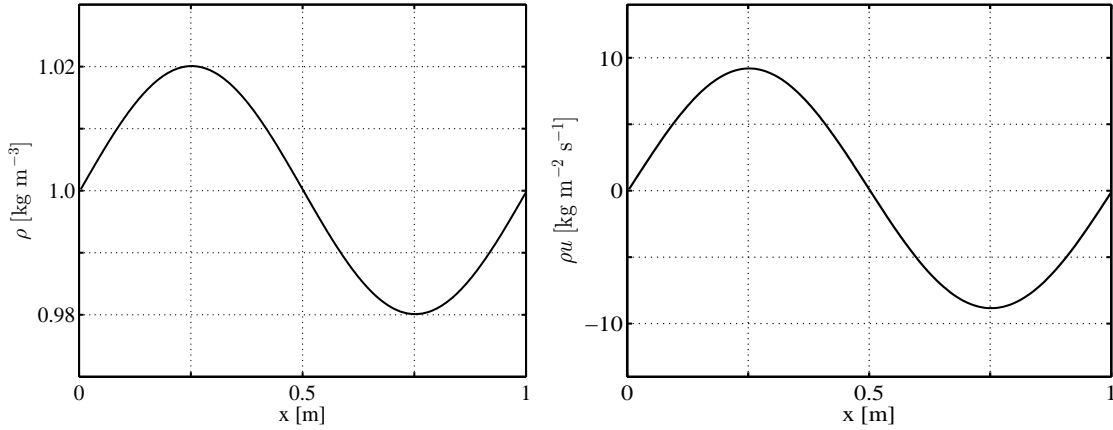**Figure 3.13:** Initial density (left) and horizontal momentum (right) for the simple acoustic wave in the case $\tilde{c} = 0.05c_{\mathrm{ref}}$.

Figure 3.14: Initial density (left) and horizontal momentum (right) for the simple acoustic wave in the case $\tilde{c} = 0.01c_{\mathrm{ref}}$.

The goal is to verify that our compressible scheme correctly reproduces the speed of the weakly nonlinear acoustic wave. First we consider the case with $Fr = 0.1$. We compare our simulations to [121] nondimensionalizing quantities as appropriate. It is worth remarking that, despite the equivalence of compressible equations and shallow water equations for $\gamma = 2$ and although the present numerical method and the method in [121] are built on the same premises (i.e. a projection-like numerical framework), some differences between the two methods are indeed present. For instance, [121] is based an exact projection technique whereby not only the variables but also their gradients are adjusted in the second correction step. Yet another difference is given by the pressure-energy binding (3.39), a distinctive feature of our scheme.

The final time $t = 0.00267282$ s is considered for a simulation with 256 horizontal cells and CFL $= 0.77$ as in [121]. At this time, the wave has already completed one round of the domain. Results are in the top panels of Figure 3.15. Solid lines denote the results with the present scheme, dashed lines results with the scheme of [121]. Compressible behaviour is visible as the wave steepens up as shown by the exact solution depicted in black as in [121]. The computed solution of the present scheme exhibits numerical dispersion leading to a phase error. The phase error is lower in the present scheme than it is with the scheme [121]. Furthermore, off-centring the second correction equation with $\theta = 0.7$ in (3.36) entails a more diffused and thus lower-amplitude result. The effect of off-centring appears smaller in the present scheme than in [121]. At the later time $t = 0.00668205$ s the nonlinear behaviour becomes even more visible, see bottom panels in Figure 3.15. At this time, the wave has completed three rounds of the domain and a shock is visible in the exact solution. The numerical scheme exhibits a dispersion error and smears out the discontinuity. The off-centred version introduced further numerical diffusion. Unlike the scheme of [121] our trapezoidal scheme is able to simulate the wave behaviour until this time. The off-centred version in our case displays less numerical diffusion than the reference scheme. This test case shows that the present scheme is able to give a fair picture of the wave dynamics including the wave steepening.
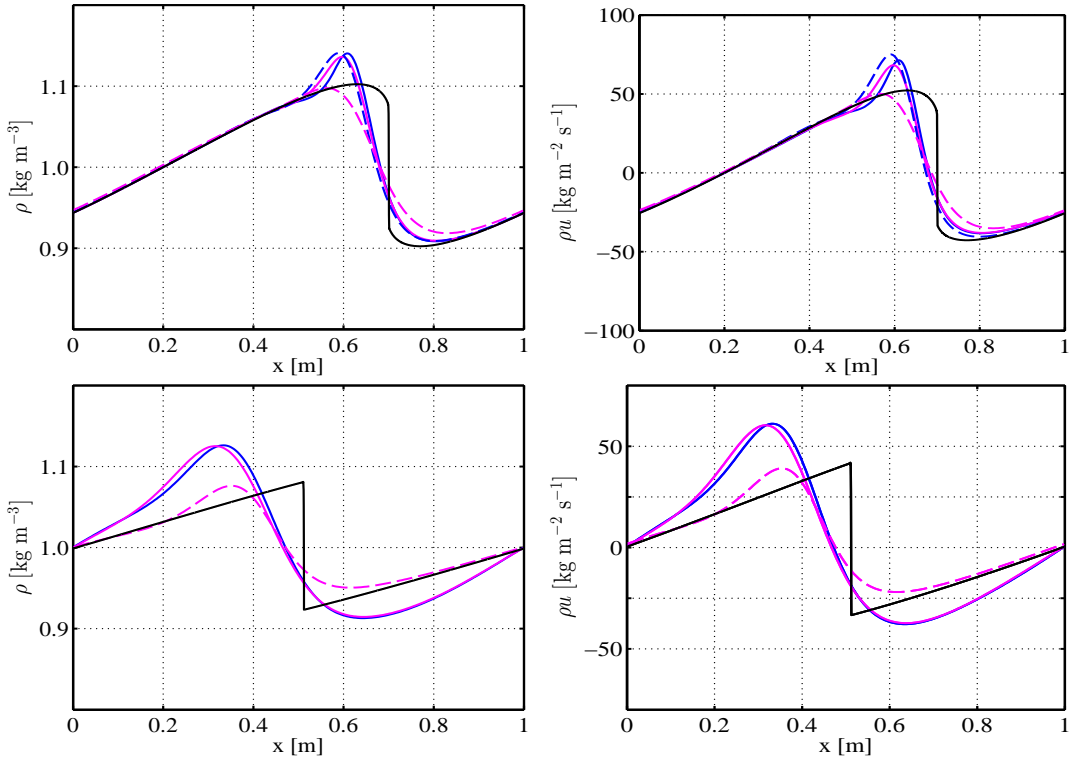

Figure 3.15: Computed density (left) and horizontal momentum (right) for the simple acoustic wave in the case $\tilde{c} = 0.05c_{\mathrm{ref}}$ at time $t = 0.00267282$ (top row) and $t = 0.00668205$ (bottom row) with CFL=0.77. Blue: trapezoidal scheme in the second projection; magenta: off-centred scheme in the second projection, $\theta = 0.7$. The black solid line denotes the exact solution as in [121].

Next, we turn to the analysis of the lower-amplitude wave with Fr $= 0.02$. We consider again results at final time $t = 0.00267282$ s. At this time, the wave has already travelled once across the domain. For this case we consider a reduced CFL $= 0.5$ with a view to the convergence study. Figure 3.16 displays the results with our scheme. Nonlinear effects are reduced with respect to the previous case. The wave dynamics is reproduced fairly well. Dispersion and diffusion effects can be especially noticed in the trough on the right. In general, both in the small and in the large amplitude case our scheme faithfully simulates the dynamics of the simple acoustic wave. We remark that simulation of acoustics and shocks is not the domain of application in which we will be chiefly interested; a number of numerical schemes better suited for the purposes of acoustic simulation is already present in the literature, see, e.g., [72] for an overview. Indeed, our scheme focuses on low-Mach number dynamics and is not meant to stand comparison with shock-capturing methods for transonic and supersonic flows.
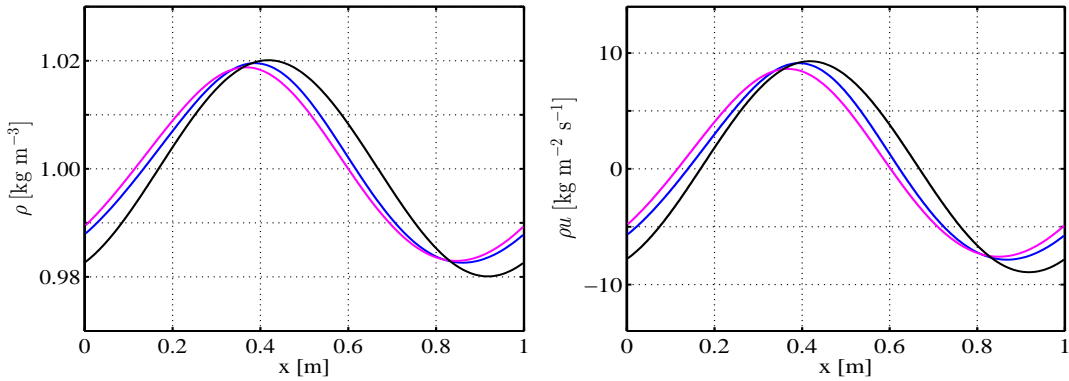

Figure 3.16: Computed density (left) and horizontal momentum (right) for the simple acoustic wave in the case $\tilde{c} = 0.01 c_{\text{ref}}$ at time $t = 0.00267282$ at CFL=0.5. Colours as in Figure 3.15.

Finally, we analyze the convergence behaviour of our scheme for the low-amplitude case (Table 3.6 and Figure 3.17). A fine-grid solution computed over 8192 cells is taken as the reference solution. Relative errors are computed on grids with 256, 512, 1024, 2048 and 4096 points with respect to the fine grid one. Here, for simplicity we considered a final time of $t = 0.001$ s, CFL $= 0.5$ and a trapezoidal approach. This corresponds to 148 time steps for the fine grid solution. The errors display the expected second-order rate of convergence.

Having validated our scheme in test cases without the influence of gravity, in the following chapter we turn our attention to the discretization of the gravity source term.

Table 3.6: Variation of relative L^2 and L^∞ errors and convergence rates for the acoustic wave case. Errors computed as numerical solution at $t = 0.001$ s on grids with N cells with respect to a fine-grid solution computed on 8192 cells in the horizontal direction.

|	N	$\mathcal{E}_\rho$	σ_ρ	$\mathcal{E}_{\rho|u|}$	$\sigma_{\rho|u|}$	$\mathcal{E}_p$	σ_p
	256	3.65e-03		2.27e-01		1.89e-01	
	512	1.16e-03	1.66	6.97e-02	1.70	5.85e-02	1.69
L^∞	1024	3.53e-04	1.71	1.99e-02	1.81	1.78e-02	1.72
	2048	1.01e-04	1.81	5.41e-03	1.88	5.07e-03	1.81
	4096	2.34e-05	2.10	1.25e-03	2.11	1.18e-03	2.10
	N	$\mathcal{E}_\rho$	σ_ρ	$\mathcal{E}_{\rho|u|}$	$\sigma_{\rho|u|}$	$\mathcal{E}_p$	σ_p
	256	2.25e-03		2.07e-01		1.65e-01	
	512	6.93e-04	1.70	6.08e-02	1.77	4.94e-02	1.74
L^2	1024	2.10e-04	1.73	1.70e-02	1.84	1.49e-02	1.73
	2048	6.00e-05	1.81	4.65e-03	1.87	4.25e-03	1.81
	4096	1.42e-05	2.08	1.08e-03	2.10	1.00e-03	2.08
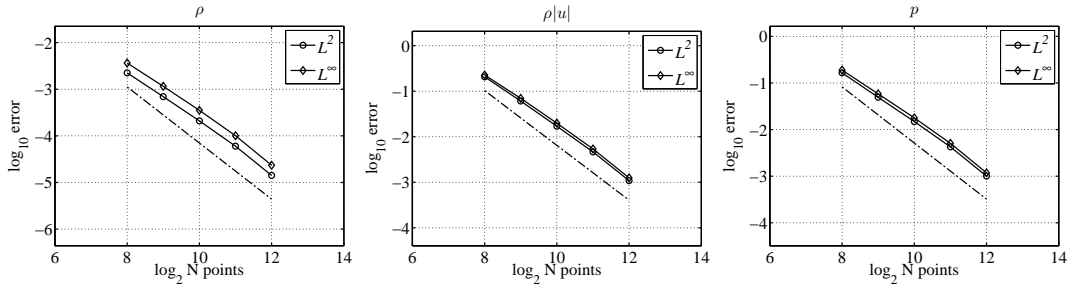
Figure 3.17: Density (left), momentum magnitude (middle) and pressure (right) convergence story for the acoustic wave case. Errors of computed solutions at $T = 0.001$ s on grids with N cells with N cells with respect to a fine-grid solution computed on 8192 cells in the horizontal direction.

4

Discretization of the buoyancy term

In this chapter we apply the fully compressible numerical framework described in Chapter 3 to gravity-driven flows. To this end, we describe the way in which the gravity source term is handled by the semi-implicit compressible scheme. First, we give a theoretical account of the well-balancing problem. Second, we list the modifications that we introduced in the numerical scheme in order to preserve the hydrostatic balance throughout. Third, we consider an atmosphere at rest and three test cases with thermal perturbations in order to assess the performance of the scheme in a homentropic and thermally stratified setting.

4.1 The well balancing problem

In the envisaged atmospheric applications of our scheme, flow patterns arise as perturbations around balanced states. If we focus our attention on the vertical direction, the dominant steady state is of hydrostatic balance. In absence of motion, the vertical component of the momentum equation (2.12b) takes the form

$$\frac{\partial p}{\partial z} = -\rho g. \tag{4.1}$$

In this configuration, the vertical pressure gradient offsets the gravitational force.

The finite volume method we use in our semi-implicit fully compressible scheme relies on a piecewise constant approximation of the physical variables. As such, an application of the scheme to evolve an initially motionless atmosphere in hydrostatic balance will preserve (4.1) at the discrete level up to the scheme's truncation error, in our case $O\big((\Delta x)^2\big)$. In particular, spurious vertical velocities will be introduced into the simulation. While the effect of these errors is hardly noticed in short-time, fine-grid runs on relatively large perturbations, these velocities are nonetheless unphysical and their accumulation unacceptably jeopardises the applicability of the scheme over the time scales typical of numerical weather prediction and climate simulations.

Numerical methods that preserve balanced states — and (4.1) in particular — up to machine precision ε, i.e., up to a $O(\varepsilon)$ error, are known in the literature as well-balanced schemes [19, 47]. As noted, one solution to sidestep the problem is to cast the physical model in terms of perturbations around a chosen hydrostatically

balanced background state. The resulting numerical models are well-balanced by construction [19, eq. (4)] and thus a widespread choice in the atmospheric modelling community, cfr., e.g. [93, 104, 119, 133]. While such an approach leads to considerable ease of implementation with respect to a full-variables-based approach as the one employed in the present study, it also relies on the choice of a reference state.

Here, we choose to work with full variables and endow our scheme with the well-balancing framework of [19], tackling the issue via local hydrostatic reconstructions, thereby dispensing with the degree of freedom of a global reference state. In the following, we first discuss the discretization of the source term in the predictor. Then, we present the parts of our implementation tuned to take into account the hydrostatic balance at the discrete level. We also refer to the recent analysis in [57] which employs techniques similar to the ones described below.

4.2 Neutrally and stably-stratified atmospheres

The well-balancing approach of [19] is implemented in the semi-implicit compressible discrete model. In the framework of a model written in non-perturbational form with a node-centred pressure, adjustments are required in the numerical scheme so as to maintain it hydrostatically balanced.

For later reference, we introduce the background atmospheric settings that we will consider in the remainder of the chapter. A homentropic atmosphere, i.e. with constant background potential temperature Θ, is obtained with the following choice of the variables (see [19]):

$$p(z) = p_{\text{ref}} \left(1 - \Gamma \frac{g\rho_{\text{ref}}}{p_{\text{ref}}} z \right)^{1/\Gamma}, \qquad \rho(z) = \rho_{\text{ref}} \left(\frac{p(z)}{p_{\text{ref}}} \right)^{\frac{1}{\gamma}}, \qquad \rho_{\text{ref}} = \frac{p_{\text{ref}}}{RT_{\text{ref}}}, \tag{4.2}$$

where $\Gamma = (\gamma - 1)/\gamma$.

A thermally stratified atmosphere with a height-varying potential temperature Θ such that $\partial\Theta/\partial z > 0$, is obtained considering as in, e.g., [93, 103]:

$$\Theta(z) = T_{\text{ref}} \exp\left(\frac{N^2}{g} z \right), \tag{4.3}$$

where N denotes the buoyancy frequency. For tropospheric simulations the reference value $N = 0.01 \text{ s}^{-1}$ is usually considered in the literature. The other variables are set as follows:

$$p(z) = p_{\text{ref}} \left\{ 1 - \frac{g}{N^2} \Gamma \frac{g\rho_{\text{ref}}}{p_{\text{ref}}} \left[1 - \exp\left(-\frac{N^2 z}{g} \right) \right] \right\}^{1/\Gamma}, \tag{4.4}$$

$$\rho(z) = \rho_{\text{ref}} \left(\frac{p(z)}{p_{\text{ref}}} \right)^{\frac{1}{\gamma}} \exp\left(-\frac{N^2 z}{g} \right), \qquad \rho_{\text{ref}} = \frac{p_{\text{ref}}}{RT_{\text{ref}}}. \tag{4.5}$$

Both in the homentropic and in the thermally stratified case the background analytical distributions of pressure and density are constructed in agreement with the hydrostatic balance Equation (4.1).

4.3 The discrete implementation of the gravity term

Let us reappraise the momentum equation in the predictor step (3.15b):

$$(\rho \boldsymbol{v})_C^{n+1,*} = (\rho \boldsymbol{v})_C^n - \Delta t \left(\widetilde{\nabla} \cdot \left(P \boldsymbol{v} \circ \boldsymbol{v} \Theta^{-1} + p^n \mathsf{I} \right) \right)_C^{n+\frac{1}{2},*} - \Delta t \, g \boldsymbol{k} \, (\rho)_C^{n+\frac{1}{2},*}. \tag{4.6}$$

First, in the case of gravity-driven flows, the time step restriction described in Section 3.1.1 and in particular expression (3.19) will feature the following buoyancy-dependent time step:

$$\Delta t_{\mathrm{B}} = \mathrm{CFL} \sqrt{\frac{\Delta x \, \max_\Omega \Theta'}{g \, \min_\Omega \Theta}}, \tag{4.7}$$

where $\max_\Omega \Theta' = \max_\Omega \Theta - \min_\Omega \Theta$ is the maximum potential temperature perturbation in Ω.

Next, we focus on the source term, i.e., the rightmost term in the vertical component of the Equation (4.6). A first possibility is to take the cell-centred value of the density for each cell as in (4.6), thus considering the discretization for the cell $C_{i,j} \equiv C$:

$$(\rho g)_C = \rho_{i,j} g \tag{4.8}$$

where $\rho_{i,j}$ is the value of the density at the centre of the cell $C_{i,j}$ and at the correct Runge-Kutta stage. The time superscripts and the horizontal index i will not be indicated in the rest of the section when not essential to the comprehension of the vertical discretization. The discretization (4.8) is arguably simple and attractive because of its low computational cost and ease of implementation. However, in numerical simulations carried out on the case of the rising warm air bubble, the strategy (4.8) was shown to entail instabilities already with values of CFL ≈ 0.05 in (4.7).

Therefore, other possibilities were explored. A three-cell approach can be considered

$$(\rho g)_C = \frac{1}{4} g \left(\rho_{j-1} + 2\rho_j + \rho_{j+1} \right) \tag{4.9}$$

this was beneficial in that it helped raising the threshold for stable runs up to CFL ≈ 0.1 in (4.7), but still far from the desired behaviour.

Considerable improvement was brought by considering linear distributions for the variable $1/\Theta$ in the vertical intervals $[z_{j-1}, z_j]$ and $[z_j, z_{j+1}]$ along the lines of what done in [61]. In particular, the Exner-pressure-based hydrostatic balance equation $c_p \Theta \partial \pi / \partial z = -g$, where $\pi = (p/p_{\mathrm{ref}})^\Gamma$ is employed to compute the integral of $1/\Theta$ over $[z_j, z_{j\pm 1/2}]$ as a function of $1/\Theta$ at z_j and $z_{j\pm 1}$, arriving to the following discretization:

$$(\rho g)_C = \frac{1}{\Delta z} p_{\mathrm{ref}} \left\{ \left\{ \pi_j - \frac{1}{8} \frac{\Delta z g}{c_p} \left[\left(\frac{1}{\Theta} \right)_{j+1} + 3 \left(\frac{1}{\Theta} \right)_j \right] \right\}^{1/\Gamma} \right.$$
$$\left. - \left\{ \pi_j + \frac{1}{8} \frac{\Delta z g}{c_p} \left[\left(\frac{1}{\Theta} \right)_{j-1} + 3 \left(\frac{1}{\Theta} \right)_j \right] \right\}^{1/\Gamma} \right\}, \tag{4.10}$$

where we have used the definition of the Exner pressure. In practice, the values of $(1/\Theta)_j$ are computed as $(\rho/P)_j$.

In the rising bubble case, the choice (4.10) enabled stable simulations at CFL $= 0.99$ in (4.7). This has to do with the fact that expression (4.10) explicitly uses the variable $1/\Theta$ instead of ρ. In fact, $1/\Theta$ represents the advected density in the computation of fluxes in the predictor, see Section 3.1.1. Therefore, better results are obtained using expression (4.10) in that (4.10) mirrors the flux computation more closely than it is the case using expression (4.8). Moreover, this choice enables a better separation of the effects of the pressure and the potential temperature on the buoyancy.

An even more convenient solution using $1/\Theta$ is obtained without the three-cell stencil (W. O'Neill, personal communication and [16]) as follows

$$(\rho g)_C = g\boldsymbol{k} P^{n+\frac{1}{2},*} \left(\frac{1}{\Theta} \right)_j . \tag{4.11}$$

In (4.11), $(1/\Theta)_j$ is computed as $(\rho/P)_j$. Furthermore, the value of P is computed as $P^{n+\frac{1}{2},*} = P^n + \frac{1}{2}\delta p \left(\partial P/\partial p \right)$ to preserve second-order accuracy, where δp is the pressure increment computed in the correction step of the previous time loop. The derivative of P with respect to p is computed using the equation of state as done in (3.31).

By discretizing the gravity source term using (4.11) we obtained the same results as with (4.10). However, (4.11) does not need a three-cell stencil so it is of arguable computational advantage, also with a view to the well-balancing adjustments described below.

Expression (4.11) was used for the simulation of the gravity-driven flows in this chapter and in Chapter 5. A comparison of the results obtained with the first strategy (4.8) is presented in the rising bubble case in Section 4.5.2.

4.4 Well-balancing-driven modifications

4.4.1 Initialization

The first modification to the basic version of the code occurs at the initialization stage. In the gravity-free case, initial values of discrete variables — including the pressure — are set up at cell centres and nodal values of the pressure are obtained by linear interpolation from the adjacent cell values. In cases with a stratified background pressure, as noted, such an approach produces values that violate the hydrostatic balance.

Since the problem is inherently one-dimensional, we focus on the vertical coordinate for the moment. First, let the initial data for pressure $p(z)$ and density $\rho(z)$ be given in the form of a homentropic or stably stratified atmosphere as in expressions (4.2) or (4.4) above. Next:

- $p(z)$ is initialized at cell centres z_j, $j = 1, \ldots, \mathcal{N}_z$ and nodes $z_{j-1/2}$, $j = 1, \ldots, \mathcal{N}_z + 1$ according to its analytical expression (4.2) or (4.4);

- $\rho(z)$ is initialized at z_j using a discretized form of the hydrostatic balance (4.1), i.e.

$$\rho(z_j) = -\frac{1}{g \Delta z}[p(z_{j+1/2}) - p(z_{j-1/2})], \quad j = 1, \ldots, \mathcal{N}_z \tag{4.12}$$
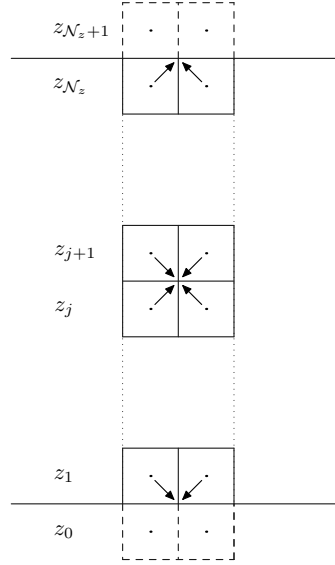
where Δz denotes the vertical grid spacing.

Figure 4.1: Well balancing framework. Arrows indicate the stencil for the cell-node interpolation as of expressions (4.19), (4.20), and (4.21). Also indicated are the first lower and upper ghost cells, see expressions (4.17) and (4.18).

4.4.2 Hydrostatic averaging of the pressure

The second modification to the scheme occurs in the computation of the predicted value of momentum, expression (3.15b). The value of the pressure at the centre of the cell face needed for the momentum flux computation in expression (3.15b) is computed as follows:

$$p(z_j) = \frac{1}{2}\left\{p(z_{j+1/2}) + p(z_{j-1/2}) - g\left[2f(z_j) - f(z_{j+1/2}) - f(z_{j-1/2})\right]\right\} \tag{4.13}$$

for $j = 1, \ldots, \mathcal{N}_z$, where:

$$f(z) = \int_0^z \rho(z')\mathrm{d}z' \tag{4.14}$$

and the square bracket in (4.13) represents a hydrostatic modification of the simple average. Note that the integral in (4.14) is computed analytically for each cell. Specifically, we have:

$$f(z) = \left(1 - \Gamma\frac{g\rho_{\mathrm{ref}}}{p_{\mathrm{ref}}}z\right)^{1/\Gamma} \tag{4.15}$$

for the homentropic distribution (4.2) and

$$f(z) = \left\{ \Gamma \frac{\rho_{\text{ref}}}{p_{\text{ref}}} \frac{g^2}{N^2} \left[\exp\left(-\frac{N^2}{g}z\right) - 1 \right] + 1 \right\}^{1/\Gamma} \tag{4.16}$$

for the stably stratified distribution (4.4).

4.4.3 Boundary conditions

The third well-balancing modification involves the so-called "solid wall" boundary conditions. As customary in finite differences and finite volume codes [72], in our scheme we implement fully reflecting boundaries using "ghost cells". The strategy involves attaching two dummy cells to the boundary in which the value of all the variables except for the normal velocity is mirrored from the two innermost cells, whereas the normal velocity value is taken with opposite sign.

We modify the process for the mirrored variables in that we retrieve the hydrostatic values of the variables in the ghost cells. For instance, for the pressure in the ghost cells adjacent to the lower boundary we have:

$$p(z_0) = p(z_1) + g \int_{z_0}^{z_1} \rho(z')dz'. \tag{4.17}$$

For the pressure in the ghost cells adjacent to the upper boundary, we have.

$$p(z_{\mathcal{N}_z+1}) = p(z_{\mathcal{N}_z}) - g \int_{z_{\mathcal{N}_z}}^{z_{\mathcal{N}_z+1}} \rho(z')dz'. \tag{4.18}$$

4.4.4 Hydrostatic interpolation and pressure-energy binding

The fourth modification involves the interpolation from nodes to cell centres or *vice versa*, which in the case without gravity is a standard linear interpolation. In the cases with gravity, the cell-to-node interpolation used in the pressure update (3.39) after the second correction step is implemented as follows (see also Figure 4.1 for corroboration):

- For the nodes on the lower boundary:

$$p(x_{i+1/2}, z_{1/2}) = 0.5(p_{NW} + p_{NE}), \quad \forall\, i = 1, \ldots, \mathcal{N}_x \tag{4.19}$$

  where p_{NW} and p_{NE} denote the pressure values obtained with analytical integration — expr. (4.14) — downwards from the hydrostatic pressure values in the adjacent upper left and upper right cell, respectively.

- For the nodes on the upper boundary:

$$p(x_{i+1/2}, z_{\mathcal{N}_z+1/2}) = 0.5(p_{SW} + p_{SE}), \quad \forall\, i = 1, \ldots, \mathcal{N}_x \tag{4.20}$$

where p_{SW} and p_{SE} denote the pressure values obtained with analytical integration upwards from the hydrostatic pressure values in the adjacent lower left and lower right cell, respectively.

- For the internal nodes:

$$p(x_{i+1/2}, z_{j+1/2}) = 0.25(p_{SW} + p_{SE} + p_{NW} + p_{NE}), \quad \forall\, i = 1, \ldots, \mathcal{N}_x,\ j = 1, \ldots, \mathcal{N}_z. \quad (4.21)$$

Finally, we remark that the fully compressible scheme appeared — at least operationally — more sensible to violations of hydrostatic balance as opposed to the pseudo-incompressible model. For the latter, as noted in Chapter 2, the pressure plays the role of a Lagrange multiplier that enforces the divergence constraint (2.21c) at each time loop. Therefore, the pseudo-incompressible scheme is able to default to discretely balanced values of the prognosed variables after the solution of the two Poisson equations in the correction step. By contrast, the fully compressible model incorporates the complete thermodynamics through the energy derivative term in (2.12c) and the energy-pressure binding driven by the equation of state in (3.39). This latter feature in particular entails the automatic transfer of any perturbation in one variable upon the others.

4.5 Numerical results

In this section we show the results obtained with our code in a number of gravity-driven flow simulations and compare them with references in the literature. First, we consider an atmosphere at rest test case, with the aim of verifying the well-balancing of the scheme, i.e. the absence of spurious vertical velocities by running the code for a large number of time steps. Then, we run our scheme on two thermal bubbles on the neutrally stratified setting (4.2) to examine the capabilities of the scheme in the simulation of buoyancy-driven dynamics. Finally, we consider the propagation of inertia-gravity waves in a horizontal channel initiated by a thermal perturbation on the stably stratified background (4.4).

4.5.1 Atmosphere at rest

As a test for the well-balancing properties of the numerical scheme, we consider a case of atmosphere at rest, that is, a homentropic or thermally stratified motionless state with no bottom topography. Running our scheme for a large number of time steps, we expect no spurious perturbations to be generated up to machine precision.

Let $\Omega = [-10, 10] \times [0, 10]$ km be a horizontally periodic domain with solid walls on top and bottom boundaries gridded with 160×80 cells, and let pressure and density be given by the homentropic distribution (4.2), with zero initial velocity and, in agreement with [19], $g = 10$ m s^2. The scheme is run until the final time $\mathcal{T} = 43200$ s (12 hours or 23544 time steps with $\Delta t_I = 1.9$ s). Figure 4.2 on the left displays the temporal evolution of the maximum norm of the vertical velocity in the domain. Generated perturbations are of the order of the machine precision times the grid points (see Table 4.1) as the atmosphere remains

virtually at rest up to errors consistent with double machine precision. Furthermore, no significant growth pattern is displayed.
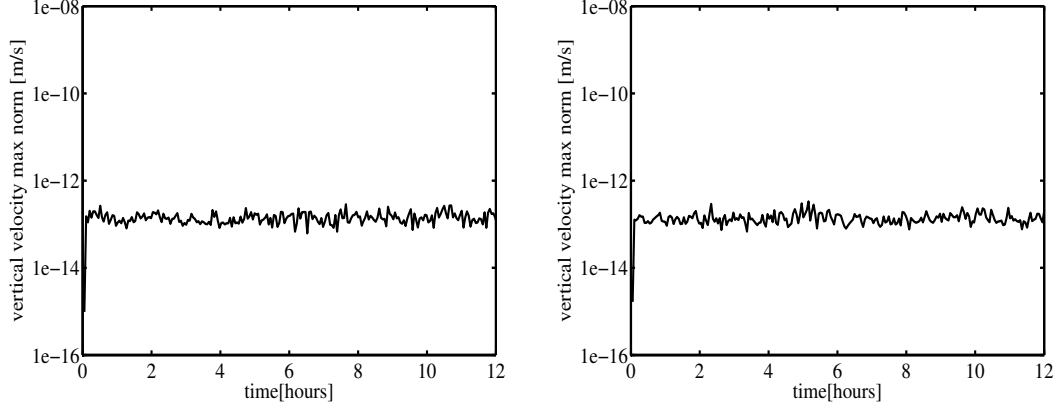

Figure 4.2: Maximum vertical velocity norm, homentropic (left) and thermally stratified (right) atmosphere at rest, final time $\mathcal{T} = 43200\,\text{s}$.

Next, we consider the stratified scenario (4.4) in the same geometric setting. As documented in the right panel of Figure 4.2, the maximum error in the vertical velocity remains of the order of the machine precision times the grid points (Table 4.1) throughout the whole simulation and shows no growth pattern. We remark that in both cases longer-time runs (not shown) have been performed that confirm the findings. The results corroborate the validity of our well-balancing strategy and are expecially promising with a view to future developments for large-scale, long-time test cases and in presence of bottom topography.

Table 4.1: Maximum vertical velocity for the homentropic (w_H) and stably stratified (w_S) atmosphere at rest simulations of Figure 4.2. The value of roundoff error times the total cell number is reported for comparison.

$\max\left(w_H\right)$	$\max\left(w_S\right)$	$\varepsilon \mathcal{N}_x \mathcal{N}_z$
3.52e-13 m s^{-1}	3.24e-13 m s^{-1}	2.84e-12

4.5.2 Rising thermal bubble

Next, we examine a convection test case in the domain $\Omega = (x,z) \in [-10, 10] \times [0, 10]\,\text{km}^2$. Specifically, we consider a warm thermal perturbation Θ' upon the homentropic setting (4.2) as in [61]:

$$\Theta'(x,z) = \begin{cases} \delta\Theta \cos^2(\frac{\pi}{2}r) & (r \leq 1) \\ 0 & \text{otherwise} \end{cases}, \qquad \begin{cases} \delta\Theta = 2\,\text{K} \\ r = 5\sqrt{(\frac{x}{L})^2 + (\frac{z}{L} - \frac{1}{5})^2} \\ L = 10\,\text{km} \end{cases} . \qquad (4.22)$$

In agreement with [61], ρ_{ref}, p_{ref}, g, and T_{ref} have the values $1\,\text{kg}\,\text{m}^{-3}$ $8.61\text{e}04\,\text{N}\,\text{m}^{-2}$, $10\,\text{m}\,\text{s}^{-2}$, and $300\,\text{K}$. The initial velocity is zero. Lateral boundary conditions are periodic, with solid walls on top and bottom boundaries. Figure 4.3 displays Θ'.
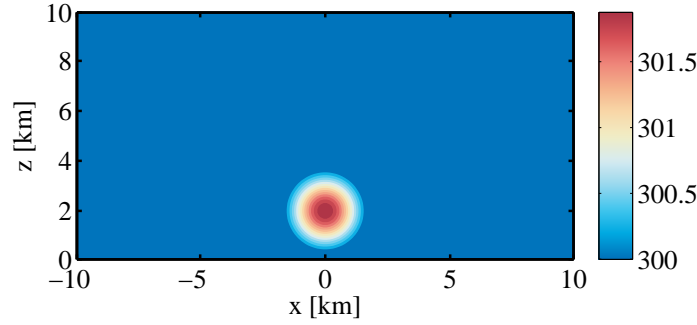

Figure 4.3: Rising thermal bubble initial potential temperature. Colour shading every 0.125 K starting at $\Theta = 300.25$ K.

We run the semi-implicit compressible scheme on a grid with $\Delta x = \Delta z = 125$ m, i.e. 160×80 cells, and CFL $= 0.5$. The trapezoidal approach is used in the second projection. In the first five steps a buoyancy-driven time step $\Delta t = \Delta t_{\text{B}} \approx 21.69$ s is used. Due to growing velocities, the advection-driven time step is then selected for the remainder of the simulation. Towards the end of the simulation, values of $\Delta t \approx 4.6$ s are attained (Figure 4.5).

Driven by buoyancy, the warm bubble rises and rolls up on the sides (Figure 4.4). The dynamics of the bubble is reproduced by the numerical scheme without oscillations. At the final time $\mathcal{T} = 1000$ s, the value of the thermal perturbation amplitude (Table 4.2) and the attained height are in agreement with the soundproof results in the reference [61, fig. 3 and 4], see also [65]. This is expected at the scales considered in this test case.

These results were corroborated by comparisons with the results produced by a pseudo-incompressible version of the code and a thermodynamically consistent modification [16], see also [66]. For further analysis on this test case using the blended code we refer to Section 5.3 below.

For reference, the total wallclock time for the simulation of Figure 4.5 was 71.113 s including preprocessing input, actual computation and output. 40% of the total wallclock time was taken up by the predictor step and 56% by the corrector step.

Table 4.2: Maximum and minimum potential temperature Θ_{max} and Θ_{min}, and corresponding maximum perturbation $\delta\Theta$ at final time $\mathcal{T} = 1000$ s for the fully compressible model as of Figure 4.4 for the dry rising bubble test case.

Θ_{max}	Θ_{min}	$\delta\Theta$
301.54 K	299.9 K	1.64 K

Furthermore, for the simulation of Figure 4.4, we report in Figure 4.6 an assessment of the energy balances,
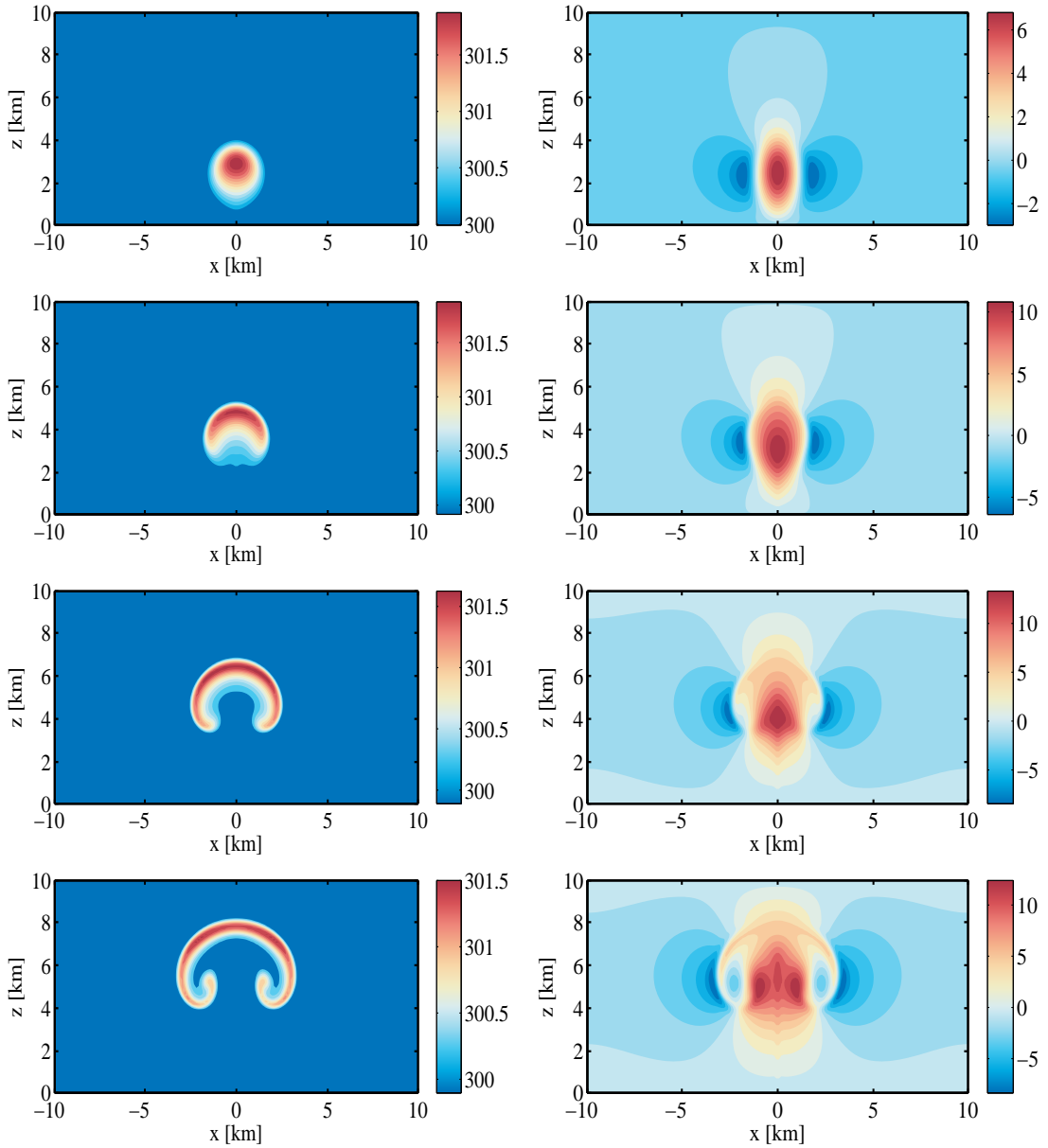
Figure 4.4: Rising thermal bubble results with the fully compressible scheme, large time steps. Top to bottom: computed potential temperature (left panels) and vertical velocity (right panels) at $t = 250, 500, 750, 1000$ s. Colour shading every 0.125 K starting at 300.25 K for the potential temperature. For the vertical velocity, 16 colour shades are represented in the intervals (top to bottom) $[-2.99, 7.41]$ m s^{-1}, $[-6.40, 11.89]$ m s^{-1}, $[-8.46, 14.66]$ m s^{-1}, $[-8.45, 13.69]$ m s^{-1}.
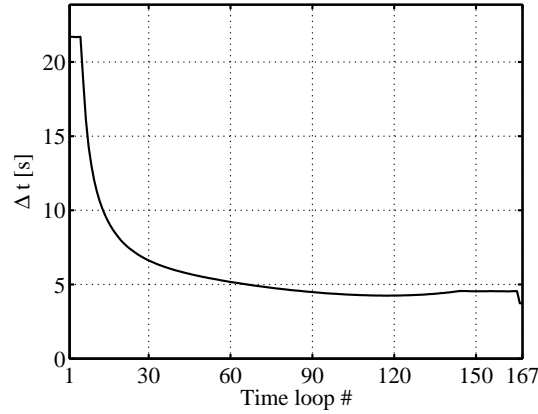
Figure 4.5: Time step size as a function of the time loop in the rising bubble run at CFL $= 0.5$ as of Figure 4.4.

see definitions (2.3). The volumetric integrals of the kinetic, potential, internal and total energy are computed to obtain the global value of the quantities over the domain. The top left panel reports the time series of the normalized change of global potential, internal and total energy values with respect to the global values at time $t = 0$. The top right panel reports the time series of the global kinetic energy value.

The potential energy decays as the bubble rises while the kinetic energy grows as velocities build up. The value of the total energy is analyzed in the lower panels, where a normalized value with respect to the maximum value of the kinetic energy during the run is also presented. Despite a growth pattern in the total energy plots, these scores appear satisfactory at this stage, also in view of the fact that, as noted, by design we do not expect our scheme to conserve more than total mass, horizontal momentum and P.

Convergence study, constant vs. variable time step

In order to assess the accuracy of our scheme, we perform a convergence study based on the computed potential temperature Θ at time $t = 250$ s. Errors are evaluated between computed solutions with $\Delta z = \Delta x = 500, 250, 125, 62.5$ m with respect to the computed solution with $\Delta z = \Delta x = 31.25$ m. The analysis is carried out both for the case of a variable time step run as in Figure 4.5 and for a run at constant time step $\Delta t = 2$ s. As documented in Figure 4.7 and Table 4.3, second-order convergence rate is observed with comparable values of the relative errors. The choice of an adaptive time step does not affect the accuracy.

Runs with simple discretization of gravity

For reference, we report the result with the simple discretization of the gravity source term considered in (4.8) (Figure 4.8 and Table 4.4. In terms of attained height and final amplitude of the thermal perturbation, results mathc the ones reported in Figure 4.4 and Table 4.4. However, note that the time step employed in the case with simple discretization of gravity is $\Delta t \approx 1.91$ s, or CFL $= 0.044$ in expression (3.19). Considering higher values of the time step with this discretization of the source term led to instabilities.
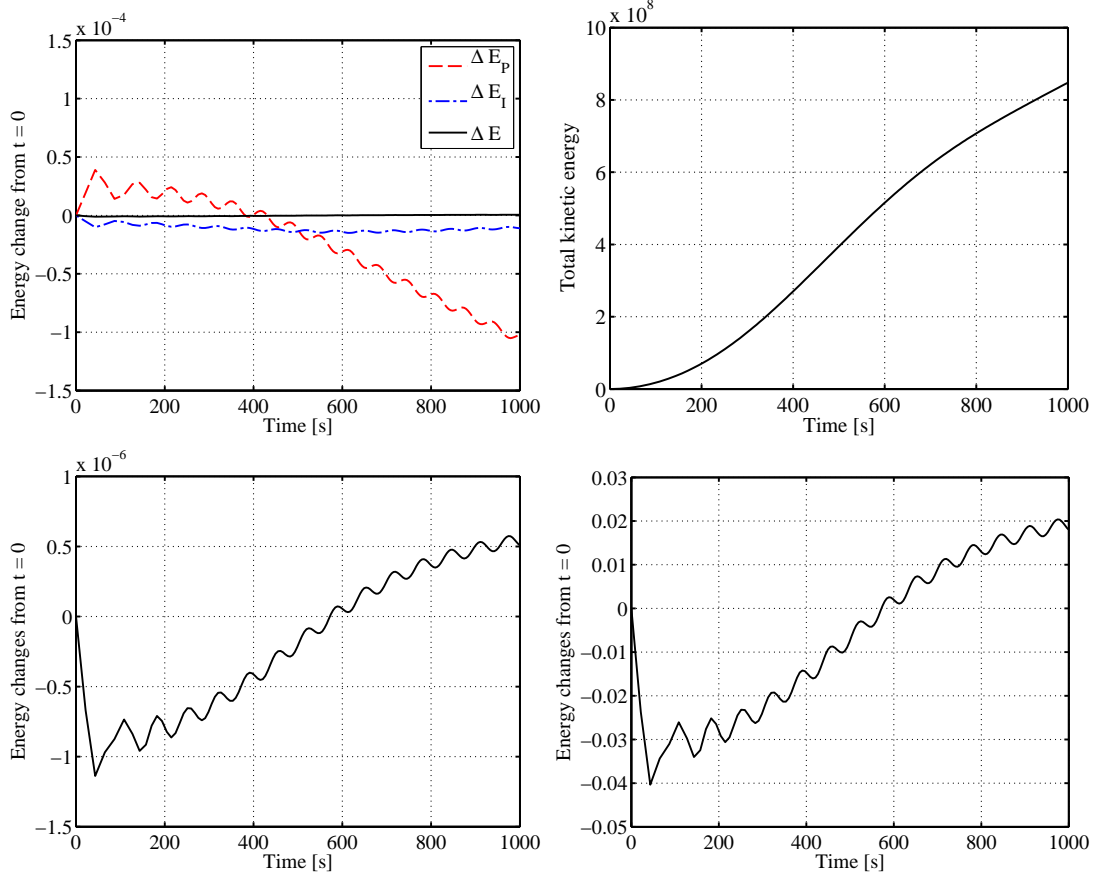
Figure 4.6: Energy time series for the rising bubble run of Figure 4.4. Top left: normalized relative change with respect to values at initial time of global potential energy (dashed red), internal energy (dashed-dotted blue), total energy (solid black). Top right: global kinetic energy value. Bottom left: magnified total energy plot as of top left panel. Bottom right: Same as bottom left, but normalized by the maximum global kinetic energy value in the run.
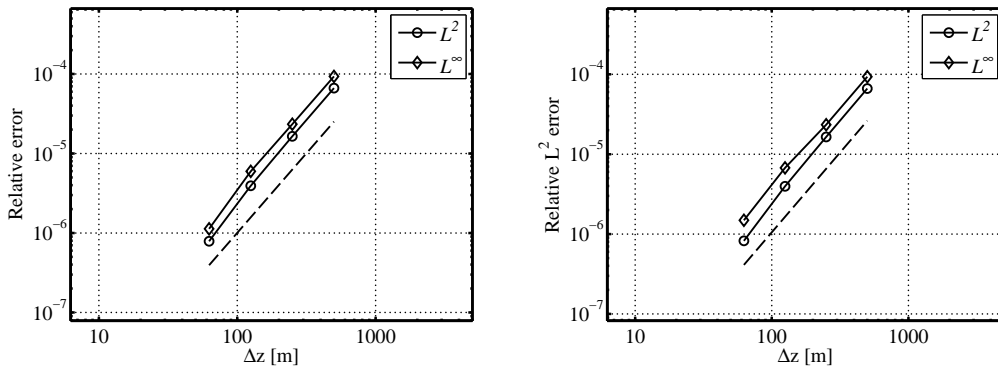

Figure 4.7: Convergence story for the computed potential temperature at time $t = 250$ s in the rising bubble test case. Relative errors and convergence rates on grids with $\Delta z = \Delta x = 500,\ 250,\ 125,\ 62.5$ m with respect to a fine-grid solution on a grid with $\Delta z = \Delta x = 31.25$ m. Left panel: constant Δt. Right panel: variable Δt at CFL=0.5 as in Figure 4.5.

Table 4.3: Relative errors $\mathcal{E}$ and convergence rates σ of computed solutions on grids with $\Delta z = \Delta x = 500, 250, 125, 62.5$ m with respect to the computed solution on a grid with $\Delta z = \Delta x = 31.25$ m, see Figure 4.7. Left table: constant Δt. Right table: variable Δt at CFL $= 0.5$.

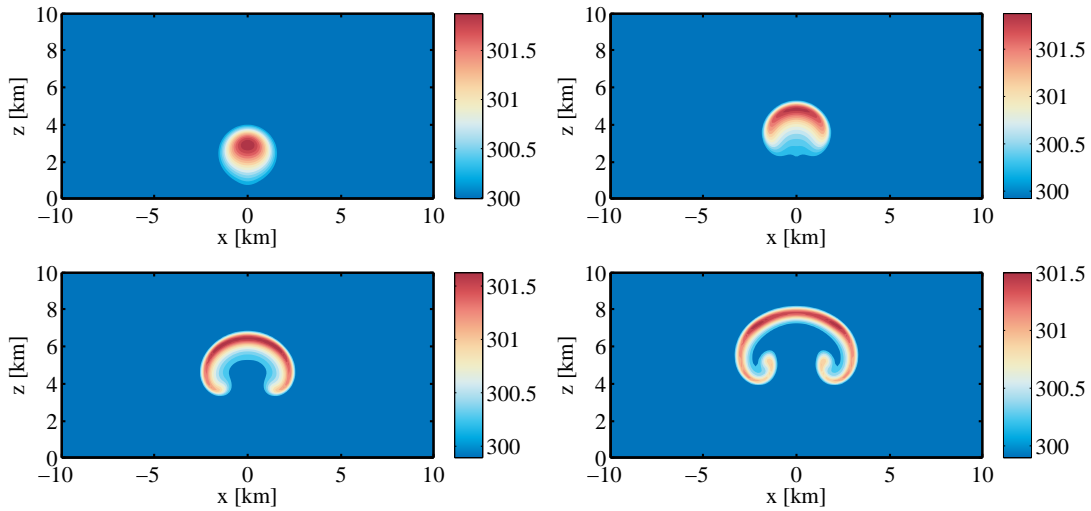| Δz [m]	L^2 $\mathcal{E}_\Theta$	σ_Θ	L^∞ $\mathcal{E}_\Theta$	σ_Θ	Δz [m]	L^2 $\mathcal{E}_\Theta$	σ_Θ	L^∞ $\mathcal{E}_\Theta$	σ_Θ
500	6.65e-05		9.35e-05		500	6.65e-05		9.35e-05	
250	1.65e-05	2.01	2.34e-05	2.00	250	1.64e-05	2.01	2.34e-05	2.00
125	3.93e-06	2.07	5.97e-06	1.97	125	3.96e-06	2.05	6.74e-06	1.79
62.5	7.87e-07	2.32	1.13e-06	2.40	62.5	8.22e-07	2.27	1.49e-06	2.18

Figure 4.8: Rising thermal bubble results in a run with the gravity discretization (4.8). Computed potential temperature at $t = 250$ s (upper left), $t = 500$ s (upper right), $t = 750$ s (lower left), $t = 1000$ s (lower right). Colour shading every 0.125 K starting at $\Theta = 300.25$ K. The time step is $\Delta t = 1.91$ s.

Table 4.4: Maximum and minimum potential temperature Θ_{max} and Θ_{min}, and corresponding maximum perturbation $\delta\Theta$ at final time $\mathcal{T} = 1000$ s as of Figure 4.8 for the dry rising bubble test case.

Θ_{max}	Θ_{min}	$\delta\Theta$
301.57 K	299.9 K	1.67 K

Moreover, in the context of small time step runs we observed a checkerboarding effect in the velocity both with discretization (4.11) and with discretization (4.8) for the source term. The effect is visible in the vertical velocity plot at $t = 500$ s in a simulation with $\Delta t = 1.9$ s (Figure 4.9). We remark that the effect is not present in runs at large time step as the ones seen in Figure 4.4.

Many options have been considered to sidestep the problem. Among them are considering the BDF2 discretization in the second correction, adopting the five-point stencil as in [100] for the nodal elliptic problem and modifying the computation of the fluxes of P in the predictor by taking values of P at the interface in agreement with the hydrostatic balance. None of these modifications altered the checkerboard pattern. The problem remains object of research, see the discussion in Chapter 7.
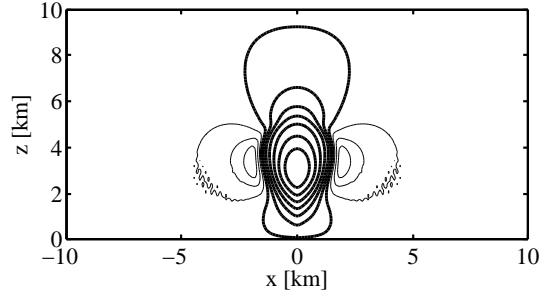
Figure 4.9: Rising thermal bubble results, computed vertical velocity at $t = 500$ s. 10 contours in the interval $[-6.38, 11.92]$ m s^{-1}. Thin lines denote negative contours. The time step used is $\Delta t = 1.9$ s

4.5.3 Density current

The next test [113] consists in a negative potential temperature perturbation in a $[-25.6, 25.6] \times [0, 6.4]$ km^2 neutrally stratified atmosphere (4.2),

$$T' = \begin{cases} 0.0 \text{ K} & \text{if } r > 1 \\ -15.0 \left[1.0 + \cos(\pi r)\right]/2 \text{ K} & \text{if } r < 1 \end{cases}, \tag{4.23}$$

where $r = \left\{ [(x - x_c)/x_r]^2 + [(z - z_c)/z_r]^2 \right\}^{0.5}$, $x_c = 0.0$ km, $x_r = 4.0$ km, $z_c = 3.0$ km, $z_r = 2.0$ km. From $\Theta = T(p/p_{\text{ref}})^{-\Gamma}$ we derive $\Theta_{\text{ref}} = T_{\text{ref}}$ and the potential temperature perturbation and density distribution,

$$\Theta'(x, z) = \frac{T'}{1 - \Gamma \frac{g \rho_{\text{ref}}}{p_{\text{ref}}} z}, \qquad \rho(z) = \rho_{\text{ref}} \left(\frac{p(z)}{p_{\text{ref}}} \right)^{\frac{1}{\gamma}} \frac{\Theta_{\text{ref}}}{\Theta_{\text{ref}} + \Theta'}. \tag{4.24}$$

In particular, we have $\max |\Theta'| = 16.63$ K. The boundary conditions are periodic on the left and right boundary, solid walls on the top and bottom boundary. Furthermore, we add an artificial diffusion term $\rho \mu \nabla^2 \boldsymbol{v}$ to the right hand side of the momentum equation ($\rho \mu \nabla^2 \Theta$ in the P equation), with $\mu = 75$ m^2 s^{-1} as in [113]. The initial velocity is set to zero, and the reference quantities are $T_{\text{ref}} = 300$ K, $p_{\text{ref}} = 10^5$ Pa, $\rho_{\text{ref}} = p_{\text{ref}}/(R T_{\text{ref}})$.

The semi-implicit fully compressible model is run with $\Delta x = 50$ m and CFL $= 0.5$. Thus, the time step is $\Delta t = \Delta t_{\text{B}} \approx 4.65$ s for the first three steps and then the advective time step is used. A BDF2 approach in the second projection is used, see Equation (3.49).

The negative buoyancy of the bubble drives it down, until it hits the bottom boundary and starts travelling in the horizontal direction with small-scale Kelvin-Helmholtz instabilities (Figure 4.10). Due to the symmetrical nature of the test-case, only the plots for the subdomain $[0, 19.2] \times [0, 4.8]$ km^2 are shown. The scheme resolves fairly well the flow patterns at the different scales and gives a good representation of the vortices. The computed final values of thermal perturbation and the front position (Table 4.5) are in line with results in the literature [2, 93, 113].

The total wallclock time for the simulation as in Figure 4.10 was 4896.72 s. 40% of the total wallclock time

was taken up by the predictor step, 57% by the corrector step.

As in the previous test, results with the fully compressible model are comparable to the ones obtained with pseudo-incompressible runs as expected at the spatial scales under consideration (see [16]).
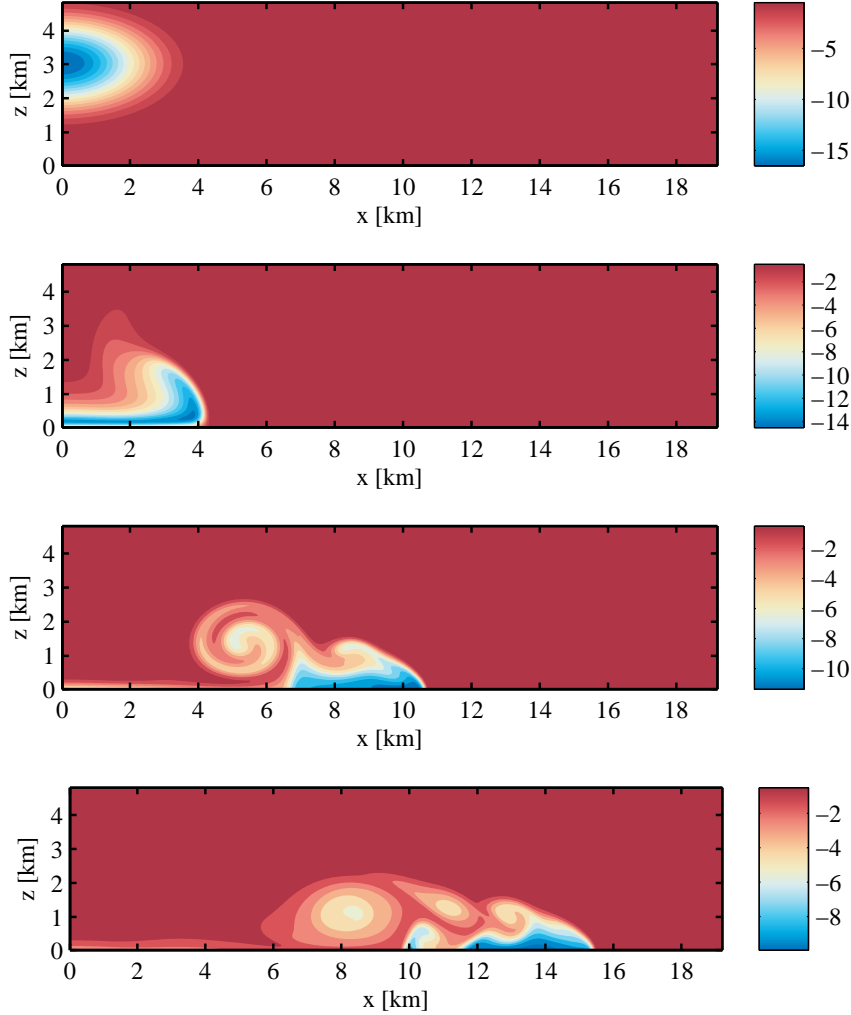

Figure 4.10: Potential temperature perturbation in the density current test case. Computed solution with $CFL = 0.5$ at resolution $\Delta x = \Delta z = 50$ m. Top to bottom: initial data, computed data at $t = 300$ s, 600 s, 900 s. Colour shading every 1 K starting at -16.5 K.

Table 4.5: Maximum and minimum potential temperature Θ_{max} and Θ_{min}, corresponding maximum perturbation Θ', and front position x_{max} at final time $\mathcal{T} = 900$ s for the density current test case, as of Figure 4.10. x_{max} is defined as the rightmost intersection of the 1 K contour with the bottom boundary

Θ_{max}	Θ_{min}	Θ'	x_{max}
300.17 K	290.03 K	10.14 K	15475.68 m

Convergence study

We present a convergence study based on the computed potential temperature distribution Θ at time $t = 100$ s. Errors are evaluated between computed solutions with grids at resolutions $\Delta z = \Delta x = 800, 400, 200, 100$ m and the computed solution with $\Delta z = \Delta x = 50$ m as reference. Quadratic convergence rate is found both in the trapezoidal and in the BDF2 case (Figure 4.11 and Table 4.6).
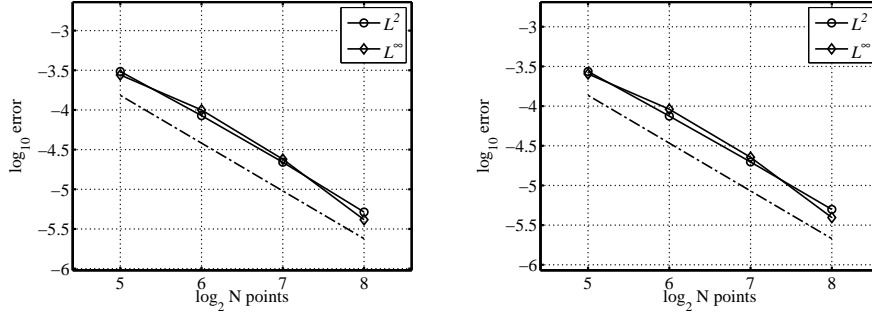

Figure 4.11: Convergence story for computed potential temperature Θ at time $t = 100$ s on $[0, 25.6] \times [0, 6.4]$ km^2. Relative errors computed with respect to a fine-grid solution with $\Delta x = 50$ m (512×128 cells). Left panel: trapezoidal method in the second projection. Right panel: BDF2 method in the second projection.

Table 4.6: Variation of relative L^2 and L^∞ errors and convergence rates for the density current case as of Fig. 4.11. Errors computed as numerical solution at $t = 100$ s on grids with $\mathcal{N}_x \times (\mathcal{N}_x/4)$ cells with respect to a fine-grid solution computed on 512×128 cells. Left table: trapezoidal method in the second projection. Right table: BDF2 method in the second projection.

$\mathcal{N}_x$	L^2 $\mathcal{E}_\Theta$	σ_Θ	L^∞ $\mathcal{E}_\Theta$	σ_Θ	$\mathcal{N}_x$	L^2 $\mathcal{E}_\Theta$	σ_Θ	L^∞ $\mathcal{E}_\Theta$	σ_Θ
32	3.06e-04		2.76e-04		32	2.73e-04		2.54e-04	
64	8.48e-05	1.85	1.00e-04	1.47	64	7.49e-05	1.87	9.13e-05	1.48
128	2.19e-05	1.95	2.39e-05	2.06	128	1.98e-05	1.92	2.26e-05	2.01
256	5.17e-06	2.09	4.14e-06	2.53	256	4.99e-06	1.99	3.94e-06	2.52

4.5.4 Non-hydrostatic inertia-gravity waves

The third test case concerns a perturbation on the thermally stratified background (4.3)–(4.4). Considering the values $N = 0.01$ s^{-1}, $g = 9.81$ m s^{-2}, and $T_{\text{ref}} = 300$ K, we obtain the range $\Theta \in [300, 332.19]$ K for $z \in [0, 10]$ km for the background thermal stratification. In a $[0, 300] \times [0, 10]$ km^2 domain we consider the perturbation (see [103] and top left panel of Figure 4.12):

$$\Theta'(x, z, 0) = 0.01 \text{ K} * \frac{\sin(\pi z/H)}{1 + (x - x_c/a)^2}, \tag{4.25}$$

$$H = 10 \text{ km}, \ x_c = 100 \text{ km}, \ a = 5 \text{ km}. \tag{4.26}$$

In addition, there is a background horizontal flow $u = 20 \, \text{m s}^{-1}$. The simulations are performed using an advective time step at CFL = 0.3, that is $\Delta t = \Delta t_A \approx 3.75$ s. The grid spacing is $\Delta x = \Delta z = 250$ m and the trapezoidal time integrator is employed in the second projection. As in the previous cases, boundary conditions are set periodic on the sides and solid walls on top and bottom boundaries.

Unlike the previous test cases, here the dominant dynamics is chiefly wavelike rather than vertically buoyancy-driven. Inertia-gravity waves develop in the horizontal direction, Figures 4.12 and 4.13. The wave dynamics is especially visible in the right panels which show horizontal cuts of the two-dimensional plots at height $z = 5000$ m. A noteworthy feature of the obtained results is the good symmetry of the curves with respect to the centre of the perturbation.

A quantitative comparison between the fully compressible results and the results of [93] is reported in Table 4.7. Maxima and minima of perturbations of velocity components, potential temperature and Exner pressure at final time $\mathcal{T} = 3000$ s are in line with published work. Moreover, the potential temperature profile at final time in the lower right panel of Figure 4.12 bears good comparison with the corresponding picture in [93]. Besides the wave dynamics, the scheme reproduces the correct horizontal advection speed, as the centre of the perturbation is moved horizontally from $x = 100$ km to $x = 100 \, \text{km} + 3000 \, \text{s} * 20 \, \text{m s}^{-1} = 160$ km. This finding corroborates the conclusions of Section 3.2.2 about the vortex advection. The wave dynamics displayed by the vertical velocity (Figure 4.13) is also in agreement with results found in the literature [2]. As in the previous cases, [16] report quantitatively similar results for a thermodynamically consistent version of a pseudo-incompressible model. The total wallclock time for the simulation of Figure 4.12 was 1261 s including output at final time. 43% of the total wallclock time was taken up by the predictor step and 55% by the corrector step.

Table 4.7: Maxima and minima of horizontal velocity u, vertical velocity w potential temperature Θ and Exner pressure $\pi = T\Theta^{-1}$ perturbations at final time $\mathcal{T} = 3000$ s in the present study and [93] for the inertia-gravity waves test case.

	u'_{max}	u'_{min}	w'_{max}	w'_{min}	Θ'_{max}	Θ'_{min}	π'_{max}	π'_{min}
	1.054e-02	-1.06e-02	2.739e-03	-2.262e-03	2.808e-03	-1.526e-03	7.75e-07	-5.27e-07
[93]	1.064e-02	-1.061e-02	2.877e-03	-2.4e-03	2.808e-03	-1.511e-03	9.11e-07	-7.13e-07

Finally, we define conservation errors as:

$$C_\phi = \frac{(\phi_{\text{tot}})_{\mathcal{T}} - (\phi_{\text{tot}})_0}{(\phi_{\text{tot}})_0}, \tag{4.27}$$

where $\phi_{\text{tot}} = \int_\Omega \phi \, d\boldsymbol{x}$ denotes the volumetric integral of ϕ in the domain Ω. Subscripts 0 and $\mathcal{T}$ denote initial and final time, respectively. We expect our scheme to conserve ρ_{tot}, ρu_{tot} and P_{tot}. Though our model does not conserve total energy density E defined in 2.3, we report conservation scores for that variable, too. Values of the conservation error for ρ, ρu and P are fairly low (Table 4.8) in comparison with published work [93].
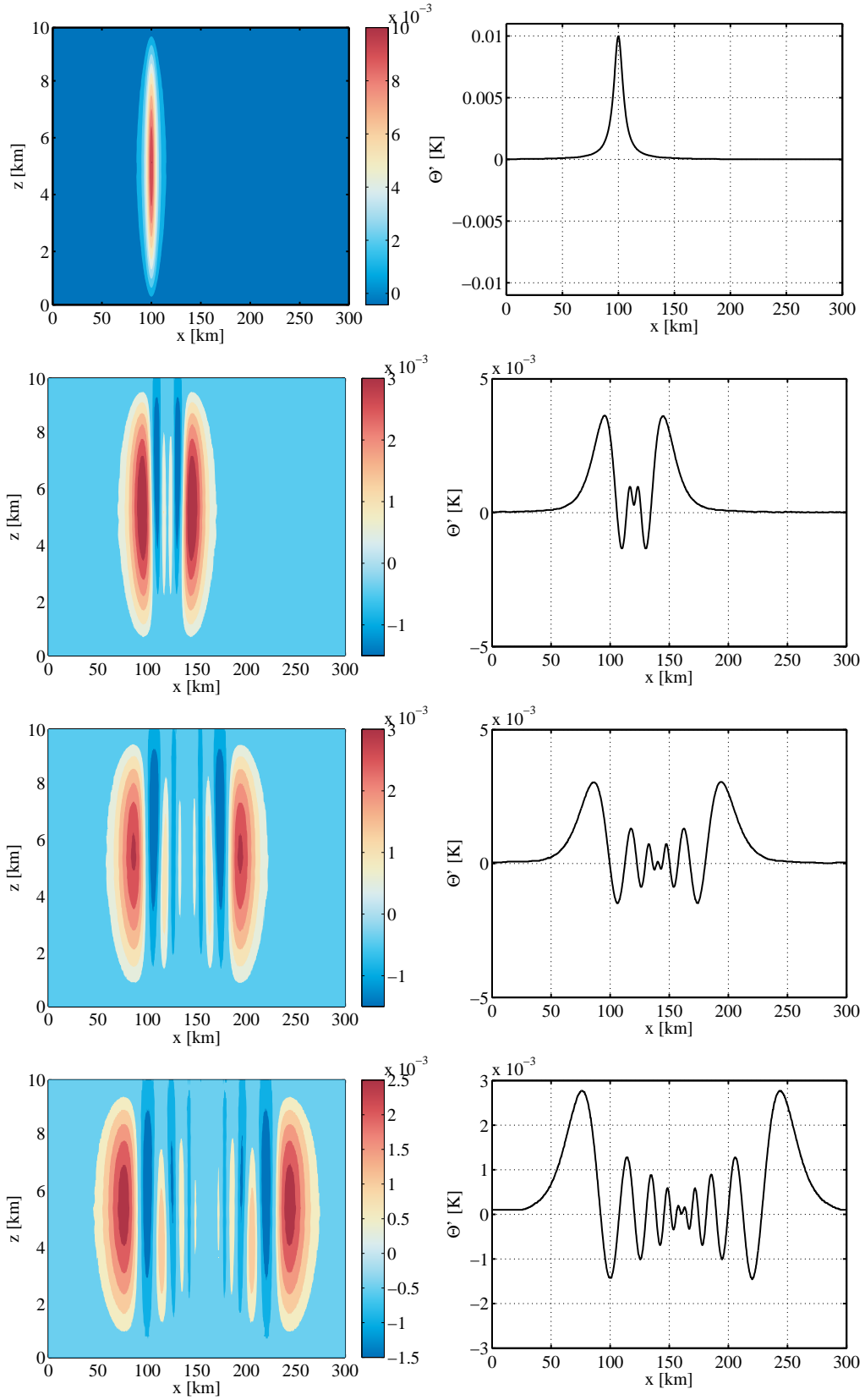
Figure 4.12: Potential temperature perturbation in the inertia-gravity waves test case, large time step results. Left column, top to bottom: initial data, colour shading every 10^{-3} K; computed solution at $t = 1000$ s, $t = 2000$ s, $t = 3000$ s, colour shading every $5 \cdot 10^{-4}$ K in the range $[-0.0015, 0.003]$ K with the 0 K shade removed. Right column: horizontal cut at height $z = 5000$ m. In the bottom right panel, the vertical scale is magnified in agreement with [93].
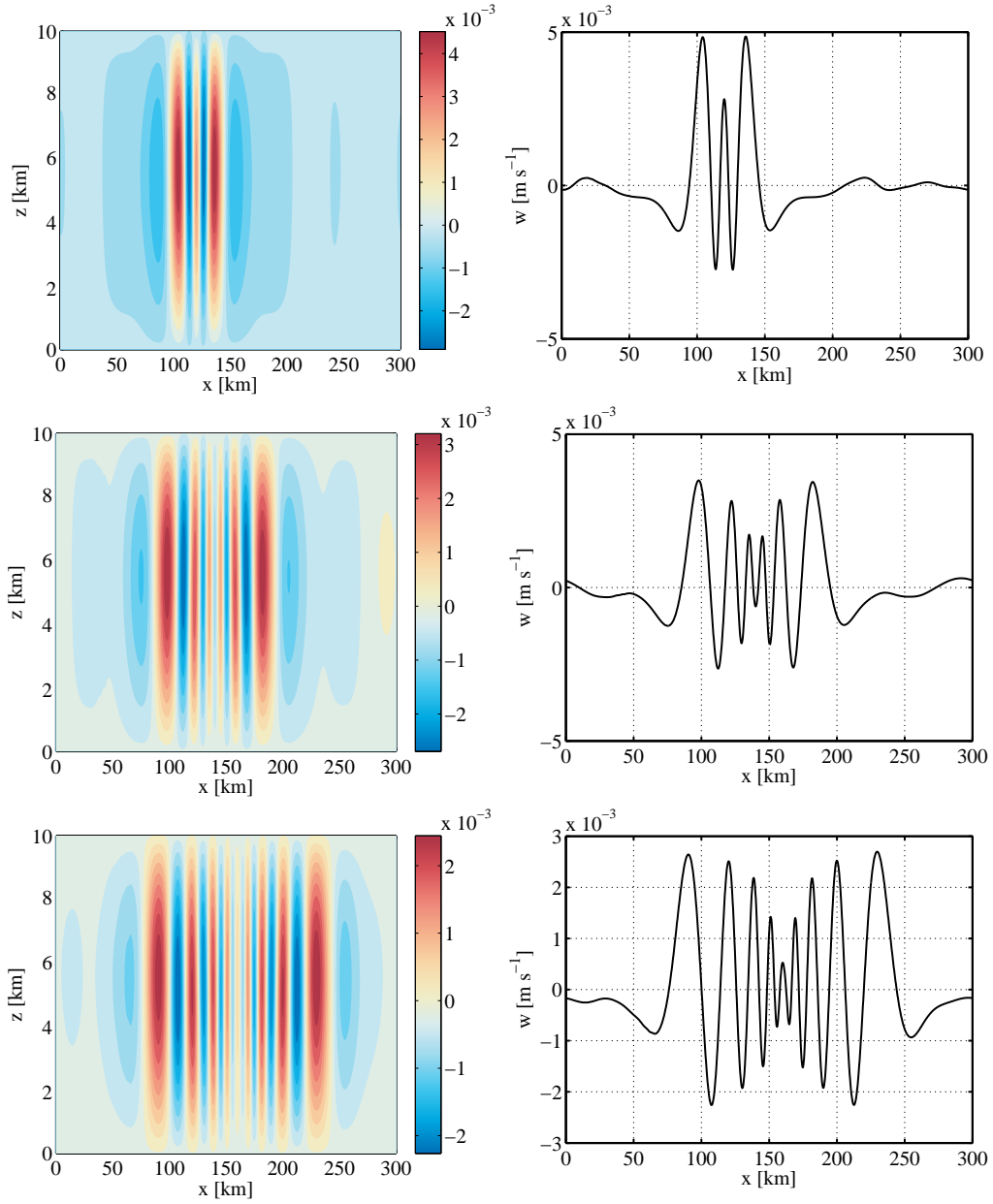
Figure 4.13: Vertical velocity in the inertia-gravity waves test case. Left column, top to bottom: computed solution at $t = 1000$ s, $t = 2000$ s, $t = 3000$ s, 16 colour shades in the intervals (top to bottom) $[-0.0029, 0.0049]$ m s^{-1}, $[-0.0027, 0.0036]$ m s^{-1}, $[-0.0023, 0.0027]$ m s^{-1}, respectively. Right column: horizontal cut at height $z = 5000$ m.

Table 4.8: Conservation errors for density, horizontal momentum density, P and total energy density in the inertia-gravity wave simulation (see text for definitions).

	C_ρ	$C_{\rho|\boldsymbol{v}|}$	C_P	$C_{\rho E}$
	1.15e-09	8.05e-11	5.68e-09	1.98 e-09
[93]	1.67e-08	2.6e-07	\	1.64 E-08

5

A blended soundproof-compressible numerical model

In this chapter we present the blended soundproof-compressible model obtained by extending the techniques described in Chapter 3. The basic idea involves assigning a weight parameter to the time derivative term in the energy equation in order to tune the amount of compressibility simulated by the scheme.

In the following, we reappraise our semi-implicit fully compressible model and describe the modifications required by the blended discretization. Then, we test the features of the blended model in the case of the rising thermal bubble, laying special emphasis on the first stages on the simulations.

5.1 Analytical framework

The blended compressible/pseudo-incompressible equations are given as follows, for $\alpha \in \{0, 1\}$:

$$\rho_t + \nabla \cdot (\rho \boldsymbol{v}) = 0, \tag{5.1a}$$

$$(\rho \boldsymbol{v})_t + \nabla \cdot (\rho \boldsymbol{v} \circ \boldsymbol{v}) + \nabla p = -\rho g \boldsymbol{k}, \tag{5.1b}$$

$$\alpha P_t + \nabla \cdot (P \boldsymbol{v}) = 0. \tag{5.1c}$$

This formulation recovers the fully compressible dynamics for $\alpha = 1$. For $\alpha = 0$ a pseudo-incompressible model as in [61] is accessed. However, unlike [61], the present model works with p and ρ instead of π and θ. As noted, for the purposes of this study we do not consider the thermodynamically consistent modification introduced in [66] and implemented in [16].

In (5.1) the α parameter is introduced to formulate the fully compressible and pseudo-incompressible model in one and the same set of equations. Only discrete values $\alpha \in \{0, 1\}$ make sense to begin with. However, if we consider the equations for any $\alpha \in [0, 1]$, a seamless discretization that allows integration of (5.1) for any of these values can be used to our advantage in some meteorologically interesting situation.

Suppose we are initializing the test case of a rising warm-air bubble as in Section 4.5.2, or of flow over a mountain. Acoustic perturbations are of negligible importance in meteorology, therefore we would like to simulate acoustically balanced flows. In general, the balanced pressure distributions associated with given initial data for potential temperature and velocity cannot be determined analytically. However, we know that

pseudo-incompressible models accurately simulate acoustics-free compressible flows. Then, by running a simulation in pseudo-incompressible mode with $\alpha = 0$ for S_1 time steps, we can generate reasonable approximations to the missing pressure distributions. Next, within S_2 time steps, we increase the value of α continuously from 0 to 1. After time step $S_1 + S_2$ we maintain $\alpha = 1$ to operate the model in fully compressible mode. In this fashion, a compressible flow simulation is obtained that is balanced with respect to acoustic modes.

Such a smooth blending of balanced and unbalanced model equations within a common discretization framework could substantially contribute to resolving similar balancing issues in the context of data assimilation.

5.2 Numerical Framework

In this section, we describe the modifications to the numerical scheme required by the blending feature. Hereafter, we will consider $\alpha \in [0, 1]$. Further discussion on the energetic properties of the blended model for $\alpha \in [0, 1]$ can be found in [65].

Predictor

The auxiliary system (3.1) solved in the predictor step is the same for the compressible and pseudo-incompressible models and is not modified in the blended framework. The discretized equations (3.1) remain the same for all values of α.

Corrector

In the correction step, two elliptic problems are solved by considering the equation:

$$\left[\alpha \left(\frac{\partial P}{\partial t} \right) + \nabla \cdot (P\boldsymbol{v}) \right]^{n+\frac{1}{2}} = 0 \,. \tag{5.2}$$

Expression (5.2) represents a semi-implicit discretization of the energy equation (5.1c) in the fully compressible case for $\alpha = 1$ and the divergence constraint in the pseudo-incompressible case for $\alpha = 0$. Proceeding as in Section 3.1.2, we derive the first discrete Helmholtz problem:

$$-\alpha \left(\frac{\mathcal{C}_H^{n+\frac{1}{2},*}}{\Delta t} \delta p \right)_C + \widetilde{\nabla} \cdot \left[\frac{\Delta t}{2} \Theta^{n+\frac{1}{2},*} \nabla \delta p \right]_C = \widetilde{\nabla} \cdot [(P\boldsymbol{v})^{n+\frac{1}{2},*}]_C. \tag{5.3}$$

We refer to Section 3.1.2 and Equation (3.30) above for definitions. Expression (5.3) is responsible for determining stable time increments of P in the compressible model ($\alpha = 1$). In the pseudo-incompressible case expression (5.3) turns into a standard Poisson pressure projection equation and enforces the divergence constraint for $\alpha = 0$. In this case, the correction of P in (3.33c) automatically yields $P^{n+1} \equiv \overline{P}$ up to the tolerance with which the Poisson equation was solved. Thus, in the pseudo-incompressible case, the pressure variable P is restored to its background value as a result of the first correction. For all values of α,

the fluxes are corrected with the solution of (5.3) via (3.33). Tuning the parameter α determines the amount of compressibility present in the system.

In the second correction step, the following version of the energy equation is considered in the blended case:

$$\alpha \left(\frac{\partial P}{\partial t}\right)^{n+\frac{1}{2}} + \nabla \cdot \left[\theta \frac{2-\alpha}{2} (P\boldsymbol{v})^{n+1} + (1-\theta)\frac{\alpha}{2} (P\boldsymbol{v})^n\right] = 0. \tag{5.4}$$

We recall that θ denotes the off-centring parameter within the trapezoidal discretization in the fully compressible case. For $\alpha = 1$ and $\theta = 1/2$, a second-order accurate trapezoidal discretization of the fully compressible model with no off-centring is obtained. For all the runs in this chapter we kept the value $\theta = 1/2$ fixed. Furthermore, in the pseudo-incompressible case with $\alpha = 0$, the value $\theta = 1$ is automatically enforced to obtain the discrete version of the divergence constraint (2.21c).

Proceeding as in Section 3.1.2 we derive the second discrete elliptic problem:

$$-\alpha \left(\frac{\mathcal{C}_H^{n+1}}{\gamma \Delta t} \delta p_\nu\right)_{\overline{C}} + \widetilde{\nabla} \cdot \left[\theta(2-\alpha)\frac{\Delta t}{4} \Theta^{n+1} \nabla \delta p_\nu\right]_{\overline{C}} = \widetilde{\nabla} \cdot \left[\theta \frac{2-\alpha}{2}(P\boldsymbol{v})^{n+1,**} + \frac{\alpha}{2}(1-\theta)(P\boldsymbol{v})^n\right]_{\overline{C}}. \tag{5.5}$$

For all values of α, the solution of (5.5) is used to update the momentum value according to (3.34).

Pressure update

In the blended case, the nodal pressure update at the end of the time step is modified as follows:

1. As in Section 3.1.2, an auxiliary cell-centred pressure p_c is computed from the energy value P using the inverse of the equation of state (2.10). The result is then interpolated to the nodes:

$$p_c^{n+1} = \left(\frac{P^{n+1,**}}{\rho_{\text{ref}}T_{\text{ref}}}\right)^\gamma p_{\text{ref}}, \qquad p_c^{n+1} \longrightarrow p_{\text{EOS}}^{n+1}. \tag{5.6}$$

2. The obtained value is weighted with the old time level pressure update with the solution of (5.5), δp_ν:

$$p^{n+1} = \alpha p_{\text{EOS}}^{n+1} + (1-\alpha)\left(p^n + \delta p_\nu\right). \tag{5.7}$$

When the model runs in pseudo-incompressible mode with $\alpha = 0$, the node-centred pressure increment δp_ν is added to the old time level value. In compressible mode, with $\alpha = 1$, the new nodal pressure is locked to the energy value imposing the equation of state at a discrete level. For intermediate values of $\alpha \in (0,1)$ the pressure is updated by weighting of the two strategies.

Other solutions are possible and were tested. For example, as a pseudo-incompressible update, an interpolated value of the solution δp_c of the first correction equation (5.3) can be added to the old time level pressure value. In that case the solution of the second Poisson problem only serves as a correction to the momentum flux, expression (3.34), not as an update for the nodal pressure value. However, since we observed no difference by using this method, in all the blended simulations we used expression (5.7) to update the pressure at the end of the time loop.

5.3 Numerical results

In Sections 3.2 and 4.5, we aimed at benchmarking the semi-implicit fully compressible method in simulations of advection and buoyancy-driven flows. With the exception of the energy transport in the vortex case and the simulation of the pressure wave dynamics, the energy derivative term representing compressibility does not bring about significant differences in the result with respect to soundproof runs, as expected in the small to meso-scale environment considered.

In this section, the goal is to show that the blended soundproof-compressible formulation (5.1) can be used to remove the onset of the initial acoustic imbalances generated in the initial stages of compressible runs as the ones observed in Figure 3.6.

More specifically, we reappraise the rising bubble test case and evaluate the capabilities of our blended model. After observing that sizeable pressure imbalances are generated by the compressible model with $\alpha = 1$, the idea is to employ the blending parameter to launch the simulations in pseudo-incompressible mode with $\alpha = 0$. Once a balanced pressure distribution has been achieved within a few time steps, the value of α is gradually increased to 1. Thereafter, the scheme is run in fully compressible mode. It is worth remarking that the character of the tests in this section is mostly "empirical", as an in-depth study of the numerical properties of the blended model for $\alpha \in (0, 1)$ has not been carried out and lies outside the scope of this work. We refer to [65] for further analysis on the properties of the blended system.

Rising bubble

We consider again the test case of a positively buoyant perturbation on the neutrally stratified atmosphere (4.2) studied in Section 4.5.2. As noted, pseudo-incompressible results for velocity and potential temperature do not differ substantially from compressible results at final time, as can be appraised comparing results in Section 4.5.2 with [61], see also [16].

However, the compressible dynamics can be detected in the onset of sound waves in the initial stages of the simulation. With the fully compressible model ($\alpha = 1$) the initial potential temperature perturbation triggers pressure waves. These are visible in the left panel of Figure 5.1, which displays pressure increments in a fully compressible run with $\Delta t = \Delta t_I = 1.9$ s. The oscillations are due to the initial hydrostatic pressure distribution from (4.2) not being acoustically balanced.

The presence of associated pressure oscillations is confirmed by a time series over the first 350 s of the nodal pressure time increment values recorded at the point $(x, z) = (-7.5, 5)$ km, marked with a cross in the left panel of Figure 5.1. The time series is shown in the right panel of Figure 5.1. The oscillations are suppressed in the pseudo-incompressible run (dashed line) except for an initial adjustment.

However, thanks to the blending feature, the code is able to continuously transition from the pseudo-incompressible to the fully compressible configuration. The left panel of Figure 5.2 shows the time series of nodal pressure increments for blended runs. We set the transition parameter α from Section 5.1 to zero
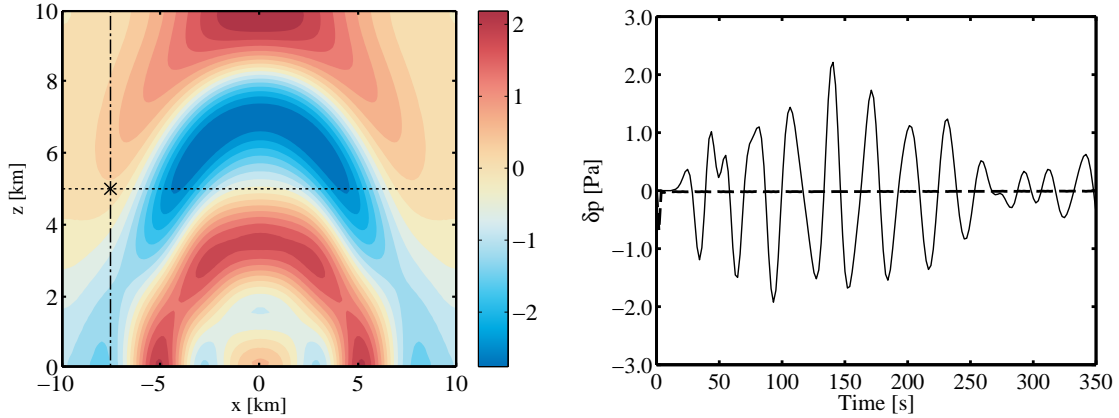
Figure 5.1: Nodal pressure time increment in the rising bubble test case. The time step size is $\Delta t = 1.9$ s. Left panel: 16 colour shades in the interval $[-2.75, 2.49]$ Pa, time step 14 ($t = 26.6$ s), fully compressible model. Right panel: value over the first 350 s measured at the point $(x, z) = (-7.5, 5)$ km (marked with a cross in the left panel) for fully compressible (solid line) and pseudo-incompressible (dashed line) configurations.

for S_1 time steps. Then, we linearly increase the value of α reaching $\alpha = 1$ over S_2 time steps. Starting at the time step number $S_1 + S_2$, the code runs compressibly with $\alpha = 1$.

In the left panel of Figure 5.2, the black curve in the background denotes the fully compressible result. The dashed-dotted red curve and blue dashed curve were obtained with $S_2 = 20$ and $S_2 = 40$, respectively. The right panel of Figure 5.2 displays the parameter α as a function of the time loop for the three cases. There are no disturbances for the first $S_1 = 10$ pseudo-incompressible steps in the two blended curves in the left panel, and the results coincide with those from the run of the pseudo-incompressible model (dashed line in the right panel of 5.1). Perturbations arise in the transitional period after S_1 time steps and fully develop after $S_1 + S_2$ time steps. The amplitudes of the oscillations in the blended runs are considerably lower than those in the fully compressible run and they are lower for the larger S_2 value, that is, the longer the transitional period.

Figure 5.3 offers a two-dimensional representation of the time series of Figure 5.2. The left panels show the temporal evolution of the nodal pressure increment values on the horizontal section $(x, z) \in [-10, 10] \times \{5\}$ km. The right panels show the temporal evolution of the same quantity on the vertical section $(x, z) \in \{-7.5\} \times [0, 10]$ km. The horizontal and vertical sections are marked in the left panel of Figure 5.1 with the dotted and dashed-dotted line, respectively. The time interval considered is $[3.8, 190]$ s, corresponding to the first 100 time steps of the simulation. Note that the data for the first time step are not plotted to remove the adjustment in the first time step of the blended runs. Plots as the ones in Figure (5.3) are known in meteorology as Hovmöller plots and serve as a two-dimensional representation of wave dynamics.

The panels on the top row refer to the compressible run with $\alpha = 1$ and correspond to the black curve in Figure 5.2. A fully developed wave pattern can be seen, roughly corresponding to the crests and troughs in Figure 5.2. The areas colored in red correspond to the passage of a crest through the section, the areas colored in blue to the passage of a trough. Moreover, the wave dynamics can be detected in the diagonal
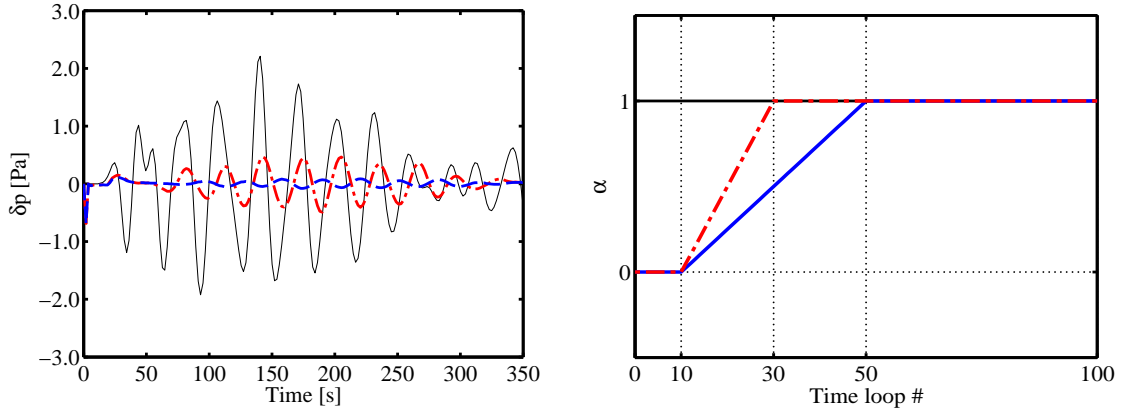
Figure 5.2: Time series of nodal pressure time increment measured at the point $(x, z) = (-7.5, 5)$ km in the rising bubble test case for the first 350 s of a run at $\Delta t = 1.9$ s. Left panel: blended runs with $S_1 = 10$ initial pseudo-incompressible steps and $S_2 = 20$ (red dashed-dotted line) and $S_2 = 40$ (blue dashed line) transitional steps. The thin black line in the background denotes a fully compressible run with $S_1 = S_2 = 0$. The right panel shows the value of α during the first 100 time steps (190 s) in the three cases.

patterns which are especially visible in the right panels.

Plots in the second and third row in Figure 5.3 refer to the blended runs with $S_1 = 10$ initial pseudo-incompressible steps and $S_2 = 20$ (second row) and $S_2 = 40$ (third row) transitional steps, respectively, and correspond to the red and blue curves in Figure 5.2. There is no wave pattern during the first 10 time steps, when the model runs in pseudo-incompressible mode (lower region in the left panels, leftmost region in the right panels). Afterwards, a wave pattern akin to the one in the compressible plots develops. However, the amplitude of the waves is sensibly reduced, see the values on the colorbars. The reduction mirrors the amplitude difference seen in Figure 5.2 for the one-dimensional plot and further highlights the advantage gained by using the blending technique.

Next, we consider the case of simulations at larger time steps. Figures 5.4 and 5.5 show the time series of the nodal pressure increments at the point $(x, z) = (-7.5, 5)$ km and on the vertical section $(x, z) \in \{-7.5\} \times [0, 10]$ km, respectively. Here, the time step is determined as in the simulations of Figure 4.4 with $\text{CFL} = 0.5$ in Equation (3.20), see also Figure 4.5. In Figure 5.4, data for the first time step have not been displayed because of the adjustment present in the pseudo-incompressible and blended cases. The dashed curve in Figure 5.4 displays the result of the pseudo-incompressible run.

The solid line in Figure 5.4 and the left panel of Figure 5.5 refer to the fully compressible run with $\alpha = 1$. The amplitude of the maximum oscillation in Figure 5.4 is substantially reduced with respect to the case of the small time step in Figure 5.2. However, the effect of compressibility is still present, as shown in the fully developed wave dynamics in the Hovmöller plot.

The dashed-dotted curve in 5.4 and the right panel of Figure 5.5 refer to a blended run with $S_1 = 0$ pseudo-incompressible steps and $S_2 = 3$ transition steps. A sizeable reduction in the oscillation amplitude is observed in the one-dimensional curve and is confirmed by the reduced amplitude of crests and troughs in
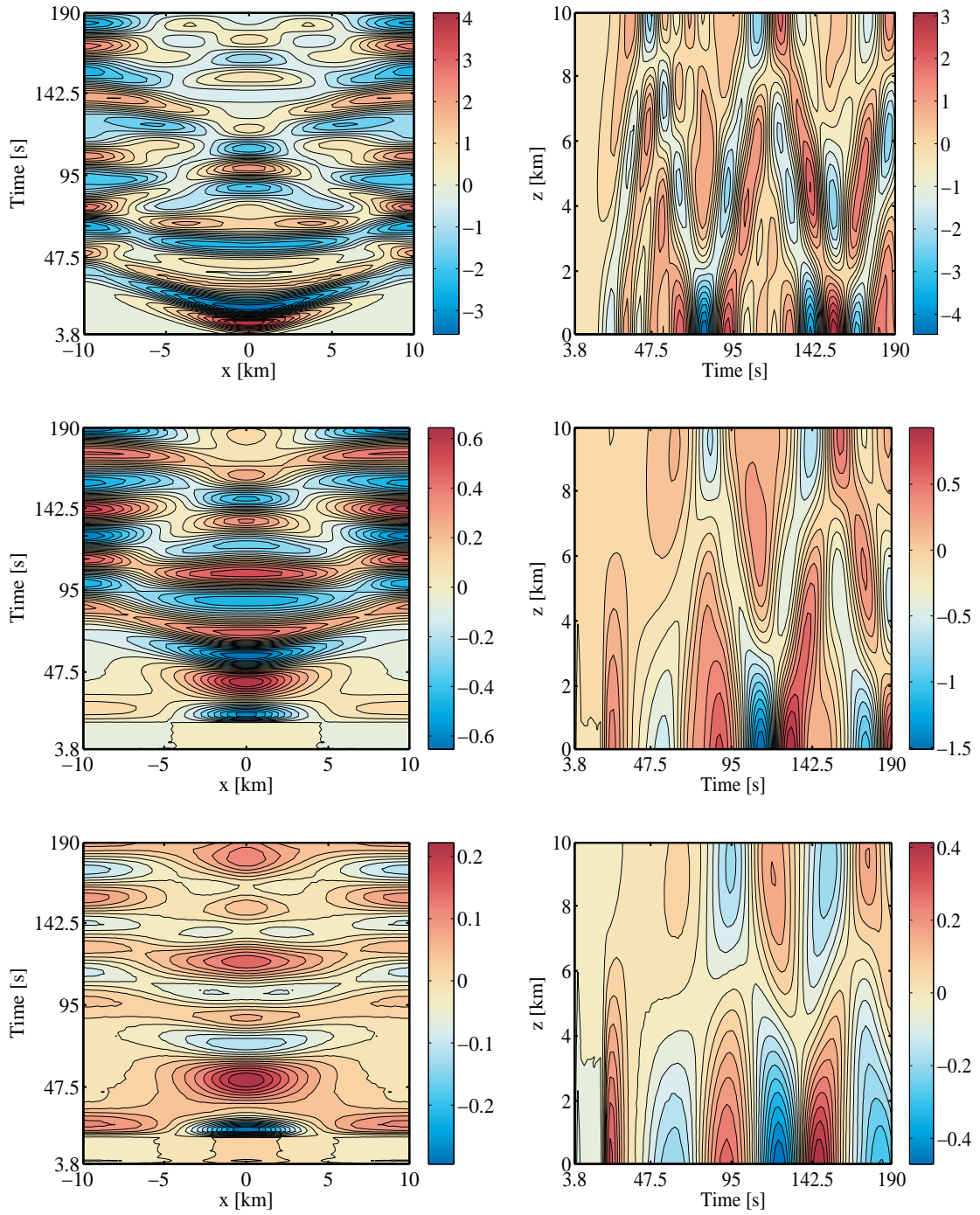
Figure 5.3: Nodal pressure time increments in the rising bubble test case for runs at $\Delta t = 1.9$ s (see Figure 5.2). Hovmöller plots of the sections $(x, z) \in [-10, 10] \times \{5\}$ km (left panels) and $(x, z) \in \{-7.5\} \times [0, 10]$ km (right panels) in the time interval $t \in [3.8, 190]$ s. Top row: fully compressible model; middle and bottom row: blended model with $S_1 = 10$ initial pseudo-incompressible steps and $S_2 = 20$ (middle row) and $S_2 = 40$ (bottom row) transitional steps. For all panels, 20 contour lines are displayed with extrema ([Pa], left to right, top to bottom): $[-3.57, 4.51]$, $[-4.47, 3.45]$, $[-0.65, 0.71]$, $[-1.51, 1.05]$, $[-0.29, 0.25]$, $[-0.47, 0.46]$ (note different values on the colorbars).

the contour plot for the blended run as compared to the compressible contour plot. These results show that a blended soundproof-compressible strategy can be of advantage in reducing acoustic imbalances not only in runs at small, acoustic-resolving time steps, but also in runs at large, advective time steps.
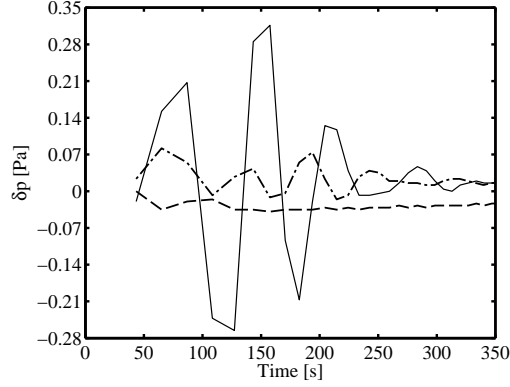

Figure 5.4: Nodal pressure time increment in the rising bubble test case. Value over the first 350 s measured at the point $(x, z) = (-7.5, 5)$ km (marked with a cross in the left panel of Figure 5.2) for fully compressible (solid line) and pseudo-incompressible (dashed line) configurations. The dashed-dotted line is obtained with a blended run with $S_1 = 0$ pseudo-incompressible steps and $S_2 = 3$ fully compressible steps. The time step is determined by CFL $= 0.5$, see Figure 4.5, and the data for the first time step is removed.

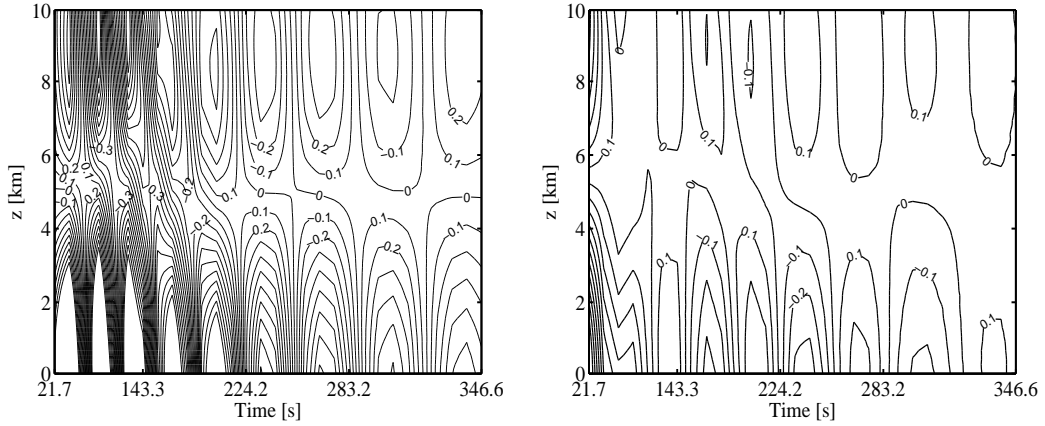**Figure 5.5:** Nodal pressure time increments in the rising bubble test case for runs at CFL $= 0.5$ s (see Figure 5.4). Hovmöller plots of the section $(x, z) \in \{-7.5\} \times [0, 10]$ km in the time interval $t \in [21.7, 346.6]$ s. Left panel: fully compressible model; right panel: blended model with $S_1 = 0$ initial pseudo-incompressible steps and $S_2 = 3$ transitional steps. 20 contour lines in $[-1, 1]$ Pa.

Finally, as in [6], which presents a pseudo-incompressible code for stellar hydrodynamics, we compare plots of the Mach number in the initial stages of fully compressible, pseudo-incompressible, and blended runs of the rising bubble. Results at time $t = 21.66$ s, that is, time step number 57 at $\Delta t = \Delta t_{\mathrm{I}} = 0.38$ s, are displayed in Figure 5.6.

The mushroom-shaped fully compressible result (upper left panel) reveals the initial onset of sound waves

due to the pressure imbalances of the kind inspected in Figure 5.6. The wave dynamics is further highlighted in a Hovmöller plot of the horizontal section $(x, z) \in [-10, 10] \times \{6\}$ km, with the x-coordinate on the horizontal axis and time on the vertical axis (top right panel in Figure 5.6). The triangular shape signalizes the arrival of the first crest after 6 seconds and the ensuing wave propagation typical of the hyperbolic compressible case.

By contrast, the pseudo-incompressible plot (lower left panel in Figure 5.6) and blended plot (lower right panel in Figure 5.6) show no perturbation away from the bubble. A very small time step was considered in this case following [6] in order to track more closely the dynamics in the initial stages.

The situation is further explained in the Hovmöller plots of the vertical velocity in Figure 5.7 in the same run. The upper left panel shows the vertical velocity in the first time step of a pseudo-incompressible run. The dashed line marks the vertical section $(x, z) \in \{0\} \times [0, 10]$ km. The value of the vertical velocity on this section and in the time interval $[0, 21.66]$ s is displayed in the remaining panels.

Away from the bubble perturbation displayed in the red areas, wave dynamics can be noticed in the fully compressible run in the upper right panel of Figure 5.7. The perturbed contours in the upper right region correspond to the mushroom-shaped contour of Figure 5.6. The lower panels of Figure 5.7 correspond to the lower panels of Figure 5.6. The blended plot in the lower right panel lacks acoustic perturbations and approaches the balanced pseudo-incompressible plot as seen in the lower left panel. Results in Figure 5.6 and 5.7 confirm what observed in the studies on pressure perturbations above and provide further evidence for the effectiveness of the blended model.

The numerical results shown in this chapter demonstrate the capabilities of the blended model. Acoustic perturbations are absent when the model runs in pseudo-incompressible mode with $\alpha = 0$ and they emerge significantly damped after the transition to $\alpha = 1$ in fully compressible mode. Therefore, when blended continuously with the compressible discretization, the soundproof limit discretization can be used to actively control imbalances in the initial data.

The blending technique may prove useful whenever new data need to be incorporated in a fully compressible model. In particular, in a data assimilation framework [91], a blended model such as the one we propose would be able to turn to balanced soundproof dynamics as new data arrive from, e.g., an observation station. As noted, these data are generally imbalanced and would spark acoustic oscillations in the framework of fully compressible numerical schemes as seen in Figure 5.1. By resorting to a blended configuration for some time steps, the impact of the acoustic imbalances can be reduced as shown above. After the data assimilation and blending phase, the model can run again in fully compressible mode with the imbalances filtered out.
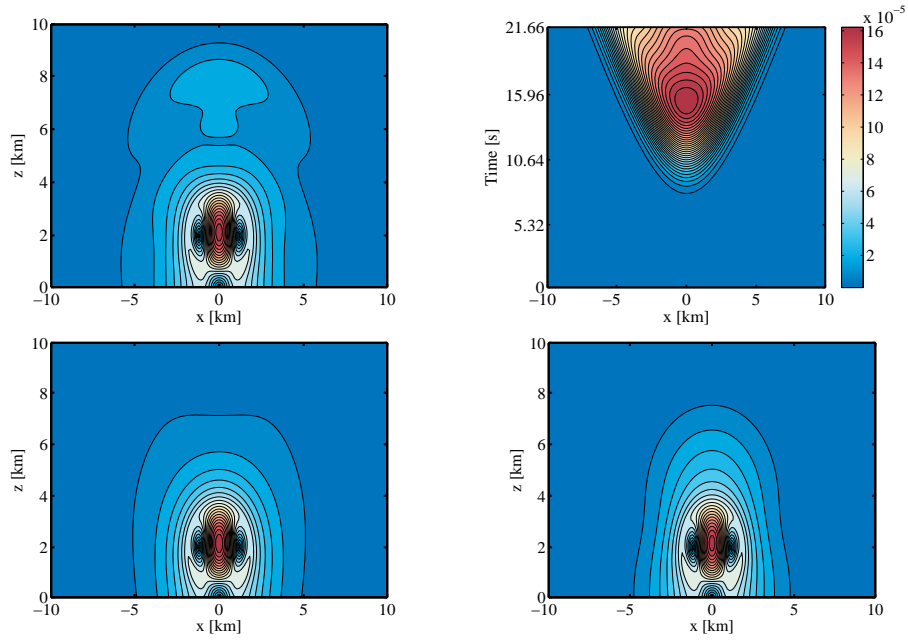
Figure 5.6: Mach number M in the rising bubble test. Upper left and lower panels: value at $t = 21.66$ s, contours every 10^{-4} in the range $[0.0001, 0.002]$; Upper left panel: fully compressible model $S_1 = S_2 = 0$. Lower left panel: pseudo-incompressible model. Lower right panel: blended model $S_1 = 10$, $S_2 = 40$. The upper right panel displays a Hovmöller plots of the horizontal section $(x, z) \in [-10, 10] \times \{6\}$ km in the time interval $t \in [0, 21.66]$ s for the fully compressible run.
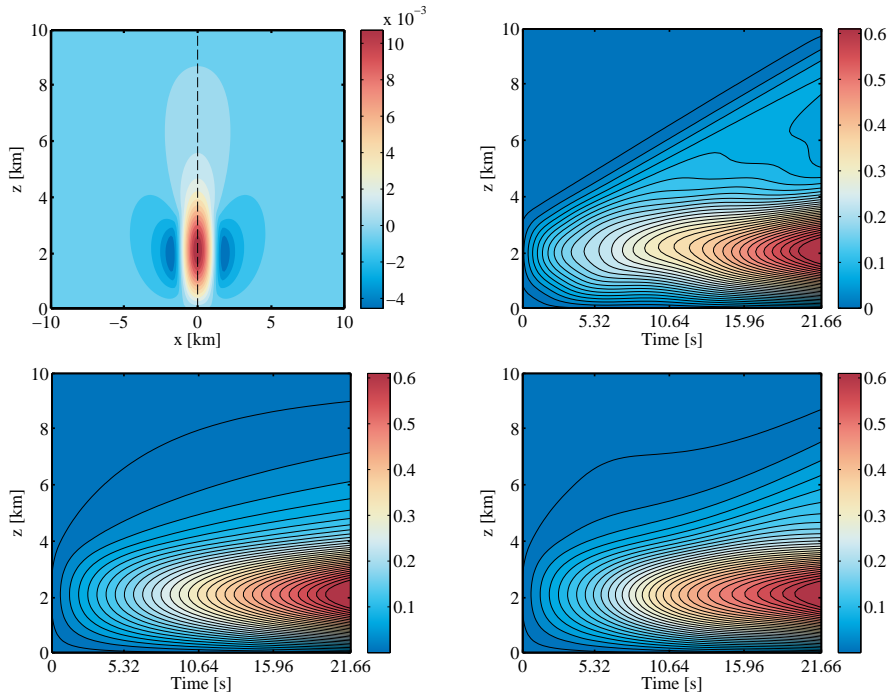

Figure 5.7: Vertical velocity in the rising bubble test case, $\Delta t = 0.38$ s. The upper left panel shows the value at the first time step of a pseudo-incompressible run with 16 colour shades in $[-0.0045, 0.011]$ m s^{-1}. The remaining panels display the Hovmöller plots of the vertical section $(x, z) \in \{0\} \times [0, 10]$ km marked with a dashed line on the upper left panel. 30 contours in $[0.01, 0.61]$ m s^{-1} are shown for the fully compressible model (upper right panel), pseudo-incompressible model (lower left panel) and blended model with $S_1 = 10$, $S_2 = 40$ (lower right panel).

6

Extension to a scheme with implicit buoyancy

The fully compressible numerical scheme constructed in Chapter 3 together with the buoyancy discretization described in Chapter 4 is implicit only with respect to sound waves. Such a scheme is sufficient to simulate flows in a neutrally-stratified environment with time steps constrained only by the advection speed [116]. The thermal perturbations considered in Sections 4.5.2 and 4.5.3 belong to this category.

However, under hydrostatic conditions, i.e. when the domains considered have a large aspect ratio of horizontal to vertical scales, the time step that can be used with a scheme implicit only with respect to sound waves is additionally constrained by $1/N$ [116]. If we recall that a value of $N = 0.01$ s^{-1} is usually adopted in the troposphere, the additional threshold entails a significant efficiency burden in flow simulations at large scales. The case of the inertia-gravity waves considered in Chapter 4 is generally regarded as nonhydrostatic in the literature.

In this chapter we will present an extension of our semi-implicit scheme to the implicit treatment of buoyancy processes. This development is necessary to extend the results presented in the previous chapters to larger scales for which the aforementioned additional threshold on the time step size holds.

As noted, existing semi-implicit numerical schemes that treat sound waves as well as gravity waves implicitly are traditionally written in terms of perturbations around hydrostatically balanced states, see, e.g., [29, 93, 109, 115, 133]. Our goal in this chapter will be to derive such a discretization while working with full variables.

6.1 The buoyancy-implicit corrections

In the following we will explain the modifications introduced in the implicit correction step in order to account for an implicit treatment of buoyancy.

First correction step

We will proceed as in Section 3.1.2 and start our analysis from the momentum equation (2.12b) integrated over a half time step. Considering it in advective form we have:

$$\boldsymbol{v}^{n+\frac{1}{2}} = \boldsymbol{v}^n - \frac{\Delta t}{2} \left[\nabla \cdot (\boldsymbol{v} \circ \boldsymbol{v})\right]^{n+\frac{1}{4}} - \frac{\Delta t}{2} (g\boldsymbol{k})^{n+\frac{1}{4}} - \frac{\Delta t}{2} \left(\frac{1}{\rho}\nabla p\right)^{n+\frac{1}{4}}. \tag{6.1}$$

Then we consider the following expansions, neglecting higher-order terms:

$$\frac{1}{\rho} = \left(\frac{\Theta}{P}\right)^* + \delta\left(\frac{\Theta}{P}\right) \tag{6.2}$$

$$p^{n+\frac{1}{4}} = p^* + \delta p \tag{6.3}$$

and define:

$$\delta\boldsymbol{v} \equiv \boldsymbol{v}^{n+\frac{1}{2}} - \boldsymbol{v}^{n+\frac{1}{2},*}. \tag{6.4}$$

In particular, in (6.4) the term:

$$\boldsymbol{v}^{n+\frac{1}{2},*} = \boldsymbol{v}^n - \frac{\Delta t}{2} \left[\nabla \cdot (\boldsymbol{v} \circ \boldsymbol{v})\right]^{n+\frac{1}{4}} - \frac{\Delta t}{2} (g\boldsymbol{k})^{n+\frac{1}{4}} - \frac{\Delta t}{2} \left(\frac{1}{\rho}\right)^* (\nabla p)^* \tag{6.5}$$

denotes the predicted velocity.

Above, unknown variables are decomposed into predictor-computed quantities, denoted by an asterisk, and an increment, denoted by δ. As a result, we get, once more neglecting higher-order terms:

$$\delta\boldsymbol{v} = -\frac{\Delta t}{2} \left(\frac{\Theta}{P}\right)^* \nabla\delta p - \frac{\Delta t}{2P^*}\delta\Theta\nabla p^* - \frac{\Delta t}{2}\Theta^*\delta\left(\frac{1}{P}\right)\nabla p^*. \tag{6.6}$$

In an adiabatic setting, the equation for potential temperature reads:

$$\frac{d\Theta}{dt} = 0. \tag{6.7}$$

We integrate this equation over a half time step. Subtracting from the equation:

$$\Theta^{n+\frac{1}{2}} - \Theta^n = -\frac{\Delta t}{2}\boldsymbol{v}^{n+\frac{1}{2}} \cdot \nabla\Theta \tag{6.8}$$

the expression:

$$\Theta^{n+\frac{1}{2},*} - \Theta^n = -\frac{\Delta t}{2}\boldsymbol{v}^{n+\frac{1}{2},*} \cdot \nabla\Theta \tag{6.9}$$

we obtain:

$$\Theta^{n+\frac{1}{2}} - \Theta^{n+\frac{1}{2},*} \equiv \delta\Theta = -\frac{\Delta t}{2}\delta\boldsymbol{v} \cdot \nabla\Theta^* \tag{6.10}$$

where Θ^* was considered inside the gradient in the last term, as scalars computed in the predictor are already second-order accurate. Replacing now (6.6) into (6.10) we have

$$\delta\Theta = \frac{\Delta t^2}{4}\left[\left(\frac{\Theta}{P}\right)^*\nabla\delta p + \frac{1}{P^*}\delta\Theta\nabla p^* + \Theta^*\delta\left(\frac{1}{P}\right)\nabla p^*\right]\cdot\nabla\Theta^* \tag{6.11a}$$

$$= \frac{\Delta t^2}{4}\frac{\left(\frac{\Theta}{P}\right)^*\nabla\delta p + \Theta^*\delta\left(\frac{1}{P}\right)\nabla p^*}{1 - \frac{\Delta t^2}{4}\frac{1}{P^*}\nabla p^*\cdot\nabla\Theta^*}\cdot\nabla\Theta^*. \tag{6.11b}$$

For brevity, we set:

$$\chi := \frac{1}{1 - \frac{\Delta t^2}{4}\frac{1}{P^*}\nabla p^*\cdot\nabla\Theta^*}. \tag{6.12}$$

Replacing back (6.11b) into (6.6) we obtain:

$$\delta\boldsymbol{v} = -\frac{\Delta t}{2}\left(\frac{\Theta}{P}\right)^*\nabla\delta p - \frac{\Delta t^3}{8}\frac{\chi}{P^*}\left\{\left[\left(\frac{\Theta}{P}\right)^*\nabla\delta p + \Theta^*\delta\left(\frac{1}{P}\right)\nabla p^*\right]\cdot\nabla\Theta^*\right\}\nabla p^* - \frac{\Delta t}{2}\Theta^*\delta\left(\frac{1}{P}\right)\nabla p^* \tag{6.13a}$$

$$= -\frac{\Delta t}{2}\Theta^*\left\{\underbrace{\frac{1}{P^*}\nabla\delta p}_{1} + \underbrace{\frac{1}{P^*}\frac{\Delta t^2}{4}\frac{\chi}{P^*}(\nabla\delta p\cdot\nabla\Theta^*)\nabla p^*}_{2} + \underbrace{\delta\left(\frac{1}{P}\right)\nabla p^*\left[1 + \frac{\Delta t^2}{4}\frac{\chi}{P^*}(\nabla p^*\cdot\nabla\Theta^*)\right]}_{3}\right\}. \tag{6.13b}$$

Finally, replacing (6.13b) into the energy equation at the half time level:

$$\left[\alpha\frac{\partial P}{\partial t} + \nabla\cdot(P^*\boldsymbol{v}^* + P^*\delta\boldsymbol{v})\right]^{n+\frac{1}{2}} = 0 \tag{6.14}$$

we obtain the modified discrete Helmholtz equation:

$$\alpha\left(\frac{\mathcal{C}_H^{n+\frac{1}{2}}}{\Delta t}\delta p\right)_C - \frac{\Delta t}{2}\widetilde{\nabla}\cdot\left(\underbrace{\Theta^*\nabla\delta p}_{1}\right)_C - \frac{\Delta t}{2}\widetilde{\nabla}\cdot\left[\underbrace{\Theta^*\frac{\Delta t^2}{4}\frac{\chi}{P^*}(\nabla\delta p\cdot\nabla\Theta^*)\nabla p^*}_{2}\right]_C$$

$$- \frac{\Delta t}{2}\widetilde{\nabla}\cdot\left\{\underbrace{\Theta^*P^*\delta\left(\frac{1}{P}\right)\nabla p^*\left[1 + \frac{\Delta t^2}{4}\frac{\chi}{P^*}(\nabla p^*\cdot\nabla\Theta^*)\right]}_{3}\right\}_C = -\widetilde{\nabla}\cdot\left[(P\boldsymbol{v})^*\right]_C \tag{6.15}$$

where:

$$\mathcal{C}_H^{n+\frac{1}{2}} = \left(\frac{\partial P}{\partial p}\right)^{n+\frac{1}{2}}. \tag{6.16}$$

In order to simplify expression (6.15), we make the approximation of considering only the vertical base state contributions $\overline{\Theta}$ and $\overline{p}$ in the gradients in the denominator of expression (6.11b), i.e.:

$$\nabla\Theta^* = \boldsymbol{k}\frac{d\overline{\Theta}}{dz} = \boldsymbol{k}\frac{\overline{\Theta}}{g}N^2 \tag{6.17}$$

$$\nabla p^* = \boldsymbol{k}\frac{d\overline{p}}{dz} = -\overline{\rho}g\boldsymbol{k} \tag{6.18}$$

where we used hydrostatic balance and the definition of the buoyancy frequency:

$$N^2 = \frac{g}{\overline{\Theta}} \frac{d\overline{\Theta}}{dz}. \tag{6.19}$$

Furthermore, if we write:

$$\delta\left(\frac{1}{P}\right) = -\frac{1}{P^2}\delta P \approx -\frac{1}{(P^*)^2}\mathcal{C}_H^{n+\frac{1}{2}}\delta p \tag{6.20}$$

then using (6.17) and (6.18) expression (6.12) becomes:

$$\chi = \frac{1}{1 + \frac{\Delta t^2}{4}N^2}. \tag{6.21}$$

Hence we have, for expressions grouped into 2 and 3 of Equation (6.15):

$$\Theta^*\frac{\Delta t^2}{4}\frac{\chi}{P^*}\left(\nabla\delta p \cdot \nabla\Theta^*\right)\nabla p^* = \Theta^*\frac{\Delta t^2}{4}\frac{\chi}{P^*}\left(\nabla\delta p \cdot \boldsymbol{k}\frac{\overline{\Theta}}{g}N^2\right)(-\overline{\rho}g\boldsymbol{k}) \tag{6.22}$$

$$= -\Theta^*\frac{\Delta t^2}{4}\chi N^2\left(\boldsymbol{k}\circ\boldsymbol{k}\right)\nabla\delta p \tag{6.23}$$

and

$$\Theta^*P^*\delta\left(\frac{1}{P}\right)\nabla p^*\left[1 + \frac{\Delta t^2}{4}\frac{\chi}{P^*}\left(\nabla p^* \cdot \nabla\Theta^*\right)\right] = \Theta^*P^*\left[-\frac{1}{(P^*)^2}\right]\mathcal{C}_H^{n+\frac{1}{2}}\delta p\,(-\overline{\rho}g\boldsymbol{k})\left(1 - \frac{\Delta t^2}{4}\chi N^2\right) \tag{6.24}$$

$$= \mathcal{C}_H^{n+\frac{1}{2}}g\boldsymbol{k}\left(1 - \frac{\Delta t^2}{4}\chi N^2\right)\delta p \tag{6.25}$$

respectively, where we used (6.20) and the fact that, up to higher-order terms, $P^* = \overline{P} = \overline{\rho}\overline{\Theta}$.

Replacing expressions (6.23) and (6.25) into the Helmholtz problem (6.15) we obtain:

$$\alpha\left(\frac{\mathcal{C}_H^{n+\frac{1}{2}}}{\Delta t}\delta p\right)_C - \frac{\Delta t}{2}\widetilde{\nabla}\cdot\left\{\Theta^*\left[\mathsf{I} - (\boldsymbol{k}\circ\boldsymbol{k})\frac{\Delta t^2}{4}\chi N^2\right]\nabla\delta p\right\}_C$$
$$- \frac{\Delta t}{2}\widetilde{\nabla}\cdot\left[\mathcal{C}_H^{n+\frac{1}{2}}g\boldsymbol{k}\left(1 - \frac{\Delta t^2}{4}\chi N^2\right)\delta p\right]_C = -\widetilde{\nabla}\cdot\left[(P\boldsymbol{v})^*\right]_C \tag{6.26}$$

that is:

$$-\alpha\left(\frac{\mathcal{C}_H^{n+\frac{1}{2}}}{\Delta t}\delta p\right)_C + \frac{\Delta t}{2}\widetilde{\nabla}\cdot\left\{\Theta^*\left[\mathsf{I} - (\boldsymbol{k}\circ\boldsymbol{k})\frac{\Delta t^2}{4}\chi N^2\right]\nabla\delta p\right\}_C$$
$$+ \frac{\Delta t}{2}\widetilde{\nabla}\cdot\left[\mathcal{C}_H^{n+\frac{1}{2}}g\boldsymbol{k}\left(1 - \frac{\Delta t^2}{4}\chi N^2\right)\delta p\right]_C = \widetilde{\nabla}\cdot\left[(P\boldsymbol{v})^*\right]_C \tag{6.27}$$

where I denotes the identity tensor, and $\circ$ the tensor product.

Iterating the procedure in the second projection as done in Section 3.1.2 leads to a second Helmholtz problem of the same form as (6.27) centred on the dual cells $\overline{C}$. The resulting discretization is implicit with respect to gravity waves as well as to sound waves. In (6.27) the information on the stratification is embedded in the modified coefficient of the second-order term and the additional first-order term.

7

Conclusions and outlook

We have presented a semi-implicit fully compressible numerical model for the simulation of atmospheric flows at low Mach number. The scheme is derived as a direct extension of a pseudo-incompressible sound-proof framework [61]. The two-time-level conservative finite volume method integrates the nonlinear partial differential equations representing mass, momentum and energy conservation using a two-step approach.

An explicit predictor provides second-order accurate scalars via linear reconstructions for the computation of fluxes. The pressure variable is at the old time level in the predictor, which features a stability condition unconstrained by the speed of sound waves. In the compressible case, the pseudo-incompressible divergence constraint coming from the energy equation is extended to include the time derivative term. The neglect of the constraint and the use of the old time level pressure in the predictor are corrected with the solution of two elliptic problems for cell-centred and nodal pressure increments. Using the equation of state, the time derivative term in the P equation is implemented as an additional zero-order term in the matrix of the two Helmholtz equations, thereby implying virtually no computational overhead with respect to the soundproof case.

The properties of the compressible flow solver were tested in a low-speed, small-scale environment on the transport of a smooth axysimmetric vortex. The scheme was shown to advect the vortex at the correct speed. Furthermore, the pressure increments coming from the solution of the two Helmholtz problems were shown to yield consistent values, thus validating the adopted strategy. In terms of accuracy, the quadratic convergence rate was verified both with respect to initial data and in the framework of self-convergence tests. We remark that weak instabilities observed in the vortex case for CFL ≥ 0.6 may be amended by employing a different time integrator in the predictor or by adopting an exact projection strategy in the corrector step as in [122]. These solutions are left for future work. Compressibility was observed in imbalances of the pressure distribution in the initial stages of the vortex runs. Moreover, the study of the propagation of a simple acoustic wave further highlighted the properties of the scheme in the simulation of compressibility in the low Mach number regime.

Next, the discretization of the gravity term has been discussed. A strategy that mirrors the advection of $1/\Theta$ in the predictor was adopted that enables the use of buoyancy-driven time steps up to CFL $= 0.99$.

Accuracy was maintained working with full variables in a well-balanced framework [19, 61]. Modifications were required in the implementation of initial data, node-cell interpolations and boundary conditions in order to preserve hydrostatic balance at the discrete level. The absence of spurious velocities was verified on resting neutrally and stably stratified atmospheres. Then, the dynamics of thermal perturbations was simulated with large time steps in a small and meso-scale environment. On the one hand, the compressible results were in agreement with the soundproof results as expected at the scales under consideration. On the other hand, in all of these benchmarks the proposed scheme bore satisfactory comparison with established approaches in the literature as measured with reference to published work on nohydrostatic compressible models. Weak checkerboard modes were observed in runs at acoustics-resolving time steps. Considering different approaches for the time integrator in the predictor may be of advantage in tackling this issue before adopting well-established filtering techniques, which were not adopted in the present work. We also refer to the literature for the description of instabilities arising in the context of projection methods for incompressible flows [4, 94]. The issue currently remains object of research in the framework of the model proposed here.

By exploiting the modular character of the compressibility addition in the scheme, the system has then been cast in a novel blended soundproof-compressible formulation. The blending was accomplished by attaching a switching parameter to the compressibility term in the energy equation. In view of the previous developments, the multimodel formulation only required minor changes in the implementation. The resulting blended scheme flexibly integrates different systems with virtually the same numerics. The blended approach was shown to be of advantage in filtering acoustic imbalances in the initial stages of compressible runs of a rising warm air bubble. Launching the code in pseudo-incompressible mode and then smoothly turning on compressibility, fully compressible simulations effectively balanced with respect to acoustics were obtained.

Finally, an extension of the scheme to implicit buoyancy has been presented. The proposed modification involves minor changes in the coefficients of the elliptic problems in the correction step, thus entailing negligible additional computational cost.

A remark is in order on the motivation that has driven the present work. On the one hand, we very much subscribe to the common knowledge that sound waves do not play a significant role in small to mesoscale atmospheric dynamics. Indeed, the results presented in Chapters 3 and 4 as produced by the compressible scheme are very similar to the results obtained with pseudo-incompressible runs [16]. In this sense, our study corroborates the recent published work on the employability of soundproof models for the simulations of small to mesoscale motions under realistic assumptions on the potential temperature stratification [1, 62, 108]. On the other hand, as pointed out in the mentioned comparison studies [32], compressibility exerts a nontrivial influence on the structure of slower internal waves, and this influence can only be detected by solving the fully compressible equations. The compressible solver developed in the present work defaults to pseudo-incompressible behaviour by design on small scales. Therefore, rather than

trying to identify a "better" model depending on the scale under consideration, our goal has been to show that a systematic approach can be adopted that considers both a general and a reduced analytical model – indeed a seamless blending of the two models – with minor differences in the numerics. We believe such an approach can be frutiful in evaluating the respective merits of different modelling choices especially with a view to the smaller and smaller scales accessible by future schemes.

The choice of keeping the formulation in terms of pressure and density instead of the more traditional Exner pressure and potential temperature was taken in agreement with the coding framework upon which the developments described in this work draw. Moreover, as discussed in [66, 86], the choice increases flexibility towards extensions to more complicated equations of state.

On the point of efficiency, our scheme requires the solution of an additional elliptic problem with respect to most of the existing semi-implicit integrators in the literature. However, the computational burden of our corrector step appears to be put into perspective by the observed share of wallclock time taken up by the solution of the elliptic problems. In this regard the authors of [109] observed better conditioning properties in the compressible Helmholtz problem than in the soundproof Poisson problems.

As for the choice of a discretization independent of a hydrostatically balanced background state, parallel research endeavours are currently in progress on the subject, see, e.g., [128]. From a qualitative point of view, one of the noteworthy features of our scheme is the relative simplicity of its analytical and numerical formulation compared with existing approaches written in terms of perturbations.

As noted, the blending feature has interesting potential applications in the field of atmospheric data assimilation [91]. In that context the ability to insert new imbalanced data in the model without ad hoc filtering techniques appears especially attractive. Such an approach may also be employed in mapping external data into a multidimensional finite volume scheme as in [135]. Furthermore, the idea of blending may be also useful as an alternative to the mentioned existing unified multiscale approaches [7, 35, 69] in handling flows near to hydrostatic or geostrophic balance at synoptic and larger scales. An ideal development of the current blended scheme would be a blended pseudo-incompressible nonhydrostatic/fully compressible/hydrostatic model with tunable switching depending on the scale of the flow under consideration. Such a development would allow for enhanced flexibility and further comparisons with results obtained with reduced models on a broader range of scales.

A number of further developments and avenues of research are worth exploring based on the ideas presented in this work. First, the implicit treatment of gravity waves needs to be fully investigated. Once done, a comparison will be possible with existing approaches on the simulation of baroclinic waves at synoptic scales [69, 109]. With a suitable implementation of orography, the scheme could be compared with existing approaches for the simulation of mountain waves on mesoscales [18, 44, 61] and further soundproof-compressible evaluations. In this connection, a careful choice of a suitable absorbing layer will be needed [15]. Second, if the model is to run in a multiscale setting, a scale-aware time integrator will be of advantage, too. An interesting development in this respect will be a multidimensional fully compressible

implementation of the scale-selective techniques described in [121,123]. There, different time discretization strategies are combined in a multigrid approach in time that exploits damping and dispersion properties of different time integrators used to approximate the model on different grids in a suitable weighted fashion. Third, the implementation of a three-dimensional version of the present scheme will be facilitated by the 3d-ready object-oriented framework of our implementation, while the methods described in [23] appear to suit well for a formulation on a spherical grid. After systematic efficiency and scalability studies, direct comparisons will then be possible between existing approaches [106] and developments of the model proposed in this dissertation on three-dimensional test cases on the sphere.

References

[1] Achatz, U., Klein, R., Senf, F.: Gravity waves, scale asymptotics and the pseudo-incompressible equations. Journal of Fluid Mechanics **663**, 120–147 (2010)

[2] Ahmad, N., Lindeman, J.: Euler solutions using flux-based wave decomposition. International Journal for Numerical Methods in Fluids **54**, 47–72 (2007)

[3] Almgren, A., Bell, J., Colella, P., Howell, L., Welcome, M.: A conservative adaptive projection method for the variable density incompressible Navier-Stokes equations. Journal of Computational Physics **142**, 1–46 (1998)

[4] Almgren, A., Bell, J., Crutchfield, W.: Approximate projection methods: Part I. Inviscid analysis. SIAM Journal on Scientific Computing **22**, 1139–1159 (2000)

[5] Almgren, A., Bell, J., Szymczak, W.: A numerical method for the incompressible Navier-Stokes equations based on an approximate projection. SIAM Journal on Scientific Computing **17**, 358–369 (1996)

[6] Almgren, A.S., Bell, J.B., Rendleman, C.A., Zingale, M.: Low Mach number modeling of type Ia supernovae. I. Hydrodynamics. The Astrophysical Journal **637**, 922–936 (2006)

[7] Arakawa, A., Konor, C.S.: Unification of the anelastic and quasi-hydrostatic systems of equations. Monthly Weather Review **137**, 710–726 (2009)

[8] Baldauf, M.: A new fast-waves solver for the Runge-Kutta dynamical core. Tech. rep., Deutscher Wetterdienst (2013). URL http://cosmo-model.cscs.ch/content/model/documentation/techReports/docs/techReport21.pdf. Last accessed: April 3, 2014

[9] Baldauf, M., Seifert, A., Förstner, J., Majewski, D., Raschendorfer, M., Reinhardt, T.: Operational convective-scale numerical weather prediction with the COSMO model: Description and sensitivities. Monthly Weather Review **139**, 3887–3905 (2011)

[10] Bannon, P.R.: On the anelastic approximation for a compressible atmosphere. Journal of the Atmospheric Sciences **53**, 3618–3628 (1996)

[11] Behrens, J.: Atmospheric and ocean modeling with an adaptive finite element solver for the shallow-water equations. Applied Numerical Mathematics **26**, 217–226 (1998)

[12] Bell, J., Howell, L., Colella, P.: An efficient second-order projection method for viscous incompressible flow (1991)

[13] Bell, J.B., Colella, P., Glaz, H.: A second order projection method for the incompressible Navier-Stokes equations. Journal of Computational Physics **85**, 257–283 (1989)

[14] Bell, J.B., Marcus, D.L.: A second-order projection method for variable-density flows. Journal of Computational Physics **101**, 334–348 (1992)

[15] Benacchio, T., Bonaventura, L.: Absorbing boundary conditions: a spectral collocation approach. International Journal for Numerical Methods in Fluids **72**, 913–936 (2013)

[16] Benacchio, T., O'Neill, W.P., Klein, R.: A blended sound-proof-to-compressible model for small to meso-scale atmospheric dynamics. Monthly Weather Review. In press, DOI: 10.1175/MWR-D-13-00384.1

[17] Bijl, H., Wesseling, P.: A unified method for computing incompressible and compressible flows in boundary-fitted coordinates. Journal of Computational Physics **141**, 153–173 (1998)

[18] Bonaventura, L.: A semi-implicit semi-Lagrangian scheme using the height coordinate for a nonhydrostatic and fully elastic model of atmospheric flows. Journal of Computational Physics **158**, 186–213 (2000)

[19] Botta, N., Klein, R., Langenberg, S., Lützenkirchen, S.: Well balanced finite volume methods for nearly hydrostatic flows. Journal of Computational Physics **196**, 539–565 (2004)

[20] Boussinesq, J.: Théorie analythique de la chaleur, vol. 2. Gathier-Villars (1903)

[21] Brdar, S., Baldauf, M., Dedner, A., Klöfkorn, R.: Comparison of dynamical cores for NWP models: comparison of COSMO and Dune. Theoretical and Computational Fluid Dynamics **27**, 453–472 (2013)

[22] Brown, B., Vasil, G., Zweibel, E.: Energy conservation and gravity waves in sound-proof treatments of stellar interiors. Part I. Anelastic approximations. The Astrophysical Journal **756**, 109–128 (2012)

[23] Calhoun, D.A., Helzel, C., LeVeque, R.J.: Logically rectangular grids and finite volume methods for PDEs in circular and spherical domains. SIAM Review **50**, 723–752 (2008)

[24] Casulli, V., Greenspan, D.: Pressure method for the numerical solution of transient, compressible fluid flows. International Journal for Numerical Methods in Fluids **4**, 1001–1012 (1984)

[25] Childs, H., Brugger, E., Bonnell, K., Meredith, J., Miller, M., Whitlock, B., Max, N.: A contract based system for large data visualization. In: Visualization, 2005. VIS 05. IEEE, pp. 191–198 (2005)

[26] Chorin, A.J.: A numerical method for solving incompressible viscous flow problems. Journal of Computational Physics **2**, 12–26 (1967)

[27] Colella, P., Pao, K.: A projection method for low speed flows. Journal of Computational Physics **149**, 245–269 (1999)

[28] Courant, R., Friedrichs, K., Lewy, H.: Über die partiellen Differenzengleichungen der mathematischen Physik. Mathematische Annalen **100**, 32–74 (1928)

[29] Cullen, M.J.P.: A test of a semi-implicit integration technique for a fully compressible non-hydrostatic model. Quarterly Journal of the Royal Meteorological Society **116**, 1253–1258 (1990)

[30] Cullen, M.J.P.: Modelling atmospheric flows. Acta Numerica **16**, 67–154 (2007)

[31] Davies, T., Cullen, M.J.P., Malcolm, A.J., Mawson, M.H., Staniforth, A., White, A., Wood, N.: A new dynamical core for the Met Office's global and regional modelling of the atmosphere. Quarterly Journal of the Royal Meteorological Society **131**, 1759–1782 (2005)

[32] Davies, T., Staniforth, A., Wood, N., Thuburn, J.: Validity of anelastic and other equation sets as inferred from normal-mode analysis. Quarterly Journal of the Royal Meteorological Society **129**, 2761–2775 (2003)

[33] Dukowicz, J.K.: Evaluation of various approximations in ocean and atmospheric modeling based on an exact treatment of gravity wave dispersion. Monthly Weather Review **141**, 4487–4506 (2013)

[34] Durran, D.R.: Improving the anelastic approximation. Journal of the Atmospheric Sciences **46**, 1453–1461 (1989)

[35] Durran, D.R.: A physically motivated approach for filtering acoustic waves from the equations governing compressible stratified flow. Journal of Fluid Mechanics **601**, 365–379 (2008)

[36] Durran, D.R.: Numerical Methods for Fluid Dynamics: With Applications to Geophysics. Texts in Applied Mathematics. Springer (2010)

[37] Durran, D.R., Blossey, P.N.: Implicit-explicit multistep methods for fast-wave-slow-wave problems. Monthly Weather Review **140**, 1307–1325 (2012)

[38] Eckart, C.: Hydrodynamics of oceans and atmospheres. Pergamon Press (1960)

[39] Evans, L.C.: Partial differential equations. American Mathematical Society (2010)

[40] Falgout, R.D., Jones, J.E., Yang, U.M.: The design and implementation of *hypre*, a library of parallel high performance preconditioners. In: A. Bruaset, A. Tveito (eds.) Numerical Solution of Partial Differential Equations on Parallel Computers, vol. 51, pp. 267–294. Springer Berlin Heidelberg (2006)

[41] Gassmann, A.: A global hexagonal C-grid non-hydrostatic dynamical core (ICON-IAP) designed for energetic consistency. Quarterly Journal of the Royal Meteorological Society **139**, 152–175 (2013)

[42] Gatti-Bono, C., Colella, P.: An anelastic allspeed projection method for gravitationally stratified flows. Journal of Computational Physics **216**, 589–615 (2006)

[43] Geratz, K.J.: Erweiterung eines Godunov-Typ-Verfahrens für zwei-dimensionale kompressible Strömungen auf die Fälle kleiner und verschwindender Machzahl. Ph.D. thesis, Rheinisch-Westfälische Technische Hochschule Aachen (1997)

[44] Giraldo, F., Restelli, M.: A study of spectral element and discontinuous Galerkin methods for the Navier-Stokes equations in nonhydrostatic mesoscale atmospheric modeling: Equation sets and test cases. Journal of Computational Physics **227**, 3849–3877 (2008)

[45] Giraldo, F.X., Kelly, J.F., Costantinescu, E.M.: Implicit-explicit formulations of a three-dimensional nonhydrostatic unified model of the atmosphere (NUMA). SIAM Journal on Scientific Computing **35**, B1162–B1194 (2013)

[46] Gottlieb, S., Shu, C.W., Tadmor, E.: Strong stability-preserving high-order time discretization methods. SIAM review **43**, 89–112 (2001)

[47] Greenberg, J.M., Leroux, A.Y.: A well-balanced scheme for the numerical processing of source terms in hyperbolic equations. SIAM Journal on Numerical Analysis **33**, 1–16 (1996)

[48] Haack, J., Jin, S., Liu, J.G.: An all-speed asymptotic-preserving method for the isentropic Euler and Navier-Stokes equations. Commun. Comp. Phys. **12**, 955–980 (2012)

[49] Harlow, F., Welch, J.E.: Numerical calculation of time-dependent viscous incompressible flow of fluid with a free surface. Physics of Fluids **8**, 2182–2189 (1965)

[50] Holton, J.R.: An introduction to dynamic meteorology. Academic Press (2004)

[51] Hornung, R.D., Wissink, A.M., Kohn, S.R.: Managing complex data and geometry in parallel structured AMR applications. Engineering with Computers **22**, 181–195 (2006)

[52] Hortal, M.: The development and testing of a new two-time-level semi-Lagrangian scheme (SETTLS) in the ECMWF forecast model. Quarterly Journal of the Royal Meteorological Society **128**, 1671–1687 (2002)

[53] Janjic, Z., Gerrity Jr, J., Nickovic, S.: An alternative approach to nonhydrostatic modeling. Monthly Weather Review **129**, 1164–1178 (2001)

[54] Jebens, S., Knoth, O., Weiner, R.: Explicit two-step peer methods for the compressible Euler equations. Monthly Weather Review **137**, 2380–2392 (2009)

[55] Jin, S.: Efficient asymptotic-preserving (AP) schemes for some multiscale kinetic equations. SIAM Journal on Scientific Computing **21**, 441–454 (1999)

[56] Kadioglu, S.Y., Klein, R., Minion, M.L.: A fourth-order auxiliary variable projection method for zero-Mach number gas dynamics. Journal of Computational Physics **227**, 2012–2043 (2008)

[57] Käppeli, R., Mishra, S.: Well-balanced schemes for the Euler equations with gravitation. Journal of Computational Physics **259**, 199–219 (2014)

[58] Kelly, J.F., Giraldo, F.X.: Continuous and discontinuous Galerkin methods for a scalable three-dimensional nonhydrostatic atmospheric model: limited-area mode. Journal of Computational Physics **231**, 7988–8008 (2012)

[59] Klein, R.: Semi-implicit extension of a Godunov-type scheme based on low Mach number asymptotics I: One-dimensional flow. Journal of Computational Physics **121**, 213–237 (1995)

[60] Klein, R.: Asymptotic analyses for atmospheric flows and the construction of asymptotically adaptive numerical methods. Zeitschrift für Angewandte Mathematik und Mechanik **80**, 765–777 (2000)

[61] Klein, R.: Asymptotics, structure, and integration of sound-proof atmospheric flow equations. Theoretical and Computational Fluid Dynamics **23**, 161–195 (2009)

[62] Klein, R.: Scale-dependent models for atmospheric flows. Annual Review of Fluid Mechanics **42**, 249–274 (2010)

[63] Klein, R., Achatz, U., Bresch, D., Knio, O.M., Smolarkiewicz, P.: Regime of validity of soundproof atmospheric flow models. Journal of the Atmospheric Sciences **67**, 3226–3237 (2010)

[64] Klein, R., Botta, N., Hofmann, L., Meister, A., Munz, C.D., Roller, S., Sonar, T.: Asymptotic adaptive methods for multiscale problems in fluid mechanics. Journal of Engineering Mathematics **39**, 261–343 (2001)

[65] Klein, R., O'Neill, W.P., Benacchio, T.: Towards scale-dependent time integration for weakly compressible atmospheric flows. In: Proceedings of the ECMWF Seminar on Numerical Methods, 2-5 September, 2013. Reading, UK (2013)

[66] Klein, R., Pauluis, O.: Thermodynamic consistency of a pseudoincompressible approximation for general equations of state. Journal of the Atmospheric Sciences **69**, 961–968 (2011)

[67] Klemp, J.B., Wilhelmson, R.B.: The simulation of three-dimensional convective storm dynamics. Journal of the Atmospheric Sciences **35**, 1070–1096 (1978)

[68] Knoth, O., Wensch, J.: Generalized split-explicit Runge-Kutta methods for the compressible Euler equations. Monthly Weather Review **142**, 2067–2081 (2014)

[69] Konor, C.: Design of a dynamical core based on the nonhydrostatic unified system of equations. Monthly Weather Review **142**, 364–385 (2014)

[70] Kwatra, N., Su, J., Grétarsson, J.T., Fedkiw, R.: A method for avoiding the acoustic time step restriction in compressible flow. Journal of Computational Physics **228**, 4146–4161 (2009)

[71] Lauritzen, P.H., Mirin, A.A., Truesdale, J., Raeder, K., Anderson, J.L., Bacmeister, J., Neale, R.B.: Implementation of new diffusion/filtering operators in the CAM-FV dynamical core. International Journal of High Performance Computing Applications **26**, 63–73 (2012)

[72] LeVeque, R.J.: Finite Volume Methods for Hyperbolic Problems. Cambridge University Press (2002)

[73] Li, X., Chen, C., Shen, X., Xiao, F.: A multimoment constrained finite-volume model for nonhydrostatic atmospheric dynamics. Monthly Weather Review **141**, 1216–1240 (2012)

[74] Li, X.S., Gu, C.W.: An all-speed Roe-type scheme and its asymptotic analysis of low Mach number behaviour. Journal of Computational Physics **227**, 5144–5159 (2008)

[75] Lipps, F.B., Hemler, R.S.: A scale analysis of deep moist convection and some related numerical calculations. Journal of the Atmospheric Sciences **39**, 2192–2210 (1982)

[76] Majda, A.: Introduction to PDEs and Waves for the Atmosphere and Ocean. American Mathematical Society (2003)

[77] Majda, A., Sethian, J.: The derivation and numerical solution of the equations for zero Mach number combustion. Combustion Science and Technology **42**, 185–205 (1985)

[78] Müller, A., Behrens, J., Giraldo, F., Wirth, V.: Comparison between adaptive and uniform discontinuous Galerkin simulations in dry 2D bubble experiments. Journal of Computational Physics **235**, 371–393 (2013)

[79] Munz, C.D., Dumbser, M., Zucchini, M.: The multiple pressure variables method for fluid dynamics and aeroacoustics at low Mach numbers. In: Numerical Methods for Hyperbolic and Kinetic Problems, vol. 7, pp. 335–359. European Mathematical Society (2003)

[80] Nance, L.B., Durran, D.R.: A comparison of the accuracy of three anelastic systems and the pseudo-incompressible system. Journal of the Atmospheric Sciences **51**, 3549–3565 (1994)

[81] Noelle, S., Bispen, G., Arun, K.R., Lukáčová-Medvid'ová, M., Munz, C.D.: An asymptotic preserving all Mach number scheme for the Euler equations of gas dynamics. SIAM Journal on Scientific Computing (2014). Submitted.

[82] Nonaka, A., Almgren, A.S., Bell, J.B., Lijewski, M.J., Malone, C.M., Zingale, M.: MAESTRO: An adaptive low Mach number hydrodynamics algorithm for stellar flows. The Astrophysical Journal Supplement Series **188**, 358 (2010)

[83] Norman, M.R., Nair, R.D., Semazzi, F.H.M.: A low communication and large time step explicit finite-volume solver for non-hydrostatic atmospheric dynamics. Journal of Computational Physics **230**, 1567–1584 (2011)

[84] Ogura, Y., Phillips, N.A.: Scale analysis of deep and shallow convection in the atmosphere. Journal of the Atmospheric Sciences **19**, 173–179 (1962)

[85] Ohfuchi, W., Nakamura, H., Yoshioka, M.K., Enomoto, T., Takaya, K., Peng, X., Yamane, S., Nishimura, T., Kurihara, Y., Ninomiya, K.: 10-km mesh meso-scale resolving simulations of the global atmosphere on the Earth Simulator: Preliminary outcomes of AFES (AGCM for the Earth Simulator). Journal of the Earth Simulator **1**, 8–34 (2004)

[86] O'Neill, W.P., Klein, R.: A moist pseudo-incompressible model. Atmospheric Research **142**, 133–141 (2014)

[87] Patnaik, G., Guirguis, R.H., Boris, J.P., Oran, E.S.: A barely implicit correction for flux-corrected transport. Journal of Computational Physics **71**, 1–20 (1987)

[88] Piotrowski, Z.P., Wyszogrodzki, A.A., Smolarkiewicz, P.K.: Towards petascale simulation of atmospheric circulations with soundproof equations. Acta Geophysica **59**, 1294–1311 (2011)

[89] Prusa, J.M., Gutowski, W.J.: Multi-scale waves in sound-proof global simulations with EULAG. Acta Geophysica **59**, 1135–1157 (2011)

[90] Quarteroni, A., Sacco, R., Saleri, F.: Numerical mathematics. Springer (2007)

[91] Rabier, F.: Overview of global data assimilation developments in numerical weather-prediction centres. Quarterly Journal of the Royal Meteorological Society **131**, 3215–3233 (2005)

[92] Reisner, J.M., Mousseau, A., Wyszogrodzki, A.A., Knoll, D.A.: An implicitly balanced hurricane model with physics-based preconditioning. Monthly Weather Review **133**, 1003–1022 (2005)

[93] Restelli, M., Giraldo, F.X.: A conservative discontinuous Galerkin semi-implicit formulation for the Navier-Stokes equations in nonhydrostatic mesoscale modeling. SIAM Journal on Scientific Computing **31**, 2231–2257 (2009)

[94] Rider, W.J.: Filtering non-solenoidal modes in numerical solutions of incompressible flows. International Journal for Numerical Methods in Fluids **28**, 789–814 (1998)

[95] Rieper, F.: A low-Mach number fix for Roe's approximate Riemann solver. Journal of Computational Physics **230**, 5263–5287 (2011)

[96] Robert, A.: Bubble convection experiments with a semi-implicit formulation of the Euler equations. Journal of the Atmospheric Sciences **50**, 1865–1873 (1993)

[97] Rosa, B., Kurowski, M.J., Ziemiański, M.Z.: Testing the anelastic nonhydrostatic model EULAG as a prospective dynamical core of a numerical weather prediction model. Part I: dry benchmarks. Acta Geophysica **59**, 1236–1266 (2011)

[98] Saad, Y., Schultz, M.: GMRES: A generalized minimal residual algorithm for solving nonsymmetric linear systems. SIAM Journal on Scientific and Statistical Computing **7**, 856–869 (1986)

[99] Satoh, M., Matsuno, T., Tomita, H., Miura, H., Nasuno, T., Iga, S.: Nonhydrostatic icosahedral atmospheric model (NICAM) for global cloud resolving simulations. Journal of Computational Physics **227**, 3486–3514 (2008)

[100] Schneider, T., Botta, N., Geratz, K.J., Klein, R.: Extension of finite volume compressible flow solvers to multi-dimensional, variable density zero Mach number flows. Journal of Computational Physics **155**, 248–286 (1999)

[101] Seny, B., Lambrechts, J., Comblen, R., Legat, V., Remacle, J.F.: Multirate time stepping for accelerating explicit discontinuous Galerkin computations with application to geophysical flows. International Journal for Numerical Methods in Fluids **71**, 41–64 (2012)

[102] Skamarock, W.C., Klemp, J.B.: The stability of time-split numerical methods for the hydrostatic and the nonhydrostatic elastic equations. Monthly Weather Review **120**, 2109–2127 (1992)

[103] Skamarock, W.C., Klemp, J.B.: Efficiency and accuracy of the Klemp-Wilhelmson time-splitting technique. Monthly Weather Review **122**, 2623–2630 (1994)

[104] Skamarock, W.C., Klemp, J.B.: A time-split nonhydrostatic atmospheric model for weather research and forecasting applications. Journal of Computational Physics **227**, 3465–3485 (2008)

[105] Skamarock, W.C., Klemp, J.B., Duda, M.G., Fowler, L.D., Park, S.H., Ringler, T.D.: A multi-scale nonhydrostatic atmospheric model using centroidal Voronoi tesselations and C-grid staggering. Monthly Weather Review **140**, 3090–3105 (2012)

[106] Smolarkiewicz, P., Szmelter, J., Wyszogrodzki, A.: An unstructured-mesh atmospheric model for nonhydrostatic dynamics. Journal of Computational Physics **254**, 184–199 (2013)

[107] Smolarkiewicz, P.K., Charbonneau, P.: EULAG, a computational model for multiscale flows: An MHD extension. Journal of Computational Physics **236**, 608–623 (2013)

[108] Smolarkiewicz, P.K., Dörnbrack, A.: Conservative integrals of adiabatic Durran's equations. International Journal for Numerical Methods in Fluids **56**, 1513–1519 (2008)

[109] Smolarkiewicz, P.K., Kühnlein, C., Wedi, N.P.: A consistent framework for discrete integrations of soundproof and compressible PDEs of atmospheric dynamics. Journal of Computational Physics **263**, 185–205 (2014)

[110] Smolarkiewicz, P.K., Margolin, L.G., Wyszogrodzki, A.A.: A class of nonhydrostatic global models. Journal of the Atmospheric Sciences **58**, 349–364 (2001)

[111] Staniforth, A., Wood, N.: Aspects of the dynamical core of a nonhydrostatic, deep-atmosphere, unified weather and climate-prediction model. Journal of Computational Physics **227**, 3445–3464 (2008)

[112] Steppeler, J., Hess, R., Schättler, U., Bonaventura, L.: Review of numerical methods for nonhydrostatic weather prediction models. Meteorology and Atmospheric Physics **82**, 287–301 (2003)

[113] Straka, J.M., Wilhelmson, R.B., Wicker, L.J., Anderson, J.R., Droegemeier, K.K.: Numerical solutions of a nonlinear density current: A benchmark solution and comparisons. International Journal for Numerical Methods in Fluids **17**, 1–22 (1993)

[114] Szmelter, J., Smolarkiewicz, P.K.: An edge-based unstructured mesh framework for atmospheric flows. Computers & Fluids **46**, 455–460 (2011)

[115] Tanguay, M., Robert, A., Laprise, R.: A semi-implicit send-lagrangian fully compressible regional forecast model. Monthly Weather Review **118**, 1970–1980 (1990)

[116] Tapp, M.C., White, P.W.: A non-hydrostatic mesoscale model. Quarterly Journal of the Royal Meteorological Society **102**, 277–296 (1976)

[117] Thuburn, J.: Some conservation issues for the dynamical cores of NWP and climate models. Journal of Computational Physics **227**, 3715–3730 (2008)

[118] Tumolo, G., Bonaventura, L., Restelli, M.: A semi-implicit, semi-Lagrangian, p-adaptive discontinuous Galerkin method for the shallow water equations. Journal of Computational Physics **232**, 46–67 (2013)

[119] Ullrich, P., Jablonowski, C.: Operator-split Runge-Kutta-Rosenbrock methods for nonhydrostatic atmospheric models. Monthly Weather Review **140**, 1257–1284 (2011)

[120] Vasil, G.M., Lecoanet, D., Brown, B.P., Wood, T.S., Zweibel, E.G.: Energy conservation and gravity waves in sound-proof treatments of stellar interiors. II. Lagrangian constrained analysis. The Astrophysical Journal **773**, 169 (2013)

[121] Vater, S.: A multigrid-based multiscale numerical scheme for shallow water flows at low Froude number. Ph.D. thesis, Freie Universität Berlin (2013). URL http://edocs.fu-berlin.de/diss/receive/FUDISS_thesis_000000093897. Last accessed: April 3, 2014

[122] Vater, S., Klein, R.: Stability of a cartesian grid projection method for zero Froude number shallow water flows. Numerische Mathematik **113**, 123–161 (2009)

[123] Vater, S., Klein, R., Knio, O.: A scale-selective multilevel method for long-wave linear acoustics. Acta Geophysica **59**, 1076–1108 (2011)

[124] Van der Vorst, H.: Bi-CGSTAB: A fast and smoothly converging variant of Bi-CG for the solution of nonsymmetric linear systems. SIAM Journal on Scientific and Statistical Computing **13**, 631–644 (1992)

[125] Wan, H., Giorgetta, M.A., Zängl, G., Restelli, M., Majewski, D., Bonaventura, L., Fröhlich, K., Reinert, D., Rípodas, P., Kornblueh, L., Förstner, J.: The ICON-1.2 hydrostatic atmospheric dynamical core on triangular grids – Part 1: Formulation and performance of the baseline version. Geoscientific Model Development **6**, 735–763 (2013)

[126] Wedi, N.P., Hamrud, M., Mozdzynski, G.: A fast spherical harmonics transform for global NWP and climate models. Monthly Weather Review **141**, 3450–3461 (2013)

[127] Wedi, N.P., Hamrud, M., Mozdzynski, G., Austad, G., Curic, S., Bidlot, J.: Global, non-hydrostatic, convection-permitting, medium-range forecasts: progress and challenges. ECMWF Newsletter No. 133 (2012). URL http://www.ecmwf.int/publications/newsletters/pdf/133.pdf. Last accessed: April 3, 2014

[128] Weller, H., Shahrokhi, A.: Curl-free pressure gradients over orography in a solution of the fully compressible Euler equations with long time-steps. Monthly Weather Review (2014). Submitted.

[129] Wensch, J., Knoth, O., Galant, A.: Multirate infinitesimal step methods for atmospheric flow simulation. BIT Numerical Mathematics **49**, 449–473 (2009)

[130] White, A.A.: A view of the equations of meteorological dynamics and various approximations. In: J. Norbury, I. Roulstone (eds.) Large-scale Atmosphere-Ocean Dynamics I, pp. 1–100. Cambridge University Press (2002)

[131] Wicker, L.J., Skamarock, W.C.: Time-splitting methods for elastic models using forward time schemes. Monthly Weather Review **130**, 2088–2097 (2002)

[132] Wong, M., Skamarock, W.C., Lauritzen, P.H., Klemp, J.B., Stull, R.B.: A compressible nonhydrostatic cell-integrated semi-Lagrangian semi-implicit solver (CSLAM-NH) with consistent and conservative transport. Monthly Weather Review **142**, 1669–1687 (2013)

[133] Wood, N., Staniforth, A., White, A., Allen, T., Diamantakis, M., Gross, M., Melvin, T., Smith, C., Vosper, S., Zerroukat, M., Thuburn, J.: An inherently mass-conserving semi-implicit semi-lagrangian discretization of the deep-atmosphere global non-hydrostatic equations. Quarterly Journal of the Royal Meteorological Society (2013). DOI 10.1002/qj.2235

[134] Yang, D.: C++ and Object-oriented Numeric Computing for Scientists and Engineers. Springer (2001)

[135] Zingale, M., Dursi, L.J., ZuHone, J., Calder, A.C., Fryxell, B., Plewa, T., Truran, J.W., Caceres, A., Olson, K., Ricker, P.M., Riley, K., Rosner, R., Siegel, A., Timmes, F.X., Vladimirova, N.: Mapping initial hydrostatic models in Godunov codes. The Astrophysical Journal Supplement Series **143**, 539–565 (2002)